

https://dspace.org/

Investigation of the Isoscalar Giant Monopole Resonance as a function of neutron excess in the 40,42,44,48Ca isotope chain

Olorunfunmi, Sunday Daniel

2020

https://hdl.handle.net/10539/31604

Downloaded from a DSpace repository. https://dspace.org/

Investigation of the Isoscalar Giant Monopole Resonance as a function of neutron excess in the ^{40,42,44,48}Ca isotope chain

Sunday Daniel Olorunfunmi

A thesis submitted to the Faculty of Science,
University of the Witwatersrand, in fulfilment of
the requirements for the degree of
Doctor of Philosophy.

Johannesburg, May 2020

Supervisor:
Prof. I.T. Usman
School of Physics, University of the Witwatersrand

Co-supervisor(s):
Prof. J. Carter
School of Physics, University of the Witwatersrand

Dr. R. Neveling
iThemba LABS, Cape Town

Declaration

I declare that this thesis is my own unaided work. It is being submitted for the Degree of Doctor of Philosophy to the University of the Witwatersrand, Johannesburg. It has not been submitted previously for any degree or examination to any other university.



Sunday Daniel Olorunfunmi
May 20, 2020

Abstract

Experiments investigating the fine structure of the IsoScalar Giant Monopole Resonance (ISGMR) of ^{40}Ca, ^{42}Ca, ^{44}Ca and ^{48}Ca were carried out with 200 MeV alpha inelastic scattering at $\theta_{\mathrm{Lab}} = 0^{\circ}\pm2^{\circ}$ and $\theta_{\mathrm{Lab}} = 4^{\circ}\pm2^{\circ}$, using the high energy-resolution K600 magnetic spectrometer Zero-degree Facility and small angle mode of iThemba LABS, Cape Town, South Africa. Good energy-resolution of 85 keV (FWHM) was attained which allowed for a clear observation of fine structure in the excitation energy region of the ISGMR which lies between 10 and 22 MeV.

Alpha-particle inelastic scattering at intermediate energies has been used in numerous investigations across the periodic table to extract $E0$ strength and determine the properties of the ISGMR. This is made possible since the $L = 0$ multipole has a maximum at zero degrees while all other low-order multipoles have much lower yields. In the present experiment on calcium isotopes, the $L = 0$ multipole exhibits strong oscillating structure at small scattering angles, with a deep minimum at $\theta_{\mathrm{Lab}} \approx 3.5^{\circ}$, which allows the Difference of Spectra (DoS) technique to be used. Here, the background from all other low-order multipoles excited is removed by taking an angle-cut from the measured 4° spectrum and subtracting from the measured 0° spectrum. This is more reliable than the alternate Multipole Decomposition Analysis (MDA) technique which requires an arbitrary background to be first defined.

In the present project, the Fraction $E0$ EWSR and corresponding $E0$ strength distributions were extracted and compared to other measurements. In addition and for the first time, characteristic energy scales were extracted from the measured high energy-resolution $E0$ strength distributions. These were compared to those from state-of-the-art theoretical calculations in order to gain insight into the ISGMR damping mechanisms.

The theoretical calculations considered are within the framework of the Phonon Phonon Coupling (PPC), the Quasiparticle Time Blocking Approximation (QTBA) and the Quasi-particle Random Phase Approximation (QRPA). Of all these models, the PPC best described the experimental data for all the four calcium isotopes in terms of reproducibility of the energy scales present in them as well as in terms of the amount of fine structure exhibited and the prediction of the centroid energies, compared to the other models.

Level densities of the $J^{\pi} = 0^{+}$ states were extracted from experimental data for the doubly magic ^{48}Ca and ^{40}Ca isotopes and compared with those of phenomenological Back Shifted Fermi Gas (BSFG) model predictions and calculations of the Hartree-Fock Bogoluibov (HFB) microscopic model.

Dedication

This work is dedicated to my wife Faith Olorunfunmi
and
my children Bukunmi and Iretomiwa Olorunfunmi

Acknowledgements

First, my sincere appreciation goes to my two university supervisors, namely Professor Iyabo Usman and Professor John Carter, who have guided me through the PhD program. I appreciate their excellent supervision of this work as well as their continuous advice, encouragement and support all through my time of working with them. I am grateful to them for their continuous push toward perfection, especially during the preparation of this thesis. I would like to specially thank them for the care and concern they have shown, always asking after my physical well-being and that of my family.

Special thanks to my supervisor at iThemba LABS, Dr. Retief Neveling for his excellent supervision and immense contributions to this work. He patiently walked me through the data extraction and analysis procedures. I have lost count of all the emails we exchanged, in addition to the many one-on-one meeting, to fine-tune the data analysis. I appreciate you for your encouragement both in cash and kind. You carefully went through all the many versions of my thesis, thank you. I am grateful for introducing me to programming in C++ and ROOT software package. "*Dankie*".

I would like to express my special thanks to Professor Dr Peter von Neumann-Cosel for his insightful comments and contributions to this work. Thank you for creating time out of your busy schedule for the one-on-one discussions and Skype meetings with me and my supervisors.

I am indebted to Dr Panagiota Papakonstantinou of the Institute for Basic Science, Daejeon, South Korea, Dr. Elena Litvinova of the Western Michigan University and Dr. Nikolay Arsenyev of Bogoliubov Laboratory of Theoretical Physics, Dubna, for providing the theoretical calculations used in this project.

Thank you for the contributions you made to this thesis and for your readiness to read the relevant sections and provide insightful comments. I am grateful.

Special thanks to Kelvin Howard of University of Notre Dame,USA, for providing the python code for calculating the transition potentials as well as the link to PTOLEMY code. Despite your busy schedule you always make out time to answer all my questions on the code in a manner that educate me instead of just informing me. Thanks.

I would like appreciate all the members fo the Wits Nuclear Structure Research Group and the researchers at iThemba LABS. Particularly to Armand Bahini, Abraham Avaa, Mistura Ajani, Harshna Jivan, Dr. Philip Adsley, Dr. Lindsay Donaldson, Dr.Luna Pellegri and Professor Elias Sideras-Haddad. Thank you for the various forms of assistant you offered me in the course of this program.

I acknowledge and appreciate contributions of the various research groups at iThemba LABS, namely, the SSC accelerator team, the K600 group, the target-making team and the post-graduate students. Thank you all for your contributions to this work especially, in the experimental setup and the data collections.

My sincere appreciation goes to my parents Mr. and Mrs. J.O. Olorunfunmi and all siblings (Sister Muyiwa, Brother Titus, Seye, Seyi, Soga, Opeyemi and Joke) for their prayers and moral supports all through the period of the PhD program. I want to specially thank my father who planted the desire for a PhD degree in me at a tender age. I remember some years ago during one of our family morning devotions, my father said, "I am ready and willing to sponsor your education even up to PhD level if you so desire". Even though I was in high school then, and I knew next to nothing about a PhD degree, that statement birth in me the desire to study up to a PhD level. *"E se baba mi!"*

A big thank you to my father and mother in-law Alh. (Mr.) and Mrs. Awotedu for all their supports to me and my family. I appreciate those words of encouragement and prayers for me whenever we speak over the pone or I come visiting. To my brother and sisters inlaw: Opeyemi, Aisha and Latifat, I acknowledge your benevolence towards me, my wife and our children.

Special thanks to Aisha and Opeyemi for always coming to pick me from and to the airport each time I visit Nigeria. To you Latifat, thank you for taking time despite your busy schedule to travel from London to Scotland to visit me when I was in the UK for a conference. You even did the video recording of my presentation and sent to my wife. Thank you and God bless you.

I want to specially to my darling, Faith Olorunfunmi, for her encouragement, love, and support and for patiently enduring my absence from home and being alone with our children: Oluwabukunmi and Ireoluwatomiwa, during the years of this program. I love you and may God help me to love you more, even as Christ love the Church. To Oluwabukunmi and Ireoluwatomiwa, thanks for enduring the many nights "papa" was not available to read bedtime story book for you. I will make it up for you all. I love you.

I acknowledge the prayers and support of all my brothers and sisters in Christ at the Deeper Life Campus Fellowship (DLCF) at WITS and UJ. I will forever remember the atmosphere of love and warm fellowship I enjoyed all through the period being in your midst. Notably, I want to thank Professor Oyerinde and his entire family for all financial, moral and spiritual support you shower me with since the day I got to South Africa. I appreciate Mummy Oyerinde for those timely calls to pick up something for lunch in her office. Thank you. My appreciation also goes to the National Overseer of the Deeper Christian Life Ministry in SA, in person of Pastor John Amoni and the entire leadership of the Deeper Life Bible Church in South Africa. Thank you all for your prayers and support.

Special thanks to all my friends who have encouraged and supported me all through the period of this program. In particular, Mr. and Mrs. Adedayo Adefelu, thank you for the moral and spiritual support given to me and my family. Of a truth God answered all your prayers for me. I am grateful.

I would like to acknowledge the financial support that I received throughout the duration of the study, namely the iThemba LABS Top-Up Bursary and Bursary supplementation from Research funds of Professor Iyabo Usman to pay my tuition fees during three years (2017-2019) and to attend conferences.

I also wish to acknowledge the support of the management of the Obafemi

Awolowo University (OAU) for giving me the opportunity to go out and undertake this PhD program at WITS, South Africa. I wanted to specially thank all members of staff in the Department of Physics and Engineering Physics, OAU, for their encouragement and support all through the period of the PhD program.

Above all, I give all the glory to God Almighty, the fountain of all knowledge for providing me with the needed brains and brawn to complete this research.

Contents

Declaration ii

Abstract iii

Dedication v

Acknowledgements vi

List of Figures xiii

List of Tables xxii

1 Introduction 1

1.1 ISGMR in medium to low-mass range 4

1.2 ISGMR in calcium isotopes 6

1.3 Present work 12

2 Theoretical considerations 14

2.1 Giant resonances 14

2.1.1 Macroscopic description of giant resonances 15

2.1.2 Microscopic description of giant resonances 16

2.1.3 Isoscalar giant monopole resonance 18

2.2 Damping width and decay of giant resonances 19

2.2.1 Microscopic models for the damping of the ISGMR . . . 20

2.2.1.1 Random Phase Approximation (RPA) 20

2.2.1.2 Second RPA (SRPA) 21

2.2.1.3 Quasi-particle RPA (QRPA) 22

2.2.1.4 Quasiparticle Time Blocking Approximation (QTBA) 23

2.2.1.5 Phonon-Phonon Coupling (PPC) 23

2.2.2 Distorted-wave Born Approximation (DWBA) 25
2.2.2.1 Energy weighted sum rule (EWSR) 27
2.3 Extraction of characteristics energy scales 29
2.3.1 Wavelet analysis 29
2.4 Extraction of level densities 32
2.4.1 Theoretical models for level density extraction 33
2.4.1.1 Phenomenological models 33
2.4.1.2 Microscopic statistical models 34
2.4.2 Fluctuation analysis 34
2.4.2.1 Procedure of fluctuation analysis for (α, α') spectrum 36

3 Experimental procedure and data extraction 38
3.1 iThemba LABS Separated Sector Cyclotron 39
3.2 iThemba LABS K600 magnetic spectrometer 41
3.2.1 Focal plane detector suite 43
3.2.1.1 Vertical drift chambers 43
3.2.1.2 Plastic scintillators 45
3.2.2 Dispersion matching techniques 47
3.2.2.1 Faint beam method 48
3.3 Target preparation and handling 48
3.4 Experimental procedure 50
3.5 Data extraction and offline analysis: zero degrees measurements 51
3.5.1 Particle identification 52
3.5.2 Data alignment and chained data 57
3.5.3 Lineshape correction 57
3.5.4 Background subtraction 59
3.5.5 Energy calibration 60
3.5.5.1 Target thickness effects 63
3.5.6 Experimental double differential cross-sections 65
3.6 Data extraction and offline analysis: 4° measurements 70
3.6.1 Angle calibration 71
3.6.2 Energy calibration 76

4 Results, analysis and discussion 79
4.1 Overview of the measured experimental (α, α') data 80
4.1.1 Experimental ^{40,42,44,48}Ca cross-sections after removal of ^{16}O contamination 83

4.2 Extraction of $E0$ strength for ^{40,42,44,48}Ca 90
4.2.1 DWBA multipole calculations 90
4.2.2 Difference-of-Spectra (DoS) technique 94
4.2.3 Determination of the Fraction $E0$ EWSR and the $E0$ strength distributions 100
4.2.4 Discussion 106
4.3 Discussion of ISGMR strength distributions in ^{40,42,44,48}Ca . . . 107
4.3.1 Overview of ISGMR in ^{40,42,44,48}Ca 107
4.3.2 Comparison of experimental ISGMR and theoretical predictions for ^{48,44,42,40}Ca 115
4.4 Fine structure analysis of ^{40,42,44,48}Ca $E0$ strength 121
4.4.1 Effect of the DoS technique on the extraction of energy scales 121
4.4.2 Experimental and theoretical wavelet energy scales . . . 127
4.4.2.1 Discussion 135
4.5 Level density of 0^+ states in the ISGMR region for ^{40,42,44,48}Ca . 137
4.5.1 Fluctuation analysis 137
4.5.2 Extraction of level densities of 0^+ states in ^{40,42,44,48}Ca . 137

5 Conclusions **143**

References **145**

List of Figures

1.1 Notional strength distributions for various giant resonances overlapping in excitation energy. Taken from [Pat15]. 2

1.2 *Upper*: Double-differential cross sections measured at an averaged angle 0.7° for ^{90}Zr, ^{92}Zr and ^{92}Mo. *Lower*: Difference spectra of average angles 0.7° & 2.0° for the same nuclei. Taken from [Gup16] 5

1.3 ISGMR response for ^{24}Mg, ^{58}Ni and ^{90}Zr at $E_\alpha = 200$ MeV and $\theta_{\text{Lab}} = 0°$. Taken from [Moo19]. 6

1.4 Experimental results for the ISGMR energies in ^{40}Ca [You97], ^{44}Ca [But17], and ^{48}Ca [Lui11] (blue diamonds) are compared with theoretical predictions (red squares). Here, $\sqrt{m_1/m_{-1}}$ (left panel down), m_1/m_0 (top left panel) and $\sqrt{m_3/m_1}$ (top right panel) are the constrained energy, centroid energy and scaling energy, respectively. Taken from [But17]. 9

1.5 Inelastic alpha scattering spectra at $E_\alpha = 240$ MeV and $\theta_{\text{c.m.}} = 1.1°$ and 4.3° for ^{48}Ca. Taken from [Lui11]. 10

1.6 The angular distributions of the ^{48}Ca cross section at $E_{\text{x}} = 16.23$ MeV from the TAMU work. Taken from [Lui11]. 11

2.1 Schematic picture of various collective modes, taken from [Don16] 15

2.2 Schematic representation of $E0$, $E1$ and $E2$ single-partice transitions between shell-model states, taken from [She04]. . . . 17

2.3 Schematic representation of some widely used wavelet functions, taken from [Lat17] 30

2.4 Schematic illustration of how the original spectrum is decomposed into approximation and details components using the DWT, taken from [Lat17] 32

3.1 The layout of the cyclotron facility at iThemba LABS [Nev11]. . 40

3.2 The layout of the K600 facility in the zero degree mode with the focal plane detectors positioned in the high-dispersion focal plane. 42

3.3 A schematic view of the focal plane detectors. 43

3.4 A layout of the K600 trigger electronics. Note that only signals from paddle 1 are used to create the QDC gate or trigger signal. 46

3.5 (a) Target-ladder-transfer chamber. (b) Ca targets mounted on the target-ladder inside the transfer chamber. (c) The transfer chamber mounted on the spectrometer scattering chamber. . . . 50

3.6 Top: A plot of energy deposited in paddle 1 versus TOF for α particles incident on ^{48}Ca target showing various PID loci. Bottom: Position spectrum obtained from the α PID gate. . . . 54

3.7 Top: Paddle1-versus-TOF PID plot for α particles incident on ^{48}Ca target showing the proton PID gate. Bottom: Position spectrum obtained from the proton PID gate. 54

3.8 Top: Paddle1-versus-TOF PID plot for α particles incident on ^{48}Ca target showing the beam halo PID gate. Bottom: Position spectrum obtained from the beam halo PID gate. 55

3.9 Top: Paddle1-versus-TOF PID plot for α particles incident on a ^{48}Ca target showing the background below the alpha PID gate. Bottom: Position spectrum obtained from the background below the alpha PID gate. 55

3.10 Top: Paddle1-versus-TOF PID plot for α particles incident on an empty target showing the alpha PID gate. Bottom: Position spectrum for the empty obtained from the alpha PID software gate (marked in red). 56

3.11 A plot of scattering angle versus the focal plane position (top) before and after (bottom) lineshape correction for ^{24}Mg. 59

3.12 A scatter plot of Y_{fp} versus X_{fp} showing the background regions B1 and B2, and the central region ΔY containing events of interest on top of the backgrounds. 60

3.13 The focal plane position spectrum for inelastic α scattering from ^{24}Mg target before the background subtraction. 61

3.14 The lineshape-corrected and background-subtracted focal plane position spectrum for inelastic α scattering from ^{24}Mg. The peak in red is the 9.305 MeV 0^+ state that was used to obtain the TOF and position offsets. 61

3.15 A second-order polynomial fit of the momentum of the scattered particle plotted against the corrected focal plane position. . . . 62

3.16 The ^{24}Mg excitation-energy spectrum accessible in the PR260 0° measurements. 68

3.17 A magnified ^{24}Mg excitation-energy spectrum showing identified states used for the calibration. The energy resolution is 85.7 keV full width at half maximum (FWHM), based on the 9.305 MeV 0^+ state. 68

3.18 A plot of the difference between the calibrated (this work) and the assigned excited states versus the focal plane position 69

3.19 A plot of energy deposited in paddle 1 versus TOF for α particles incident on a ^{24}Mg target showing various PID loci. 70

3.20 Drift length. 71

3.21 A focal plane angle $\theta_{\rm fp}$ plot for the pepperpot run showing the associated Gaussian fits to the observed peaks for $x_{\rm fp} = 613$ mm. 73

3.22 The resultant scattering angle $\theta_{\rm SCAT}$ plot for the pepperpot run 2022 at $x_{\rm fp} = 613$ mm which illustrates the reconstructed scattering angle relative to $\theta_{\rm K600}$. 73

3.23 Calibrated horizontal and vertical scattering angle for the pepperpot collimator relative to $\theta_{\rm K600} = 4°$. 74

3.24 The focal plane angle versus scattering angle plots from the normal collimator showing the 4° aperture of the K600 spectrometer represented by the red circle. 75

3.25 The focal plane angle versus scattering angle plots at various angle cut. 75

3.26 $x_{\rm fp}$ versus $\theta_{\rm SCAT}$ plot before the lineshape correction. 76

3.27 $x_{\rm fp}$ versus $\theta_{\rm SCAT}$ plot after the lineshape correction. 77

3.28 Measured excitation energy spectrum for the ^{24}Mg(α,α') reaction, used for energy calibration. 78

4.1 Measured excitation energy spectrum for the ^{40,42,44,48}Ca(α,α') at $E_\alpha = 200$ MeV and $\theta_{\rm Lab} = 0°$ showing the ^{16}O contaminant peaks. 81

4.2 Measured excitation energy spectrum for the ^{40,42,44,48}Ca(α,α') at E_α = 200 MeV and $\theta_{\rm Lab} = 4^\circ$ showing the ^{16}O contaminant peaks. 82

4.3 Panel (a): Mylar spectrum (black) with superimposed ^{12}C spectrum (magenta). Panel (b): Extracted ^{16}O spectrum. Panel (b): Spectra of oxygen-contaminated ^{48}Ca (black), extracted ^{16}O (green) and oxygen-free ^{48}Ca (blue). 84

4.4 Superposition of experimental oxygen-contaminated and oxygen-subtracted excitation energy spectra for ^{48,44,42,40}Ca(α,α') at E_α = 200 MeV and $\theta_{\rm Lab} = 0^\circ$ - 2°. 85

4.5 Double-differential cross sections obtained from oxygen-free spectra of ^{48,44,42,40}Ca. 86

4.6 Panel (a): Mylar spectrum (black) with superimposed ^{12}C spectrum (magenta). Panel (b): Extracted ^{16}O spectrum. Panel (b): Spectra of oxygen-contaminated ^{48}Ca (black), extracted ^{16}O (green) and oxygen-free ^{48}Ca (red) 87

4.7 Superposition of experimental oxygen-contaminated and oxygen-subtracted excitation energy spectra for ^{48,44,42,40}Ca(α,α') at E_α = 200 MeV and $\theta_{\rm Lab} = 4^\circ$. 88

4.8 Double-differential cross sections obtained from oxygen-free spectra of ^{48,44,42,40}Ca at $\theta_{\rm Lab} = 4^\circ$. 89

4.9 Angular distributions of the differential cross-sections for inelastic alpha particle scattering on ^{48}Ca at $E_{\rm x}$ = 16.23 MeV and at E_α = 240 MeV (upper panel) and E_α = 200 MeV (lower panel) for L = 0, 1, 2, 4 and L = 1, T = 1. The black dashed line represent the sum of L = 1, 2, 4 and L = 1, T = 1, while the solid black line represents the sum of all the multipoles shown. Note that the data shown in the upper panel are from Lui *et al.* [Lui11]. 93

4.10 Double-differential cross section for ^{48}Ca(α, α') at $E_\alpha = 200$ MeV. The blue spectrum is for $0^\circ \leq \theta_{\rm Lab} \leq 2^\circ$ (see Fig. 4.5), the red is for $2.76^\circ \leq \theta_{\rm Lab} \leq 4.31^\circ$ (which correspond to $3^\circ \leq \theta_{\rm c.m.} \leq 4.5^\circ$, see angle region shown in Fig. 4.9 and is cut from the ^{48}Ca spectrum shown in Fig. 4.8) and the black is the difference spectrum obtained by subtracting the $2.76^\circ - 4.31^\circ$ spectrum (red) from the 0° spectrum (blue). Note that the $0^\circ - 2^\circ$ spectrum was scaled by a factor of 1.32 in order to make the cross-section equivalent to that which would be measured at $\theta_{\rm Lab} = 0^\circ$. 96

4.11 Same as Fig. 4.10 but for ^{44}Ca(α,α'). The $0^\circ - 2^\circ$ spectrum was scaled by a factor of 1.45. 97

4.12 Same as Fig. 4.10 but for ^{42}Ca(α,α'). The $0^\circ - 2^\circ$ spectrum was scaled by a factor of 1.33. 98

4.13 Same as Fig. 4.10 but for ^{40}Ca(α,α'). The $0^\circ - 2^\circ$ spectrum was scaled by a factor of 1.35. 99

4.14 An outline of the conversion process from the double-differential cross section of ^{48}Ca(α, α') to fraction $E0$ EWSR per MeV and then to $E0$ strength distribution. See text for detailed explanation. 102

4.15 Same as Fig. 4.14 but for ^{44}Ca(α,α'). 103

4.16 Same as Fig. 4.14 but for ^{42}Ca(α,α'). 104

4.17 Same as Fig. 4.14 but for ^{40}Ca(α,α'). 105

4.18 Double-differential cross section of the difference spectra for ^{40,42,44,48}Ca at $E_\alpha = 200$ MeV. 112

4.19 ISGMR strength distribution for ^{48}Ca (black circles), ^{44}Ca (blue circles), ^{42}Ca (green circles) and ^{40}Ca (red circles). The solid lines represent the Lorentzian fit. 113

4.20 Overview of the centroid values for the ISGMR across the periodic table (see Table 4.4). 114

4.21 From top to bottom: ISGMR strength distribution for ^{48}Ca(α, α') overlaid with PPC result (in red) folded with 2 MeV; strength functions within the framework of PPC, QTBA, QRPA, SRPA and RPA. 117

4.22 From top to bottom: ISGMR strength distribution for ^{44}Ca(α, α') overlaid with PPC result (in red) folded with 2 MeV; strength functions within the framework of PPC, QTBA and QRPA. 118

4.23 From top to bottom: ISGMR strength distribution for ^{42}Ca(α, α') overlaid with PPC result (in red) folded with 2 MeV; strength functions within the framework of PPC, QTBA, QRPA, SRPA and RPA. 119

4.24 From top to bottom: ISGMR strength distribution for ^{40}Ca(α, α') overlaid with PPC result (in red) folded with 2 MeV; strength functions within the framework of PPC, QTBA, QRPA, SRPA and RPA. 120

4.25 *Top Segment*: Experimental double-differential cross section for ^{48}Ca(α, α') at $\theta_{\text{Lab}} = 0°$-$2°$ (top right panel), wavelet coefficients from CWT (right panel on the second row down) and power spectrum (left panel on the second row down). *Bottom segment*: Difference spectrum for ^{48}Ca(α, α') (right panel on the third row down), wavelet coefficients from CWT (right panel on the lowest row) and corresponding power spectrum in black superimposed on power spectrum from $\theta_{\text{Lab}} = 0°$ data (left panel on the lowest row). 123

4.26 Same as Fig 4.25, but for ^{44}Ca. 124

4.27 Same as Fig 4.25, but for ^{42}Ca. 125

4.28 Same as Fig 4.25, but for ^{40}Ca. 126

4.29 *Top Segment*: ISGMR strength distribution for ^{48}Ca(α, α') (top right panel), wavelet coefficients from CWT (right panel on the second row) and power spectrum (left panel on the second row). *Bottom Segment*: ISGMR strength distribution for ^{40}Ca(α, α') (right panel on the third row), wavelet coefficients from CWT (right panel on the last row) and power spectrum (left panel on the last row) with characteristic energy scales indicated by the black arrows. Excitation-energy region of 12 - 24 MeV was considered as indicated between the dashed black lines. 129

4.30 Same as Fig 4.29, but for ^{44}Ca and ^{42}Ca. 130

4.31 *From top to bottom*: On the right hand side is the ^{48}Ca(α, α') spectrum, the ^{48}Ca - PPC spectrum, the ^{48}Ca - QTBA spectrum and the ^{48}Ca - QRPA spectrum. On the left hand side are the corresponding power spectra with the characteristic scales pointed out with black arrows. 131

4.32 Same as Fig. 4.31 but for ^{44}Ca 132

4.33 Same as Fig. 4.31 but for ^{42}Ca 133

4.34 Same as Fig. 4.31 but for ^{40}Ca 134

4.35 *Upper part top*: Spectrum of the ^{48}Ca(α, α') reaction at 0°. *Upper part middle*: Smoothed spectra $g(E\mathrm{x})$ and $g_{>}(E_{\mathrm{x}})$. *Upper part bottom*: Stationary spectrum $d(E_{\mathrm{x}})$. *Lower part*: Experimental (magenta line) and theoretical (dark yellow line) autocorrelation functions. 140

4.36 Level density of 0^{+} states extracted from ^{48}Ca(α, α') and the theoretical models: BSFG of Ref. [Egi05] (green line), BSFG of Ref. [Rau97] (red line), HFB of Ref. [Hil06] (dark yellow line) and HF-BCS of Ref. [Dem01] (blue line). 141

4.37 Level density of 0^+ states extracted from ^{40}Ca(α, α') and the theoretical models: BSFG of Ref. [Egi05] (green line), BSFG of Ref. [Rau97] (red line), HFB of Ref. [Hil06] (dark yellow line) and HF-BCS of Ref. [Dem01] (blue line). 142

List of Tables

2.1 Multipole excitations as p-h excitations across major shells [Har01]. 18

3.1 Technical specifications of the vertical drift chamber [Nev17]. . 44

3.2 Technical specifications of a plastic scintillator [Nev17]. 45

3.3 Areal thickness and corresponding isotopic enrichment of targets used [Lat17]. 49

3.4 TOF and position offsets with the corresponding position resolutions for different experimental runs. The position offsets and resolution were obtained for the 9.305 MeV 0^+ state in ^{24}Mg. 58

3.5 Focal-plane positions of well-known excited states in ^{24}Mg and the calculated average $QB\rho$ for a 200 MeV alpha beam on 2.1 mg/cm^2 thick target. See text for detail. 64

3.6 Comparison of ^{24}Mg excited states obtained in this work with values reported in NNDC [Fir07] and by Kawabata *et al.* [Kaw10]. The last column shows the difference between calibrated excited states and assigned excited states. 65

3.7 The horizontal and vertical focal plane position offsets, and the TOF offset per run for ^{48}Ca relative to run 3024. 72

3.8 Calculated solid angle $\Delta\Omega$ for various range of Θ. 76

4.1 Optical-model and Fermi distribution parameters [You97, Lui11] used in DWBA calculations. Note: a and c are from [Fri95]. 92

4.2 Moments of the ground state density for ^{40,42,44,48}Ca, taken from [Fri95]. 101

4.3 Extracted values of centroids and widths of the ISGMR using Lorentzian fits. 108

4.4 Values for centroid positions and widths for the ISGMR across the periodic table. 109

4.5 Centroid energies (in MeV) calculated from the moment ratio (m_1/m_0) over the energy range 10 to 25 MeV. For comparison purpose centroid energies were also calculated for TAMU and RCNP data set over the excitation energy range 10 MeV to 25 MeV. 110

4.6 Characteristic energy scale values extracted from the experimental spectrum and theoretical calculations of the PPC, QTBA and QRPA for doubly-magic ^{48,40}Ca. Equivalent characteristic energy scale values are shown in red. 128

4.7 Characteristic energy scale values extracted from the experimental spectrum and theoretical calculations of the PPC, QTBA and QRPA for ^{44,42}Ca. Equivalent characteristic energy scale values are shown in red. 128

Chapter 1

Introduction

The atomic nucleus is a many-body quantum system and in such a system collective oscillations are a common occurrence. Nuclear giant resonances, which are the subject of this study, can be defined as small-amplitude, high-frequency, simple collective modes of excitation, considered to be the fastest vibrations of any known many-body system. They are characterised by excitation energies above the particle emission threshold and broad widths greater than 2 MeV. In quantum-mechanical terms, the resonance corresponds to a transition between the ground state and a collective state and its strength is described by a transition amplitude. The strength of a giant resonance depends on the size of the system and the number of nucleons able to participate, and is limited by a sum rule. For a resonance to be considered giant, its observed strength should exhaust more than 60 % of the associated sum rule [Har01]. Giant resonances are classified by a change in three quantum numbers characterising the transition between the ground state and a collective state. The three quantum numbers are: the angular momentum transfer L, the spin S and the isospin T.

Microscopically, giant resonances can be described as a collective excitation of particle-hole (p-h) states. Such collective excitations occur due to the presence of a residual p-h interaction which, for a given multipolarity and parity, creates a coherent superposition of all possible p-h states. This residual interaction is attractive and repulsive for isoscalar and isovector excitations, respectively. As a result, various resonances overlap in excitation energy, where Fig. 1.1 depicts this situation. Furthermore, these resonances have large width, especially at higher energies, resulting from the coupling of the one-particle one-hole state

with more complex two-particle two-hole states of the same spin and parity [Har01]. Therefore, to investigate a particular mode of excitation, it is highly necessary to select a suitable probe so as to attain selectivity in exciting the desired mode

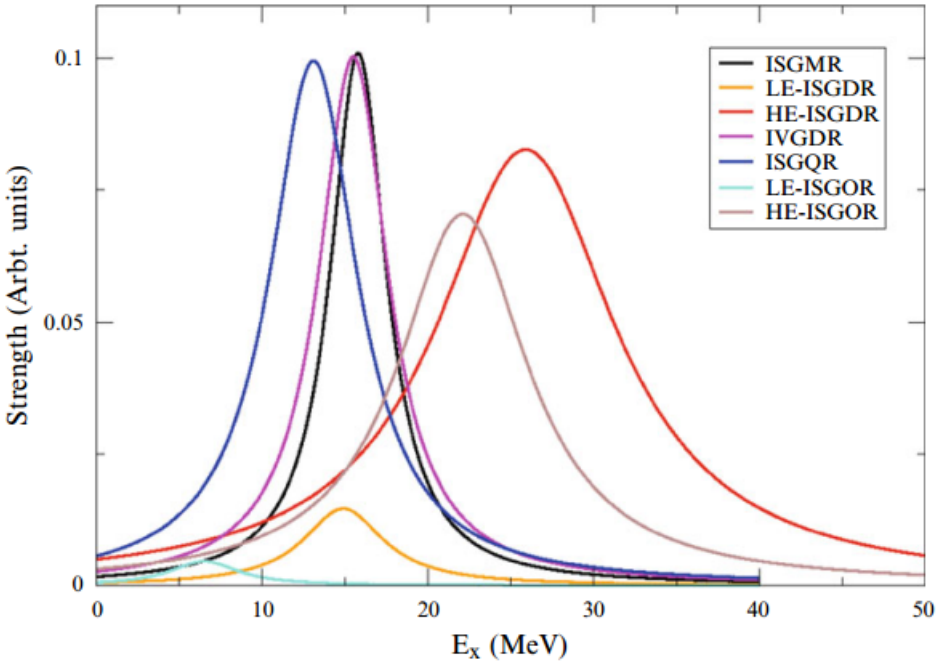


Figure 1.1: Notional strength distributions for various giant resonances overlapping in excitation energy. Taken from [Pat15].

The first evidence of giant resonances was discovered in 1937 by Bothe and Gentner [Bot37], who observed nuclear vibrations in the measurements of photon absorption from the bombardment of several nuclei with electromagnetic radiation produced in the Li(p,γ) reaction. In 1944, the first theoretical prediction of the electric dipole resonance was given by Migdal [Mig44]. In the subsequent years, theoretical descriptions of giant resonances progressed and systematic studies of the Isovector Giant Dipole Resonance (IVGDR) were under way.

About 30 years after the first observation of the IVGDR, the Isoscalar Giant Quadrupole Resonance (ISGQR) was discovered in inelastic electron scattering by Pitthan and Walcher [Pit71] and in inelastic proton scattering by Lewis and Bertrand [Lew72]. This showed that giant resonances were not solely isovector in nature. Since then, considerable effort has been put into identifying many other giant resonance modes. In 1977, the Isoscalar Giant

Monopole Resonance (ISGMR) was found by Harakeh *et al.* [Har77] by means of inelastic α-particle scattering at 120 MeV on ^{206,208}Pb. From its discovery in 1977 up until now, the ISGMR has been extensively studied both for stable and unstable nuclei not only by inelastic α-particle scattering but also by deuteron scattering [Pat14]. Studies in the past and recent times have established α-particle scattering as the best probe for studying the ISGMR because it has zero spin and isospin and, hence, the electric isoscalar resonances are predominantly excited. Isoscalar giant resonances in medium and heavy-mass nuclei are the pronounced manifestation of nuclear collective motion [Con09]. Hence, they carry important information regarding the dynamics of the nuclear excitation process and the properties of the nuclear Hamiltonian.

Furthermore, experimental study of the "monopole breathing mode" of nuclear excitation is of special significance because knowledge of its excitation energy (EISGMR) provides direct information on the nuclear compressibility, K_{A}, as shown in Eq. 1.1

$$E_{\mathrm{ISGMR}} = \hbar\sqrt{\frac{K_{\mathrm{A}}}{m\langle r^2\rangle}}, \tag{1.1}$$

where m is the nucleon mass and $\langle r^2\rangle$ is the mean-square nuclear radius. The nuclear matter incompressibility coefficient, K_∞, is a very important physical quantity in the study of nuclei, supernova collapse, neutron stars and heavy-ion collisions, since it is directly related to the curvature of the nuclear matter Equation Of State (EOS) [Bla80].

Previous studies at both iThemba LABS (South Africa) and RCNP (Japan) revealed the systematic observation of fine structure and associated characteristic energy scales of the ISGQR and the IVGDR. These studies established that the main decay mechanism leading to fine structure is the coupling to low-lying surface vibration in the ISGQR [She04, She09] and Landau damping in the IVGDR [Jin14, Lat19]. A survey of the fine structure of the IVGDR in ^{40,42,44,48}Ca was recently performed at iThemba LABS using proton inelastic scattering at 200 MeV [Lat19]. Fine structure in the energy region of the IVGDR is visible in all the nuclei. A comparison of the results from both IVGDR and the ISGMR in the same set of calcium isotopes provides better insight into the behaviour of the giant resonance with increased neutrons in different giant resonances. This present study seeks to

characterise the fine structure in the ISGMR and determine the main mechanism that is responsible for damping following the corresponding characteristic scales as the number of neutrons increase in the calcium isotope chain. The nature of the characteristic energy scales present in ISGMR is not clear, since there has been discrepancies from different model predictions. In addition, the $J^\pi = 0^+$ level densities can be deduced and combined with the $J^\pi = 1^+$, 1^-, 2^+ and 2^- values from the other giant resonance studies. In this way, one can test the spin distribution in level-density models, especially the phenomenological Back Shifted Fermi Gas model [Egi05].

1.1 ISGMR in medium to low-mass range

By way of example, systematic studies of the ISGMR in the mass 90 region have been carried out particularly by two groups - the Texas A&M and the RCNP - using inelastic α-particle scattering at 240 MeV [You15, Kri15, You13] and 386 MeV [Gup16, How19], respectively. Youngblood *et al.* [You13] measured the ISGMR strengths in ^{90,92}Zr and ^{92}Mo using 240 MeV alpha-beam at small scattering angles, including 0°. Here, an unexpected variation in the shape of the extracted ISGMR strengths in ^{90,92}Zr and ^{92}Mo was observed. Specifically, the ISGMR energy for ^{90}Zr was reported to be 1.22 and 2.80 MeV lower than that for ^{92}Zr and ^{92}Mo, respectively, resulting in the K_{A} value increasing with increasing mass number. As such, Youngblood *et al.* [You13] concluded by attributing this anomalous effect to nuclear shell structure effects. This conclusion is contrary to expectation according to the hydrodynamic model which predicts the ISGMR energies increasing with mass number. In order to further investigate this anomaly, Guptal *et al.* [Gup16] carried out independent inelastic scattering measurements of the ISGMR responses in ^{90,92}Zr and ^{92}Mo with a 386 MeV alpha-beam at small scattering angles, including 0°, at the Research Center for Nuclear Physics (RCNP) in Japan. In Ref. [Gup16], the ISGMR strengths were extracted for these three nuclei using a combination of the Difference-of-Spectra (DoS) technique and Multipole Decomposition Analysis (MDA). Nearly similar ISGMR spectra were observed for the three nuclei as shown in Fig. 2 of [Gup16] which is reproduced here as Fig. 1.2. Guptal *et al.* [Gup16] concluded that the ISGMR energies and strengths for all three nuclei are similar within experimental uncertainty, ruling out any

contribution from nuclear structure effects to the nuclear compressibility. As such, discrepancies in the ISGMR strengths were attributed to the arbitrariness involved in the background-subtraction procedure employed in the TAMU work.

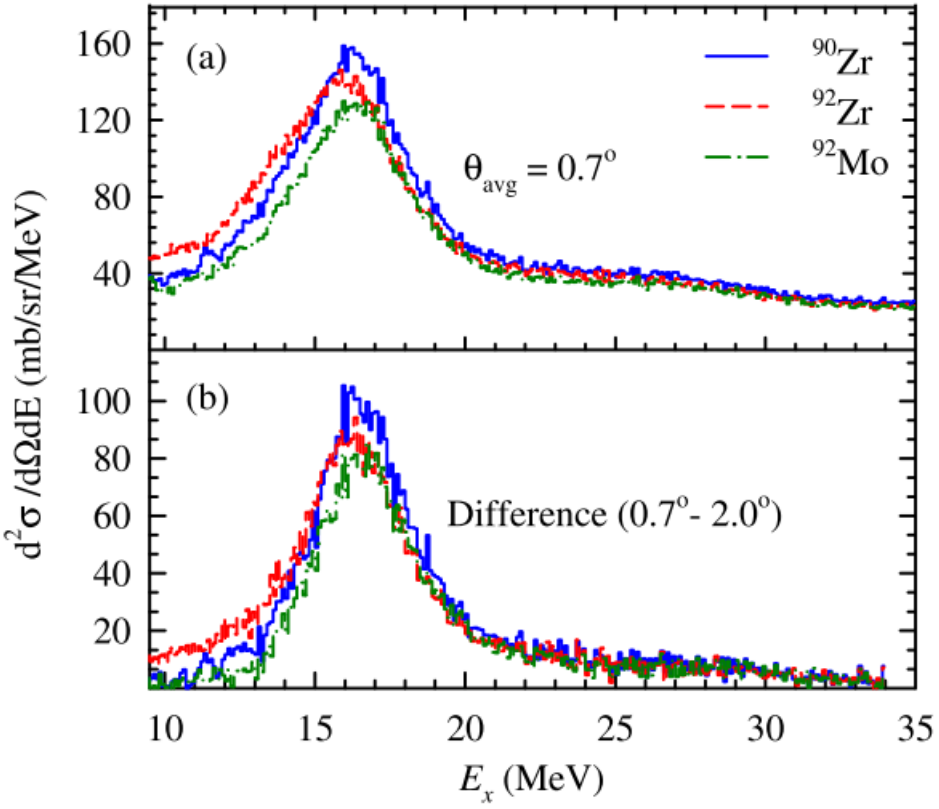


Figure 1.2: *Upper*: Double-differential cross sections measured at an averaged angle 0.7° for ^{90}Zr, ^{92}Zr and ^{92}Mo. *Lower*: Difference spectra of average angles 0.7° & 2.0° for the same nuclei. Taken from [Gup16]

Recently, in another experimental project at iThemba LABS, data were acquired to study ISGMR responses in heavy to low-mass nuclei. Part of the results from that measurements are shown in Fig. 1.3. In Fig. 1.3, an overview of giant resonance across the periodic table shows some compact ISGMR for ^{90}Zr which gets wider and starts to fragment for ^{58}Ni. Then very wide and fragmented for ^{24}Mg. But in calcium isotopes some fragmentation is seen with additional strength above the ISGMR region [Lui11] and is discussed in detail in the following section.

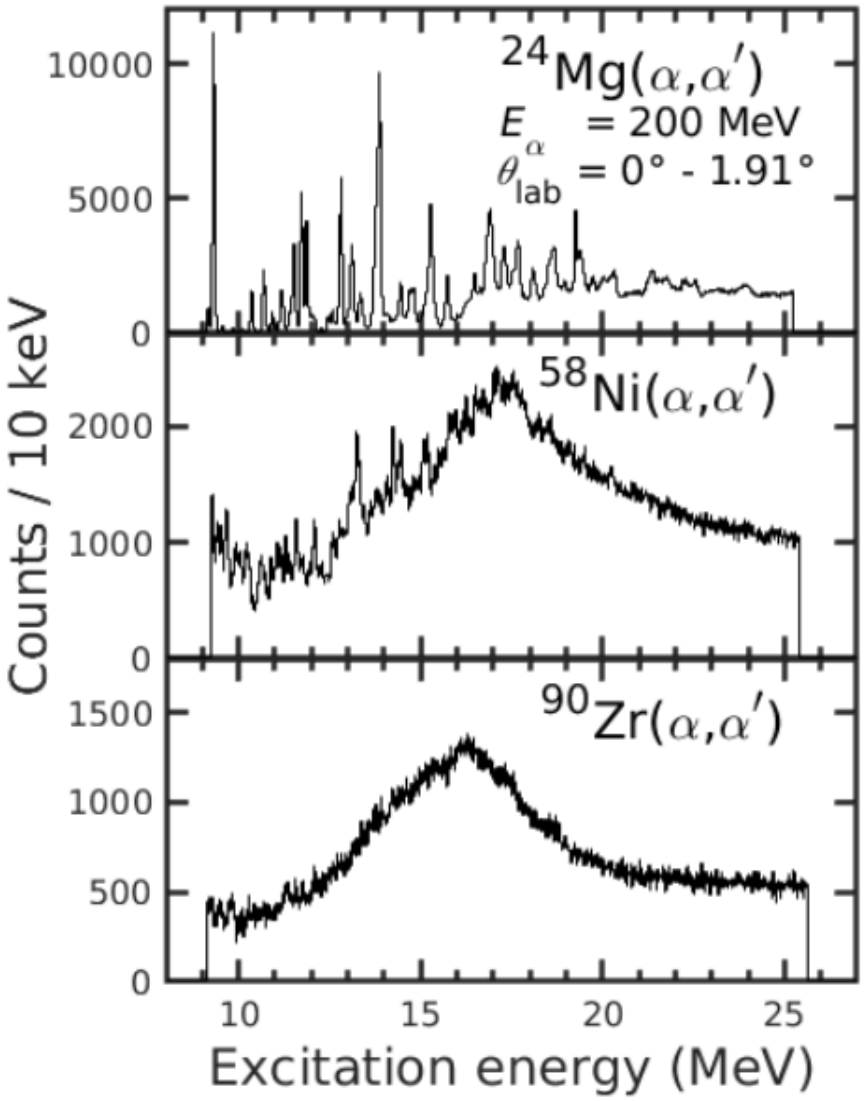


Figure 1.3: ISGMR response for ^{24}Mg, ^{58}Ni and ^{90}Zr at $E_\alpha = 200$ MeV and $\theta_{\text{Lab}} = 0°$. Taken from [Moo19].

1.2 ISGMR in calcium isotopes

The Isoscalar Giant Monopole Resonances (ISGMR) in the ^{40,44,48}Ca nuclei were studied at Texas A&M using inelastic scattering of 240 MeV α-particles at extreme forward scattering angles, including 0° [You97, Lui11, But17]. These measurements found that the ISGMR centroid energy (E_{ISGMR}) for ^{48}Ca was 0.7 MeV higher than in the case of ^{40}Ca [Lui11, And13]. On the other hand, the theoretical calculations using Random Phase Approximation (RPA) predict a lower centroid energy in ^{48}Ca as shown in Fig. 4 of [But17] which is reproduced here as Fig. 1.4. Again, Lui *et al.* [Lui11] concluded by attributing these

anomalous findings to contributions from the nuclear structure effects. Later in 2019, in an attempt to verify and elucidate these unsual phenomena, the RCNP group carried out independent ISGMR measurements using inelastic scattering of 386 MeV α-particles on ^{40,42,44,48}Ca at extreme forward scattering-angles, including 0° and the results were reported in [How20]. However, in Howard et al. [How20] it was established that the ISGMR strength distributions, and the metrics that are generally used to characterise the excitation energy of the response follow expected trends. Hence, there are no local nuclear structure effects on the ISGMR strength distribution in the calcium region of the nuclear chart.

In addition, in order to investigate further the unexpected characteristics of the ISGMR in ^{40}Ca and ^{48}Ca as reported by [Lui11], independent measurements of the ISGMR responses of ^{40,42,44,48}Ca were carried out using the inelastic scattering of 200 MeV α-particles at 0° and 4°. The results are presented in this thesis. The experiment was carried out using the K600 magnetic spectrometer at iThemba Laboratory for Accelerator Based Sciences (LABS) in South Africa.

Discrepancies in the ISGMR strengths were attributed to the arbitrariness involved in the background-subtraction procedure employed in the TAMU work. The TAMU group always employ an empirical background assuming that it has the shape of a straight line in the higher excitation-energy region, joining onto a Fermi shape at low excitation energy to model particle threshold effects [You01, Gar18]. An example of such guessed background is shown in Fig. 1 of [Lui11] which is reproduced here as Fig. 1.5. The challenge with such a background subtraction method is that it gives an additional monopole strength above the ISGMR region which results in an incorrect K_{A} value. As demonstrated by Gupta *et al.* [Gup16] and shown in Fig. 1.2, the DoS technique does not need a guessed background subtraction from measured 0° data. This approach resolved the problem of incompressibility reported by the TAMU group in the mass 90 region. In the case of ^{48}Ca, Lui *et al.* [Lui11] extracted the ISGMR strength using the MDA. A typical result of the MDA is shown at the top left-hand-side panel of Fig. 4 of Ref. [Lui11] which is reproduced here as Fig. 1.6. It is worth noting that the MDA is as reliable as the shape of background used. The guessed background shaped adopted by the TAMU group has been shown to

be unreliable by the RCNP group in when determining monopole strength in the higher excitation-energy region. Thus, the DoS technique is taken to be most reliable option for obtaining the ISGMR and additional $E0$ strength above the resonance.

The present project uses the K600 magnetic spectrometer with Zero-degree Facility. Unfortunately, due to limitations in the ion optics, there is no angle resolution within 0°-2° acceptance angle. However, this has been overcome by adapting the DoS technique in order to subtract a portion of the measured 4°$\pm$ 2° data from the measured 0° data. Noting that in the present case of calcium isotopes, the $L = 0$ angular distribution for ^{48}Ca(α,α') at $E_\alpha = 240$ MeV, as seen in Fig. 1.6, exhibits a maximum at $\theta_{\text{c.m.}} = 0°$ and a deep minimum at $\theta_{\text{c.m.}} = 3.5°$. The corresponding angular distributions for the present case of ^{40,42,44,48}Ca(α,α') at $E_\alpha = 200$ MeV are almost identical to those in Fig. 1.6. Here, the sum of all multipoles except $L = 0$ is essentially flat across an angle range $\theta_{\text{c.m.}} = 0°$ to 5°. This allows for an angle cut around the $L = 0$ deep minimum at $\theta_{\text{c.m.}} \approx 3.3°$ to be used as a subtraction for all other multipoles as "background" in the 0° data, leaving only the $E0$ strength.

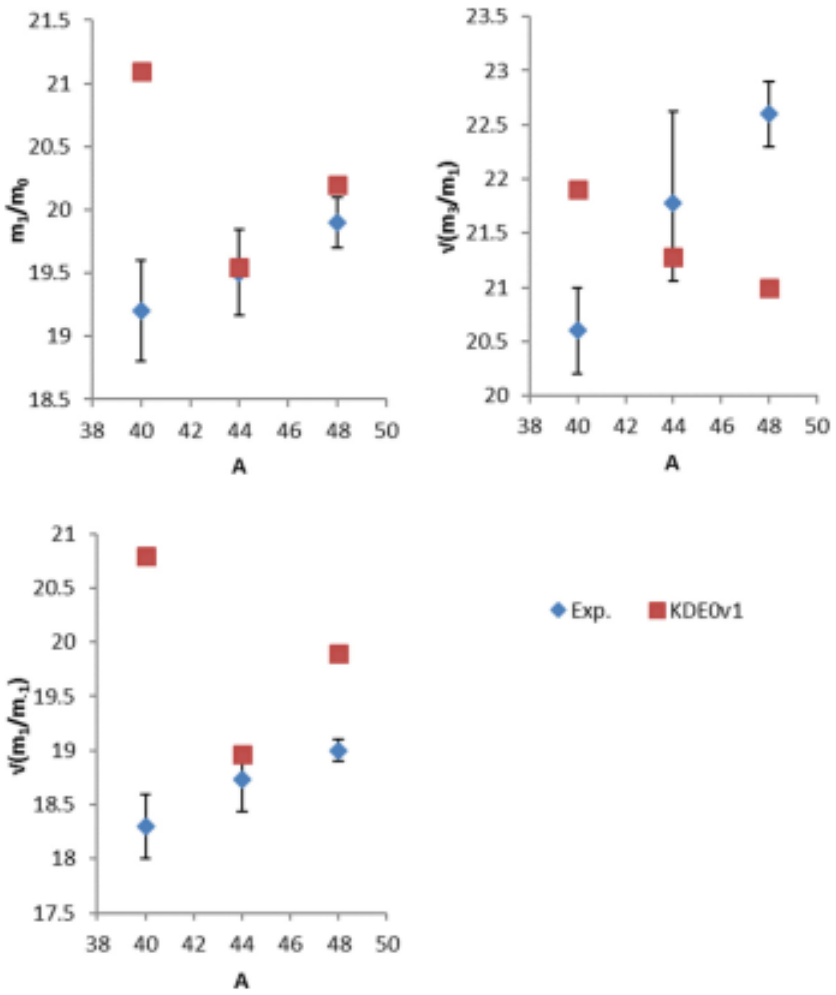


Figure 1.4: Experimental results for the ISGMR energies in ^{40}Ca [You97], ^{44}Ca [But17], and ^{48}Ca [Lui11] (blue diamonds) are compared with theoretical predictions (red squares). Here, $\sqrt{m_1/m_{-1}}$ (left panel down), m_1/m_0 (top left panel) and $\sqrt{m_3/m_1}$ (top right panel) are the constrained energy, centroid energy and scaling energy, respectively. Taken from [But17].

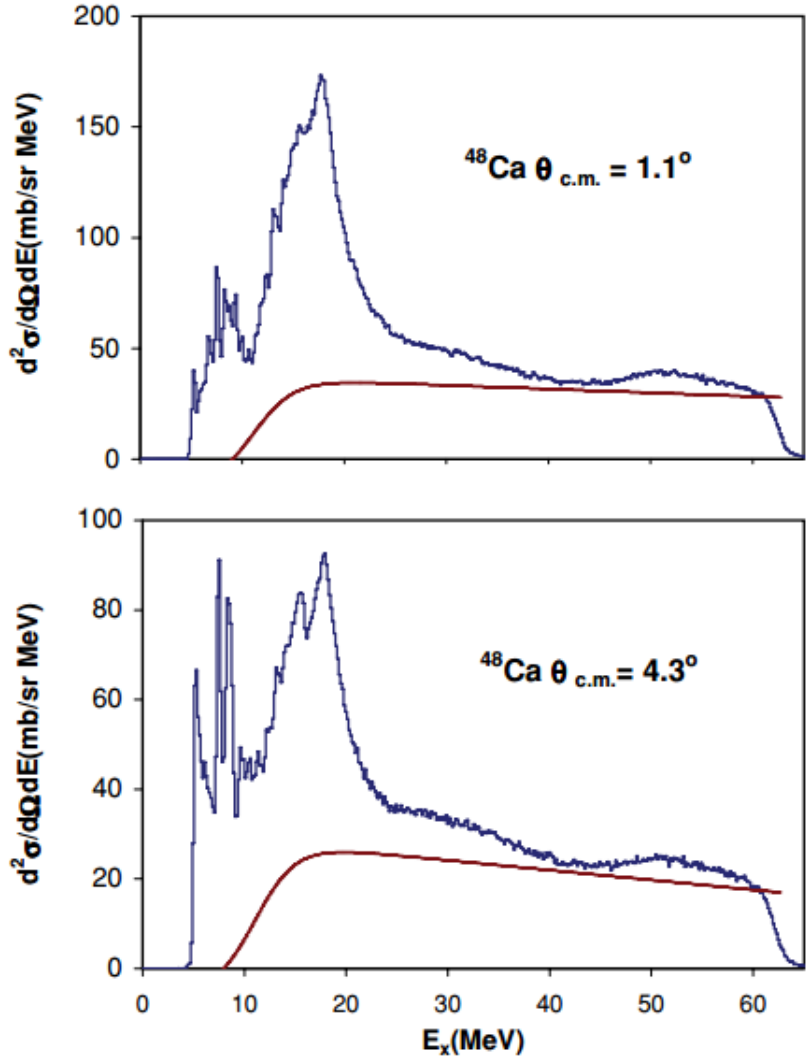


Figure 1.5: Inelastic alpha scattering spectra at $E_\alpha = 240$ MeV and $\theta_{\text{c.m.}} = 1.1°$ and $4.3°$ for ^{48}Ca. Taken from [Lui11].

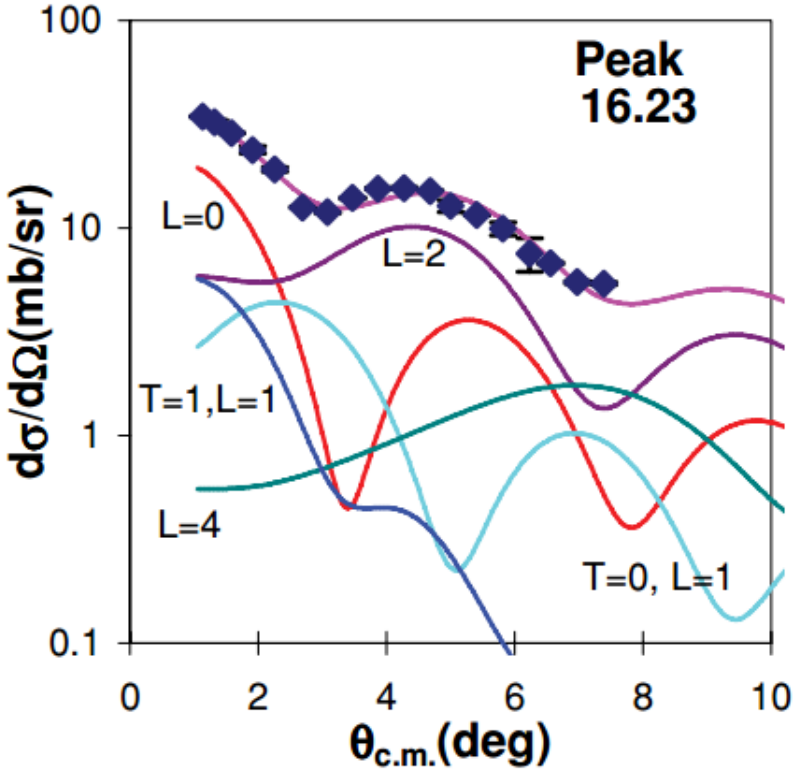


Figure 1.6: The angular distributions of the ^{48}Ca cross section at $E_{\mathrm{x}} = 16.23$ MeV from the TAMU work. Taken from [Lui11].

1.3 Present work

Various studies on giant resonances via high energy-resolution inelastic particle-scattering experiments have established fine structure as a generic phenomenon of nuclei irrespective of the mode [Kuh81, Kal06, Usm11]. The observed fine structure provides valuable information about factors that contribute to the decay of giant resonances. Specifically, at the iThemba Laboratory for Accelerator Based Sciences (iThemba LABS), a series of experimental studies using proton scattering has established the systematic observation of fine structure of the ISGQR and IVGDR [She08, Usm11, Jin18, Kur18, Don18, Lat19]. The present study seeks, for the first time, to answer the question regarding observation of fine structure phenomenon for the ISGMR in calcium isotopes. In order to achieve this goal, Inelastic α-particle scattering measurements, with $E_\alpha = 200$ MeV and $\theta_{\text{Lab}} = 0^\circ$ and 4°, were carried out on ^{40,42,44,48}Ca targets using the K600 magnetic spectrometer and the Separated Sector Cyclotron (SSC) facility at iThemba LABS. Also, in order to fully understand the origin and nature of the observed fine structure, characteristic energy scales are extracted from the experimental data via the Continuous Wavelet Transform (CWT) technique, and the results are compared with appropriate theoretical models. A visual inspection of all the figures showing excitation-energy spectra from TAMU and RCNP works on calcium isotopes shows that their energy resolutions are comparable to the one obtained in this work, which is $\Delta E = 85$ keV. However, because the two group uses the MDA technique which required that the spectra be re-binned to either 750 keV or 1 MeV, no attention was paid to the fine structure. In contrast, a major focus of this present work is to compare experimental energy scales obtained in this project to those found in a similar analysis of theoretical predictions in order to determine, for the first time, major damping mechanisms in the ISGMR region.

Another important information that can be extracted from experimental study of giant resonances is the nuclear level densities of states. Nuclear level densities are imperative for the study of nuclear reactions. Their applications include astrophysics, the study of nuclei far from the stability line, and reactor physics [Agv03]. In the present work, the extraction of level densities of the dominant 0^+ states in the excitation-energy region of the ISGMR in calcium isotopes is possible and is compared to theoretical values from

approaches based on the phenomenological Back Shifted Fermi Gas (BSFG) model, the microscopic Hartree Fock-Bardeen-Cooper-Schrieffer (HF-BCS) and Hartree Fock- Bogoluibov (HFB) calculations.

The layout of this thesis is as follows:
Chapter 2 provides a detailed overview of the necessary theoretical considerations in the study of nuclear giant resonances with a focus on the Isoscalar Giant Monopole Resonance (ISGMR). Various theoretical models used in microscopic description of the monopole strength function are briefly described. Also presented in this chapter is a short description of the theoretical models required for the extraction of characteristic energy scales and the nuclear level density.

Chapter 3 provides a detailed account of the experimental procedure for both 0° and 4° measurements. Detailed explanation of offline data analysis and extraction is presented.

Chapter 4 presents the analysed experimental data and the theoretical predictions. A detailed step-by-step procedure of extracting the $E0$ strength via the Different-of-Spectra (DoS) is presented. Extracted characteristic energy scales from the experimental data and the theoretical calculations together with the extracted spin-dependent $J^\pi = 0^+$ level densities are presented and discussed.

Chapter 5 deals with the conclusions and recommendations.

Chapter 2

Theoretical considerations

This chapter outlines the relevant theoretical considerations for this study. A general description of nuclear giant resonances is provided with a specific focus on the Isoscalar Giant Monopole Resonance (ISGMR) and its properties. Also contained in this chapter are details regarding the model predictions of giant resonance behaviour as well as the description of the technique for extracting the characteristic energy scales. The chapter ends with a description of the techniques employed for extracting the $J^{\pi} = 0^{+}$ level density.

2.1 Giant resonances

Giant resonances are simple, collective, particle-hole excitations of the nucleus. These modes correspond to the collective motion of nuclei. Quantum mechanically they are observed as resonances corresponding to a transition between the ground state and the collective states. The strength of the transition is descibed by a transition amplitude and it depends on the number of participating nucleons as well as the size of the system. As a result, a limit is placed on the total transition strength by a sum rule which rely solely on the ground state properties of the nucleus. If a given resonance exhausts more than 60 % of the corresponding sum rule (total transition strength) then it is called a Giant Resonance (GR) [Har01].

2.1.1 Macroscopic description of giant resonances

Macroscopically, giant resonances are classified based on three main quantum numbers. The first is the multipolarity L, with $\Delta L = 0$ (monopole resonance), $\Delta L = 1$ (dipole resonance), $\Delta L = 2$ (quadrupole resonance) etc. [Har01] (see Fig. 2.1). The second quantum number is the spin S. The $S = 0$ mode describes a situation with no spin excitation and it is called an electric mode, while $S = 1$ refers to a mode with spin excitation and it is called magnetic. The third is the isospin T, with $T = 0$ refering to a mode with no isospin excitation and it is called an isoscalar mode while $T = 1$ involving isospin excitation is referred to an isovector mode.

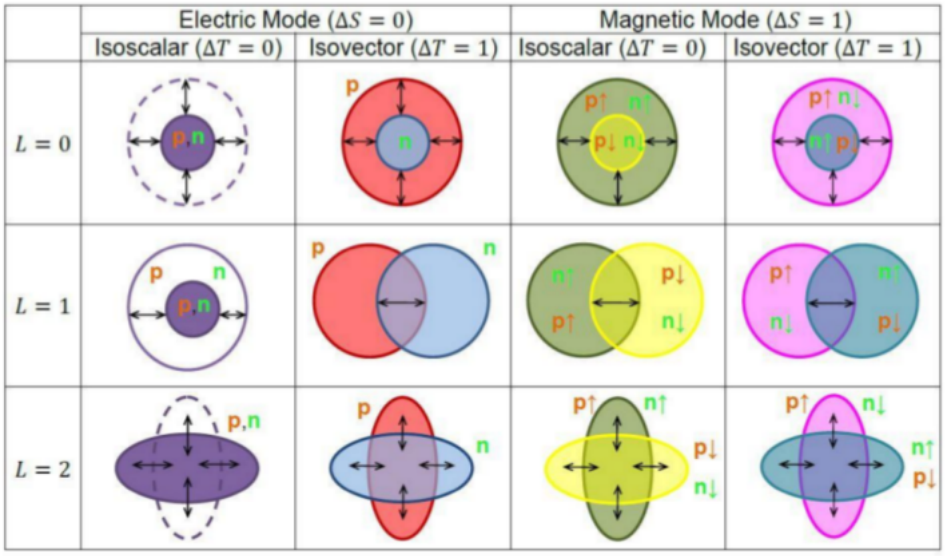


Figure 2.1: Schematic picture of various collective modes, taken from [Don16]

The electric isoscalar vibrational modes, denoted as $\Delta S = 0$, $\Delta T = 0$, correspond to vibrations in which the protons and neutrons move in phase with each other. The multipolarity pattern for this type of mode is defined by $\Delta L = 0, 2$, and so forth. On the other hand, the electric isovector modes, $\Delta S = 0$, $\Delta T = 1$, describe a vibration in which the protons and neutrons move out of phase against each other.

Similarly, the magnetic isoscalar modes, denoted by $\Delta S = 1$, $\Delta T = 0$, refer to vibrations in which the nucleons with spin-up oscillate against nucleons with spin-down, and the corresponding multipolarities are $\Delta L = 0, 1, 2$ and so forth. Finally, the magnetic isovector vibrational modes, given as $\Delta S = 1$, $\Delta T = 1$, are modes with spin-up (-down) protons vibrating against spin-down

(-up) neutrons.

2.1.2 Microscopic description of giant resonances

Giant resonances are described microscopically as a coherent overlap of many one-particle-one-hole (1p–1h) excitations built upon the ground state. Such excitations result from the operation of a one-body operator Q, on the nucleus' ground state $|\Psi_{g.s.}\rangle$.

$$|\Psi_{GR}^{L,\sigma,\tau}\rangle = Q^{L,\sigma,\tau}|\Psi_{g.s.}\rangle \tag{2.1}$$

where L, σ and τ represent the multipolarity, spin and isospin of the resonance, respectively. For example, the operator for the electric isoscalar excitation ($\sigma = 0$, $\tau = 0$) can be taken as:

$$Q_M^{L,0,0} = \sum_{i=1}^{A} r_i^L Y_{LM}(\hat{r_i}), L \geq 2, \tag{2.2}$$

where the summation runs over all nucleons i. The generally acceptable form of operators for the Isoscalar Giant Monopole Resonance (ISGMR) and Isoscalar Giant Quadrupole Resonance (ISGQR) excitations are shown as Eqs. (2.3) and (2.4), respectively.

$$Q_M^{0,0,0} = \frac{1}{\sqrt{4\pi}} \sum_{i=1}^{A} r_i^2, \tag{2.3}$$

$$Q_M^{2,0,0} = \frac{Z}{A} e \sum_{i=1}^{A} r_i^2 Y_{2M}(\hat{r_i}). \tag{2.4}$$

The shell-model concept of giant resonances, as shown in Fig. 2.2, is a viable tool that can be used to study and understand the qualitative features of the giant resonances [Har01]. There are two main distinctive attributes of this model. One, the single-particle wave functions in subsequent shells N, $N+1$, $N+2$, $N+3$,... possess alternating parity. The second is that the energies of these major shells are separated by $\Delta E = \Delta N \times 1\hbar\omega = \Delta N \times 41A^{-1/3}$ MeV. The operator in Eq. (2.2) can only generate transitions with $\Delta N \leq L$ while, parity conservation requires that odd L transition occur only when $\Delta N = 1$, 3, ... and $\Delta N = 0$, 2, ... for even L transfer. This results in a simple scheme shown in Fig. 2.2 with corresponding resonance energies as shown in Table 2.1.

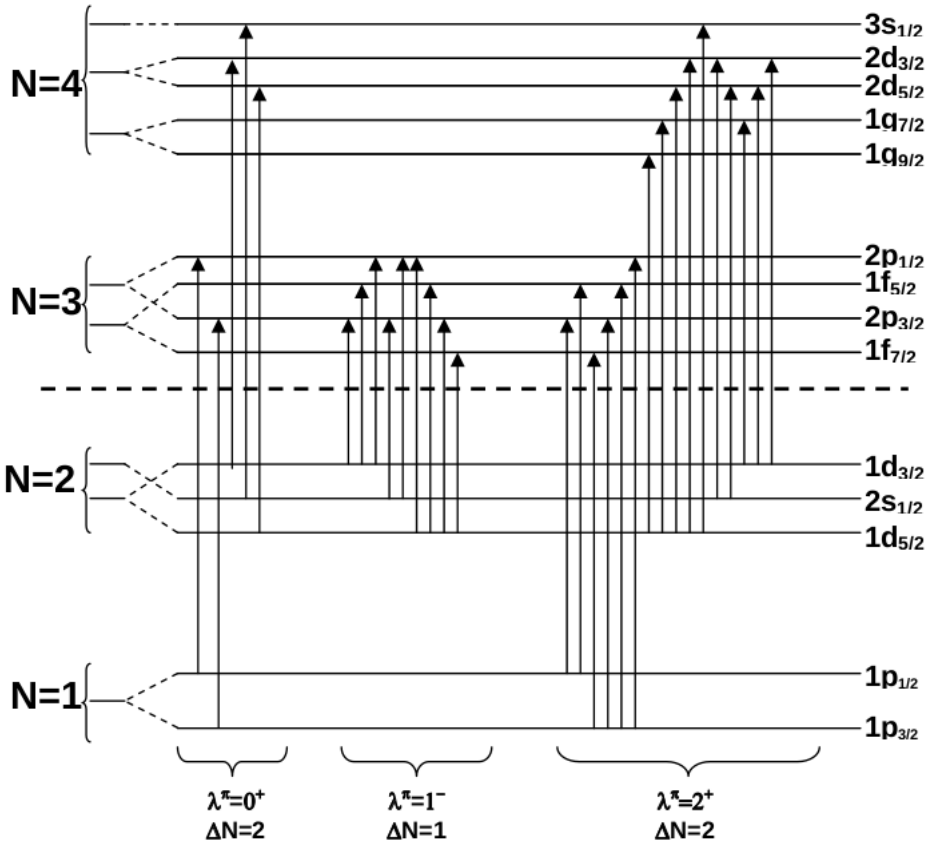


Figure 2.2: Schematic representation of $E0$, $E1$ and $E2$ single-partice transitions between shell-model states, taken from [She04].

The presence of a residual p-h interaction results in the formation of a collective state. This state, which is a coherent overlap of all p-h states of a given L and parity, exhaust the sum rule. Since the residual p-h interaction is attractive for isoscalar and repulsive for isovector excitations, the isoscalar will be located below and the isovector above the corresponding unpertubed energies $\Delta N \times 41 A^{-1/3}$ MeV. Actually, experimental results show that the $2\hbar\omega$ ISGMR and the $1\hbar\omega$ IVGDR are located almost at the same excitation energy. This overlap in many resonances' excitation energy must be disentangled, and hence the need to use specific probes to selectively excite only one type of resonance. A major example is the use of α-particles as probe to excite ISGMR as reported in this study.

Table 2.1: Multipole excitations as p-h excitations across major shells [Har01].

Resonance	Multipolarity	Resonance energy (MeV)
Monopole	$L = 0$	$(0\hbar\omega)$, $2\hbar\omega$
Dipole	$L = 1$	$1\hbar\omega$
Quadrupole	$L = 2$	$(0\hbar\omega)$, $2\hbar\omega$
Octopole	$L = 3$	$1\hbar\omega$, $3\hbar\omega$
Hexadecapole	$L = 4$	$(0\hbar\omega)$, $2\hbar\omega$, $4\hbar\omega$

2.1.3 Isoscalar giant monopole resonance

Macroscopically, the isoscalar giant monopole resonance, which is also referred to as 'breathing' or compression mode, can be described as a radial oscillation of the nucleus as a whole. It is characterised by selection rules $\Delta L = 0$, $\Delta S = 0$ and $\Delta T = 0$, where L, S and T are the angular momentum, spin and isospin of the nucleons involve respectively. This present study seeks to know, through inelastic α-particle scattering, what is responsible for the fine structure in the Isoscalar Giant Monopole Resonance (ISGMR) as the number of neutron increases in calcium isotopes and to further investigate the nature of characteristic energy scales present in the ISGMR.

The ISGMR was first discovered by Harakeh *et al.* [Har77] through inelastic α-particle scattering at forward scattering angles on ^{208}Pb, and later in the same year its classification as a $\Delta L = 0$ mode was established through a similar experiments by Youngblood *et al.* [You77]. Since then ISGMR has been extensively studied, mainly by inelastic α-particle scattering at very forward scattering angles including 0° and at an energy up to 400 MeV (see [You99, Gup16] and the references therein). From the many years of study on the ISGMR, certain properties of this mode has been established. Firstly, for nuclei with A $\geq$ 90, the strength distribution is gaussian with the centroid energy approximately at $80\mathrm{A}^{-1/3}$ MeV and with increasing width from about 2.5 MeV in Pb region to about 4 MeV for A = 90. The strength distribution is fragmented in sd-shell nuclei and broader in deformed nuclei than in spherical ones. Secondly, for lighter nuclei (A $\leq$ 90), the strength distribution is fragmented and overlaps with structures from pick-up or break-up processes [Har01].

The study of the isoscalar giant monopole resonance is important for two

main reasons: one, because of its intrinsic interest like other collective modes, and two, because of the direct relationship between its excitation energy and the incompressibility of the nucleus (denoted as K_{A}) from which the incompressibility of the nuclear matter K_{nm} can be derived by extrapolation. The latter reason makes the ISGMR to be of astrophysical interest.

The ISGMR is studied experimentally using hadronic probes such as (p,p'), (α, α') and inelastic scattering of heavy ions at very forward scattering angles including 0°. The most preferred probe is the α-particle which is an $S = 0$, $T = 0$ probe. To first order the (α, α') reaction will only excite isoscalar ($\Delta S = 0$, $\Delta T = 0$) modes. It has been shown that (α, α') can also excite the IVGDR, however, the contribution is very small at α-particle energies at or below 250 MeV [Shl87].

2.2 Damping width and decay of giant resonances

Giant resonances decay mainly by particle emission (protons, neutrons and α-particles) because they are usually located above the particle-decay threshold. Study of the giant resonance decay provides insight into the damping mechanisms responsible for the various collective modes. A giant resonance is described in terms of the three parameters which are the energy E, the width Γ and the strength S. Of these parameters, the width Γ is complex and special in the sense that its theoretical understanding requires the most complicated description. As a first approximation the total width of a giant resonance has three contributions:

$$\Gamma = \Delta\Gamma + \Gamma^{\uparrow} + \Gamma^{\downarrow}. \tag{2.5}$$

Here, $\Delta\Gamma$ is called Landau damping, which arises from the interaction between the correlated particle-hole excitation with uncorrelated particle-hole configurations in the same excitation-energy range causing a fragmentation of the correlated wave-function. Here, $\Gamma^{\uparrow}$ is the escape width and it is associated with the coupling of the correlated 1p-1h state to the continuum. Also, $\Gamma^{\downarrow}$ is the spreading width acquired by the giant resonance as a result of the mixing of the correlated 1p-1h state with more complex and

very many 2p-2h configurations. This coupling can progress to even more complex (3p-3h)...(np-nh) configurations until the system reachs equilibrium and a compound nucleus is formed. It is possible to have particle decay before the fully equilibrated system is formed. The total spreading width can be written as:

$$\Gamma^{\downarrow} = \Gamma^{\downarrow\uparrow} + \Gamma^{\downarrow\downarrow}, \tag{2.6}$$

where $\Gamma^{\downarrow\uparrow}$ is the partial width arising from the decay of 2p-2h states by particle emission at the intermediate level, and $\Gamma^{\downarrow\downarrow}$ is the partial width for statistical decay of the compound nucleus.

2.2.1 Microscopic models for the damping of the ISGMR

Many microscopic models have been developed to explain the nuclear structure in general and especially the microscopic structure of giant resonances. These models are based on the mean field approach, in which the nucleons in the ground state are considered to move independently from each other in shells that are completely occupied up to the respective Fermi levels for protons and neutrons. In excited states the models take into account the modification of the mean field owing to collective vibrations.

2.2.1.1 Random Phase Approximation (RPA)

The Random Phase Approximation (RPA), which was first established by Bohm and Pines [Boh51], is one of the many microscopic models employed in the description of giant resonances. The model treats giant resonances as a coherent superposition of 1p-1h excitation in nuclei built on a correlated ground state. On a particle-hole (p-h) basis, the RPA equation is given as [Tho61]

$$\begin{pmatrix} A & B \\ -B^* & -A^* \end{pmatrix} \begin{pmatrix} X_{ph} \\ Y_{ph} \end{pmatrix} = E_{ph} \begin{pmatrix} X_{ph} \\ Y_{ph} \end{pmatrix}, \tag{2.7}$$

where the matrixes A and B are defined as

$$A_{php'h'} = \varepsilon_{ph}\delta_{pp'}\delta_{hh'} + \left(\frac{\delta h_{ph}}{\delta \rho_{p'h'}}\right)_0; \qquad B_{php'h'} = \left(\frac{\delta h_{ph}}{\delta \rho_{p'h'}}\right)_0. \tag{2.8}$$

The nuclear excitation spectrum in response to a hadronic external perturbation

$$\hat{F} = \sum_{ph} f_{ph} a_p^\dagger a_h \tag{2.9}$$

is given by the strength function $S_F(\omega)$

$$S_F(\omega) = -\pi^{-1} \sum_{php'h'} f_p^* R_{php'h'}(\omega) f_h, \tag{2.10}$$

where $a_p^\dagger$ and a_h are the creation and annihilation operators, and $R_{php'h'}$ is the ph propagator. In terms of the RPA matrices $R_{php'h'}$ is given as

$$R_{php'h'}(\omega) = \begin{pmatrix} \omega + i\eta - A & B \\ -B^* & -\omega + i\eta - A^* \end{pmatrix}^{-1}. \tag{2.11}$$

Given the p-h states and interaction, RPA gives the collective phonons. The RPA can describe the centroid energies and Landau damping well. In a continuum implementation it also describes the escape width but it does not describe the spreading width nor the corresponding fine structure [Har01, Pap19]

2.2.1.2 Second RPA (SRPA)

The Second RPA (SRPA) extends beyond the 1p-1h RPA by incorporating coupling to the 2p-2h states [Dro86]. It has successfully been applied to describe nuclear damping processes [Yan86] and in particular the spreading width in the decay of giant resonances [Dro86, Ada84]. An expanson of Eq. (2.7) to include also 2p-2h excitations gives the SRPA equations:

$$\begin{pmatrix} A & B & A_{12} & 0 \\ -B^* & -A^* & 0 & -A_{12}^* \\ A_{21} & 0 & A_{22} & 0 \\ 0 & -A_{21}^* & 0 & -A_{22}^* \end{pmatrix} \begin{pmatrix} X_{ph} \\ Y_{ph} \\ X_{2p2h} \\ Y_{2p2h} \end{pmatrix} = E_{2p2h} \begin{pmatrix} X_{ph} \\ Y_{ph} \\ X_{2p2h} \\ Y_{2p2h} \end{pmatrix}, \tag{2.12}$$

where A and B are the normal RPA matrices, A_{12} describes the coupling between 1p-1h and 2p-2h states and A_{22} containes the 2p-2h states and their interactions. On its diagonal A_{22} contains the unperturbed 2p-2h energies. The SRPA calculations are based on the Hartree-Fock ground state (self consistent mean field and corresponding single-particle states). The same interaction

used in Hartree-Fock is used to calculate also the matrix elemnts of SRPA. A model space of 13 harmonic-oscillator shells is used. The interaction used is the Unitary Correlation Operator Method (UCOM) two-nucleon interaction based on the Argonne V18 potential and fitted only to few-nucleon systems. In SRPA the subtraction method is used in order to preserve the rather good GMR centroids predicted by RPA.

Note that, unlike SRPA implementations based on phenomenological interactions, the UCOM-SRPA is based on "undressed" single-particle states, corresponding to low effective mass. It is also based on an uncorrelated ground state. As a result, the fragmentation is weaker than in the case of, e.g., [Dro86] etc. It describes an average quenching effect rather than details of the fragmentation.

The first large-scale applications of SRPA, as in this work, can be found in [Pap09, Usm11]. A detailed description of the SRPA formalism is provided in [Pap10].

2.2.1.3 Quasi-particle RPA (QRPA)

Also built on the RPA, the Quasi-particle Random Phase Approximation (QRPA) allows one to treat the particle-particle (p-p), particle-hole (p-h) and hole-hole (h-h) excitations on the same footing. Unlike the SRPA, it is applicable to both closed and open-shell nuclei. The QRPA equation is given as:

$$\begin{pmatrix} A & B \\ B & A \end{pmatrix} \begin{pmatrix} X_n \\ Y_n \end{pmatrix} = \omega_n \begin{pmatrix} X_n \\ -Y_n \end{pmatrix}, \tag{2.13}$$

where ω_n is the energy of the QRPA excited state $\langle n \rangle$. For closed-shell nuclei (here: ^{40}Ca and ^{48}Ca) and if the same interaction is used, QRPA is the same as RPA [Pap19]. However, this is not the case in the present calculations, because very different interactions are used. Detailed solutions of Eq. (2.13) are provided in [Pap07].

2.2.1.4 Quasiparticle Time Blocking Approximation (QTBA)

The Quasiparticle Time Blocking Approximation (QTBA), developed originally in Ref. [Lit08], is a theoretical approach based on covariant density functional theory (CDFT), in which two-quasiparticles and vibrational modes excitations are taken into account. The model has been proven to be one of the most successful microscopic descriptions of nuclear structure and dynamics. RQTBA is ususally expessed in terms of *ph*-type components of the nuclear response function $\tilde{R}(\omega)$ by the following equation [Lit08, Ego16]:

$$R^{\eta\eta'}_{k_1k_4,k_2k_3}(\omega) = \tilde{R}^{(0)\eta}_{k_1k_2}(\omega)\delta_{k_1k_3}\delta_{k_2k_4}\delta_{\eta\eta'} + \tilde{R}^{(0)\eta}_{k_1k_2}(\omega) \times \sum_{k_2k_4''} \bar{W}^{\eta\eta''}_{k_1k_6,k_2k_5}(\omega) R^{\eta''\eta'}_{k_5k_4,k_6k_3}(\omega), \tag{2.14}$$

where the index k formally runs over all single-quasiparticle states, and the index numerates forward (+) and backward (-) components of the matrix elements in the Nambu space. Here, $\tilde{R}^{(0)}(\omega)$ represents the propagation of 2-quasiparticles in the mean field between acts of interaction with the following amplitudes:

$$\bar{W}^{\eta\eta''}_{k_1k_4,k_2k_3}(\omega) = \tilde{V}^{\eta\eta''}_{k_1k_4,k_2k_3} + \left(\Phi^{\eta}_{k_1k_4,k_2k_3}(\omega) - \Phi^{\eta}_{k_1k_4,k_2k_3}(0)\right)\delta_{\eta\eta''}. \tag{2.15}$$

In addition, $\tilde{V}$ is the relativistic mean field (RMF) interaction amplitude, and $\Phi^{\eta}(\omega)$ is the interaction amplitude in the QTBA responsible for the particle-phonon coupling with the particle-hole (= +) and hole-particle (η = -) components. More details about the formalism can be found in Refs. [Lit08, Ego16].

2.2.1.5 Phonon-Phonon Coupling (PPC)

The phonon-phonon coupling (PPC) formalism has been discussed in detail in [Sev04, Sev12, Ars17] and it is presented here briefly for completeness.

To build the (Q)RPA equations on the basis of HF-BCS quasiparticle states with the residual interactions is a standard procedure [Ter05]. The dimensions of the (Q)RPA matrix grow rapidly with the size of the nucleus. Using the finite rank separable approximation (FRSA) [Gia98] for the residual interactions, the eigenvalues of the (Q)RPA equations can be obtained as the roots of a

relatively simple secular equation [Sev08]. Making use of the FRSA for the residual interaction enables one to perform (Q)RPA calculations in very large two-quasiparticle spaces. In particular, the cutoff in the discretized single-particle continuum can be chosen at 100 MeV. Using the general scheme of the Quasiparticle-Phonon Model (QPM) [Sol92] with Skyrme-type interactions as inputs, the Hamiltonian can be diagonalized in a space spanned by states composed of one and two (Q)RPA phonons [Sev04]

$$\Psi_\nu(\lambda\mu) = \Bigg(\sum_i R_i(\lambda\nu) Q^+_{\lambda\mu i} + \sum_{\lambda_1 i_1 \lambda_2 i_2} P^{\lambda_1 i_1}_{\lambda_2 i_2}(\lambda\nu) \left[Q^+_{\lambda_1\mu_1 i_1} Q^+_{\lambda_2\mu_2 i_2} \right]_{\lambda\mu} \Bigg) |0\rangle, \tag{2.16}$$

where λ denotes the total angular momentum and μ its z-projection in the laboratory system. The ground state is the (Q)RPA phonon vacuum $|0\rangle$. The unknown amplitudes $R_i(\lambda\nu)$ and $P^{\lambda_1 i_1}_{\lambda_2 i_2}(\lambda\nu)$ are determined from the variational principle, which leads to a set of linear equations [Sev04, Sev12]

$$(\omega_{\lambda i} - E_\nu) R_i(\lambda\nu) + \sum_{\lambda_1 i_1 \lambda_2 i_2} U^{\lambda_1 i_1}_{\lambda_2 i_2}(\lambda i) P^{\lambda_1 i_1}_{\lambda_2 i_2}(\lambda\nu) = 0, \tag{2.17}$$

$$2(\omega_{\lambda_1 i_1} + \omega_{\lambda_2 i_2} - E_\nu) P^{\lambda_1 i_1}_{\lambda_2 i_2}(\lambda\nu) + \sum_i U^{\lambda_1 i_1}_{\lambda_2 i_2}(\lambda i) R_i(\lambda\nu) = 0. \tag{2.18}$$

The rank of the set of linear equations (2.17) and (2.18) is equal to the number of one- and two-phonon configurations included in the wave function (2.16). Its solution requires to compute the Hamiltonian matrix elements coupling one- and two-phonon configurations:

$$U^{\lambda_1 i_1}_{\lambda_2 i_2}(\lambda i) = \langle 0 | Q_{\lambda i} H \left[Q^+_{\lambda_1 i_1} Q^+_{\lambda_2 i_2} \right]_\lambda |0\rangle. \tag{2.19}$$

Equations (2.17) and (2.18) have the same form as the QPM equations [Sol92], where the single-particle spectrum and the residual interaction are derived from the same Skyrme interaction.

In the present work, the single-particle spectrum and the parameters of the residual interaction are calculated with the SLy5 Skyrme force. In the case of the open-shell calcium isotopes, the pairing strength is taken equal to -270 MeVfm^3. This value of the pairing strength is fitted to reproduce the experimental neutron pairing gaps of ^{50,52,54}Ca obtained by the three-point formula [Ars17]. To construct the wave functions Eq. (2.16) of the 0^+ states, in the present study, all two-phonon configurations below 30 MeV are taken into account, these are built from the (Q)RPA phonons with different multipoles $\lambda^\pi = 0^+$, 1^-, 2^+, 3^-, 4^+, and 5^- coupled to 0^+.

2.2.2 Distorted-wave Born Approximation (DWBA)

It has been established that inelatstic scattering selectively populates rotational and vibrational collective states [Har01]. The Distorted-wave Born Approximation (DWBA) is required to determine the inelastic scattering differential cross-section, which can then be used to calculate the strength distribution of the giant resonance. A comprehensive explanation of how the DWBA formalism is implemented within the Optical Model potential is provided by Satchler and Khoa [Sat72]. Only salient points are provided in this section.

In general, for a 2-body direct reaction $A(a,b)B$, with an entrance channel α for partition $a+A$ and exit channel β for partition $b+B$, the total Hamiltonian can be expressed as

$$H = H_\alpha + K_\alpha + V_\alpha, \tag{2.20}$$

where H_α represents the internal Hamiltonians of a and A, K_α is the kinetic energy of the relative motion of a and A, and V_α their mutual interaction. The total wavefunction of the Hamiltonian is:

$$\Psi = \sum_\alpha \xi_\alpha(r_\alpha)\psi_\alpha(x_\alpha), \tag{2.21}$$

where ξ describes the relative motion of nuclei a and A. The total wavefunction contains incoming plane waves only in the ground-state α channel but will have outgoing spherical waves in all the channels which are opened at the given incident energy. It is denoted as $\Psi^{(+)}(k_\alpha)$, and can be expanded in terms of

the states of the exit channel β:

$$\Psi^{(+)}(\vec{k_\alpha}) = \sum_\beta \left(e^{i\vec{k_\alpha}.r\vec{\alpha}}\delta_{\alpha\beta} + f_{\beta\alpha}(\hat{r_\beta}, \vec{k_\alpha})\frac{1}{r_\beta}e^{ik_\beta.r_\beta} \right)\psi_\beta(x_\beta), \tag{2.22}$$

where $f_{\beta\alpha}$ is the scattering amplitude, and $\vec{k_\alpha}$ ($\vec{k_\beta}$) represents the relative momentum in channel α (β). For the reaction $A(a,b)B$ to be elastic or inelastic scattering, β and α must correspond to the partition. In that case the differential cross section is expressed as [Har01]:

$$\frac{d\sigma_{\beta\alpha}}{d\omega} = \frac{\mu_\beta\mu_\alpha}{4\pi^2\hbar^4}\left(\frac{k_\beta}{k_\alpha}\right)|T_{\beta\alpha}(\vec{k_\beta}, \vec{\alpha})|^2. \tag{2.23}$$

Here, μ_β and μ_α are the reduce masses in channels β and α, respectively, and $T_{\beta\alpha}$ is the transition amplitude and is expressed as

$$T_{\beta\alpha} = -\frac{2\pi\hbar^2}{\mu_\beta}f_{\beta\alpha}. \tag{2.24}$$

It is obvious, from Eq. (2.23), that the transition amplitude must be evaluted before the differential cross-section can be obtained. The expression for normalised $T_{\beta\alpha}$ can be generated by solving the Schrndinger equation, using an appropriate Hamiltonian in the exit channel:

$$(H_\beta + K_\beta + V_\beta)\Psi_\alpha^{(+)} = E\Psi_\alpha^{(+)}. \tag{2.25}$$

By applying Eq. (2.22), we get

$$(E_\beta - K_\beta)\xi_\beta(\vec{r_\beta} = \langle\psi_\beta|V_\beta|\Psi_\alpha^{(+)}\rangle. \tag{2.26}$$

The solution yields

$$T_{\beta\alpha} = \langle e^{i\vec{k_\beta}.\vec{r_\beta}}\psi_\beta|V_\beta|\Psi_\alpha^{(+)}(\vec{k_\alpha})\rangle. \tag{2.27}$$

The total wavefuntion $\Psi_\alpha^{(+)}$ is estimated through the DWBA procedure. In this procedure, the interaction potential V_β is expressed as a sum of two terms:

$$V_\beta = U_\beta(r_\beta) - W_\beta(x_\beta), \tag{2.28}$$

where $U_\beta(r_\beta)$ is the average potential and $W_\beta(x_\beta, \vec{r_\beta})$ is the residual interaction potential, noting that $W_\beta(x_\beta, \vec{r_\beta})$ is comparatively small and it is usually taken

to be a perturbation. $U_\beta(r_\beta)$ is usually treated as a complex optical potential obtained by fitting elastic scattering data [Har01]. With this, Eq. (2.26) becomes

$$(E_\beta - K_\beta - U_\beta(r_\beta))\xi_\beta(\vec{r_\beta}) = \langle\psi_\beta|W_\beta|\Psi_\alpha^{(+)}\rangle \tag{2.29}$$

and the solution may be expressed in terms of the solution of the homogeneous equation

$$(E_\beta - K_\beta - U_\beta(r_\beta))\chi_\beta^{(+)}(\vec{k_\beta}, \vec{r_\beta}) = 0. \tag{2.30}$$

The functions $\chi_\beta^{(+)}(\vec{k_\beta})$ are know as the distorted waves. The waves are distorted as a result of the optical model potential U_β. Asymptotically, the solutions have the form of an incident plane wave plus outgoing spherical waves:

$$\chi_\beta^{(+)}(\vec{k_\beta} = e^{i\vec{k_\beta}.\vec{r_\beta}} + f_\beta^{(0)}(\theta)\frac{1}{r_\beta}e^{ik_\beta r_\beta}, \tag{2.31}$$

where $f_\beta^{(0)}(\theta)$ is the scattering amplitude due to U_β alone and θ is the scattering angle.

2.2.2.1 Energy weighted sum rule (EWSR)

Giant resonances are collective states in which most of the transition strength connected with the response of the nucleus to an external weak field acting on it are concentrated. This field can be decomposed into various multipoles and the response can be considered as the sum of the various contributions of the multipole giant resonances. Energy Weighted Sum Rule (EWSR) can be described as a measure of the strength of the giant resonance. It is defined as a sum of the transition probabilities from ground state to excited states for a given multipolarity, multiplied respectively by the excitation energy [Boh75, Pat15],

$$S(O^{\lambda\mu}) = \sum_n |\langle n|O^{\lambda\mu}|0\rangle|^2(E_n - E_0). \tag{2.32}$$

Here, n represents the complete set of states attainable when a multipole field operator O acts on the initial ground state $|0\rangle$ of a nucleus. Also, λ and μ refer to the multipolarity and isospin structure of the resonance. For the multipole field operator,

$$O^{\lambda\mu} = \sum_{i=1}^{A} f(r_i)Y_L^M(\Omega_i), \tag{2.33}$$

the EWSR can be expressed as [Boh75],

$$S(O^{\lambda\mu}) = \frac{2\lambda+1}{4\pi}\frac{\hbar^2}{2m}A\langle\left(\frac{df}{dr}\right)^2 + \lambda(\lambda+1)\left(\frac{f}{r}\right)^2\rangle, \tag{2.34}$$

where A is the particle number of the system. For the case of ISGMR where $\lambda = 0$ (which is the focus of the present study), Eqs. (2.33) and (2.34), respectively becomes,

$$O^{00} = \sum_{i=1}^{A} r^2 Y_0^0 \tag{2.35}$$

and

$$S(O^{\lambda\mu}) = \frac{2\hbar A}{m}\langle r^2\rangle. \tag{2.36}$$

The moments of the strength function $S(E)$ are usually expressed as [Gar18]

$$m_k \equiv \int E^k S(E) dE. \tag{2.37}$$

Also, the centroid of $S(E)$ is define by

$$E = \frac{m_1}{m_0}, \tag{2.38}$$

where, for the case of ISGMR, m_1 is given as

$$m_1(ISGMR) = \frac{2\hbar^2}{m}A\langle r^2\rangle. \tag{2.39}$$

Experimental strength distributions for various multipoles are usually obtained via the Multipole Decomposition Analysis (MDA), which involves a rebinning of the experimental cross-sections into 1 MeV excitation energy interval. For each energy bin, the experimental angular distributions in the centre-of-mass frame are fitted by means of the least-square method with linear combination of the calculated double-differential cross sections associated with different multipoles [Li10]:

$$\frac{d^2\sigma^{\exp}(\theta_{\text{c.m.}}, E_{\text{x}})}{d\Omega dE} = \sum_{\lambda=0}^{7} a_\lambda(E_{\text{x}})\frac{d^2{\sigma_\lambda}^{\text{DWBA}}(\theta_{\text{c.m.}}, E_{\text{x}})}{d\Omega dE}. \tag{2.40}$$

Here, $a_\lambda(E_{\text{x}})$ is the EWSR fraction for the λ^{th} component and $\frac{d^2{\sigma_\lambda}^{\text{DWBA}}}{d\Omega dE}$ is the cross section corresponding to 100% EWSR for the λ^{th} multipole at

excitation energy E_x, calculated using the Distorted-Wave Born Approximation (DWBA). For the case of the ISGMR, the experimental strength distribution $S_0(E_x)$ at a given excitation energy E_x is given by [Har01]

$$S_0(E_x) = \frac{2\hbar^2 A\langle r^2\rangle}{mE_x} a_0(E_x), \tag{2.41}$$

where
nucleon mass $m = 938.86$ MeV/c^2,
$\hbar = 197.329$ MeV-fm/c,
$a_0(E_x)$ is the fraction $E0$ EWSR per MeV,
E_x is the excitation energy,
A is the mass number and
$\langle r^2\rangle$ is the moment of the ground state density.

2.3 Extraction of characteristics energy scales

A major focus of the present work is the extraction of the characteristic energy scales in order to undertand the decay mechanisms present in the ISGMR for neutron-rich calcium isotopes. Wavelet analysis has been proven to be a viable tool for extracting the energy scales. The basic concept of wavelet analysis is brief discussed in the section below.

2.3.1 Wavelet analysis

The wavelet transform is a tool used to analyse signals or data. It has application in diverse fields of studies such as image processing, geophysics, accelerator physics and meteorology. The wavelet transform is somewhat an extension of the Fourier Transform (FT). The FT is used to process periodic signals [She08]. It decomposes a signal into its constituent frequency components. Using this process the time-dependence of the signal is converted into frequency dependence. Hence, the time information is completely lost. This is major drawback of the Fourier transform. Besides, Fourier transform can only be applied to periodic signals with infinite length. On the other hand, the wavelet transform offers the possibility to perform a local analysis preserving the correlation between the observable (time) and

its transform (frequency). The wavelet transform is based on the concept of wavelet function or so-called *wavelets*. For a function $\Psi(x)$ to be considered as a wavelet, it must fulfill or satisfy the following conditions [Mal98]:

$$\int_{-\infty}^{\infty} \Psi^*(x)dx = 0 \tag{2.42}$$

and

$$K_\Psi = \int_{-\infty}^{\infty} |\Psi^2(x)|dx < \infty, \tag{2.43}$$

where $\Psi^*(x)$ is the complex conjugate of $\Psi(x)$ and K_Ψ is the norm wavelet. The implication of Eq. (2.42) is that the function must be oscillating and the mean value should be zero. Equation (2.43) implies that the function must have finite length. A wavelet can then be described as a small wave localised both in time and frequency domains with zero mean value. Thus, wavelet basis functions describe the local behaviour more efficiently because they are not affected by properties of the data far away from the location of interest [She08]. Some examples of the widely used wavelet functions and their graphical representations are illustrated in Fig. 2.3.

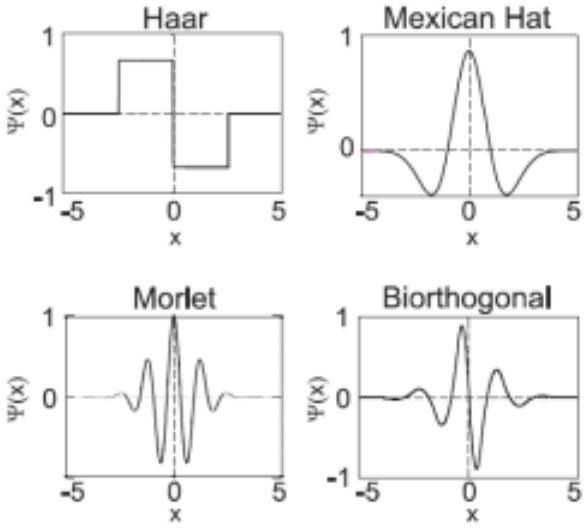


Figure 2.3: Schematic representation of some widely used wavelet functions, taken from [Lat17]

The coefficients (or wavelet transform) of an original energy spectrum $\sigma(E)$ can be obtained by the convolution of the spectrum $\sigma(E)$ with a chosen wavelet

function, and it is expressed as

$$C(E_{\mathrm{x}}, \delta E) = (\delta E)^{1/2} \int \sigma(E) \Psi \left(\frac{E - E_{\mathrm{x}}}{\delta E} \right) dE, \tag{2.44}$$

where δE is the scale parameter (energy bin size in this case) that compresses and stretches the wavelet function, and E_{x} represent the position or translation parameter (excitation energy in this case) that shift the wavelet in the spectrum $\sigma(E)$. The scale δE and translation parameter E_{x} can be varied continuously using the Continuous Wavelet Transform (CWT) or in discrete steps ($\delta E = 2^j$, $E_{\mathrm{x}} = k\delta E$, j, k =1, 2, 3,...) using the Discrete Wavelet Transform (DWT). See [She08] for detailed descriptions of these wavelet transforms. The CWT is used to extract characteristic scales from nuclear spectra. This is achieved by adjusting the fit procedure to the required precision. It is has been established [Mal98] that the inverse wavelet tansform can be used to reconstruct the original spectrum $\sigma(E)$ from the wavelet coefficients

$$\sigma(E) = K_{\Psi}^{-1} \int_{-\infty}^{\infty} C(E_{\mathrm{x}},) \frac{1}{(\delta E)^{5/2}} \Psi \left(\frac{E - E_{\mathrm{x}}}{\delta E} \right) d(\delta E) dE_{\mathrm{x}}. \tag{2.45}$$

The reconstruction is exact only if the wavelet functions are orthogonal

$$\int_{-\infty}^{\infty} \Psi_{i,j}(E) \Psi^*_{k,m}(E) dE = \delta_{ik} \delta_{jm}. \tag{2.46}$$

This condition can only be fulfilled by the DWT. The reconstruction procedure involves the use of the DWT varying the scale and the position by powers of two. This results in an iterative decomposition of the original spectrum into approximation (A_i) and the detail (D_i) components. Here, (A_i) and (D_i) correspond to the large-scale and the small-scale components of the original spectrum, respectively. This process is schematically illustrated in Fig. 2.4. In each step i of the decomposition, the original spectrum can be reconstructed as

$$\sigma(E) = A_i + \sum D_i \tag{2.47}$$

Wavelet functions have another useful feature that can be applied for determination of background in the experimental data. Each wavelet function can be characterized by the number of its vanishing moments [Mal98]

$$\int_{-\infty}^{\infty} E^n \Psi(E) dE = 0 \quad \text{with n = 0,1,2,...m.} \tag{2.48}$$

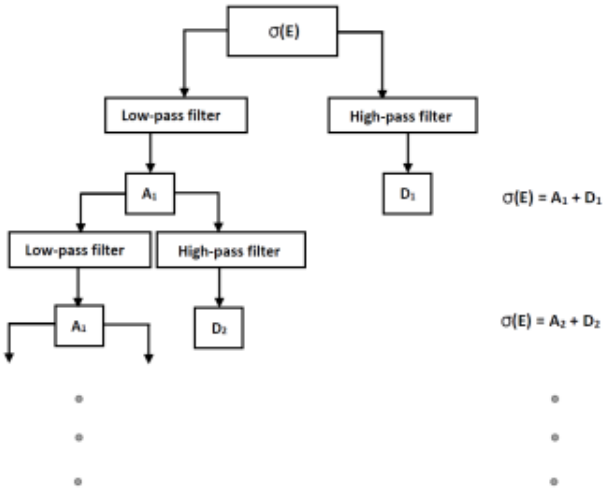


Figure 2.4: Schematic illustration of how the original spectrum is decomposed into approximation and details components using the DWT, taken from [Lat17]

For instance, the Biorthogonal (Bior3.9) wavelet function has $m = 2$. This implies that any background in the spectrum that can be approximated by a polynomial of order 2, does not contribute to the wavelet coefficients. This allows for the extraction of level densities. See [She08] for detailed information on the application of this technique to nuclear giant resonance spectra.

2.4 Extraction of level densities

The Nuclear Level Density (NLD) can be defined as the number of levels in 1 MeV at a certain excitation energy. It varies smoothly with the excitation energy and the number of nucleons in a nucleus. It is an important quantity required in nuclear models used to calculate reaction cross-sections needed for many practical applications. Consider, for example, that the study of NLD is of importance in the medical field. A number of radioactive nuclei are used in medicine for the treatment of cancers, radiotherapy, positron emmission tomography (PET) imaging [Men04]. The production cross-sections of these radio-nuclides can be optimized by using nuclear model codes that require level densities as input parameters. Also, in astrophysics, the reaction rates of production of some nuclei are predicted using nuclear models that have level densities as input parameters (see [Rau97] and the references therein). The

method of extracting experimental level densities using a model-independent approach together with fluctuation analysis is presented in this section.

2.4.1 Theoretical models for level density extraction

There are a number of approaches employed to calculate level densities. Phenomenological approaches are used to extract the level densities by fitting the experimental data at low excitation energies while sophisticated microscopic models are applied to predict the level densities by using Hartree-Fock based calculations up to high excitation energies. A brief description of some of the models is presented in this subsection.

2.4.1.1 Phenomenological models

One of the practical ways of extracting the nuclear level densities, especially at low excitation energies is through the use of simple models such as the Back-shifted Fermi Gas (BSFG) model [Gad68, Hui69] and the Constant-temperature (CT) model [Eri60]. The BSFG was obtained by modifying the original Fermi GAS model expression [Bet37] to include the shell and pairing effects. In the BSFG model, the nulcear level density $\rho(E, J)$ is expressed as a product of two functions

$$\rho(E, J) = \rho(E) f(J), \tag{2.49}$$

where $f(J)$ is a function for the spin distribution

$$f(J) = \frac{2J+1}{a\sigma^2} exp\left(-\frac{J(J+1/2)}{2\sigma^2}\right) \tag{2.50}$$

and the total level density $\rho(E)$ is given as

$$\rho(E) = \frac{1}{12a^{1/4}} \frac{\exp\left(2\sqrt{a(E_{\mathrm{x}}-\delta)}\right)}{\sqrt{2}\sigma(E_{\mathrm{x}}-\delta)^{5/4}}. \tag{2.51}$$

The spin cut-off parameter $\sigma = 0.0888A^{2/3}\sqrt{a(E_{\mathrm{x}}-\delta)}$, A is the number of nucleons, a is the density of the single-particle states near the Fermi level, and δ denotes the energy-shift. Here, a is taken as a free parameter and it is determined from a fit to data.

This model has been applied to a variety of nuclei to obtain the nuclear level density up to 20 MeV excitation energy, and the results are quite satisfactory [Dil73].

Another simple model for obtaining the NLD at low excitation energy is the Constant-temperature (CT) model. The CT model is based on the assumption that at constant temperature, all the energy is used up in the creation of more particle excitation in order to keep the excitation energy per excited particle constant. In the CT model, the NLD is expressed as [Eri60]

$$\rho(E_{\mathrm{x}}) = \frac{1}{T} \exp^{\frac{E_{\mathrm{X}} - E_0}{T}}, \tag{2.52}$$

where T is the nuclear temperature, E_{x} is excitation energy and E_0 is the back-shifted energy. This simple formula was shown [Egi88] to satisfactorily describe the NLD at excitation energies up to the neutron separation energy. Also, it was noted that the CT and BSFG models are similar in many cases at excitation energies below the particle separation energy [Egi88, Voi09].

2.4.1.2 Microscopic statistical models

The NLD are well known at low excitation energies, however, at higher excitation energies, determination of NLD is somewhat challenging. Hence, microscopic calculations are performed to predict the behaviour of the level densities at high excitation energies. Microscopic statistical calculations are performed using the deformed Hartree-Fock-Bardeen-Cooper-Schriffer (HFBCS) [Dem01] predictions of the ground-state structure properties. Also, these calculations include a consistent treatment of the shell effects, pairing correlations, deformation and collective excitation [Dem01]. The Combinatorial model is also another model used to obtain the level densities within the microscopic approach. This model has been shown to provide high predictive power and to satisfactorily reproduce experimental data [Hil01].

2.4.2 Fluctuation analysis

Fluctuation analysis is one of the viable methods used to extract level densities from spectra with high resolution. It was first applied in 1976 by Jonson

et al. [Jon76] to analyse spectra from β–delayed particle emission. Later in 1983, it was adopted for the analysis of high-resolution giant resonance spectra from electron scattering [Mul83]. Recently, it has been applied to extract level densities from giant resonance spectra from proton inelastic scattering on calcium isotopes with $J^{\pi} = 2^{+}$ and 1^{-}, respectively [Usm11, Lat19]. In this present study, the aim is to adopt the autocorrelation function in order to obtain a measure of the cross-section fluctuation with respect to a stationary mean value. This is with the view to obtaning information on the level densities in the ISGMR region of the excitation energy - a region above the particle thresholds.

In an energy region where the experimental energy resolution ΔE is greater than the mean level spacing, two possible cases have to be distinguished. The first is a case where the mean level width $\langle\Gamma\rangle$ is smaller than the mean level spacing$\langle D\rangle$, that is, $\frac{\langle\Gamma\rangle}{\langle D\rangle} \ll 1$, and fluctuations occur as a result of high density on non-resolved states and their incoherent overlap. The second is the so-called Ericson fluctuations [Eri60], where $\frac{\langle\Gamma\rangle}{\langle D\rangle} \gg 1$, which result from the coherent overlapping of the states. The discussion in this thesis is limited to the first region $\frac{\langle\Gamma\rangle}{\langle D\rangle} \ll 1$.

There are two main underlying assumptions upon which the fluctuation analysis formalism is built. One, in a highly-excited nucleus, the probability for a given spacing between states with the same spin and parity obeys the Wigner distribution [Wig65] and it is defined as

$$P_W(s) = \frac{\pi s}{2} exp(-\frac{\pi s^2}{4}), \tag{2.53}$$

where

$$s = \frac{D}{\langle D\rangle}. \tag{2.54}$$

This distribution has a maximum close to the mean value and shows a suppression of small distances between neighbouring levels. Secondly, the transition strengths obey the Porter-Thomas distribution [Por56]

$$P_{PT}(s) = \frac{1}{\sqrt{2\pi s}} exp(-\frac{s}{2}), \tag{2.55}$$

where

$$s = \frac{\Gamma}{\langle\Gamma\rangle}. \tag{2.56}$$

The two assumptions have been experimentally verified to successfully describe nuclear excitations near the particle separation energy [Haq82].

2.4.2.1 Procedure of fluctuation analysis for (α, α') spectrum

The basic steps taken in the application of fluctuation analysis to (α, α') scattering data are presented here. The steps are as follows.

1. Subtract from the experimental (α, α') spectrum any backgrounds not arising from excitations of the nuclear mode under investigation.

2. The background-subtracted spectrum is smoothed and folded with a Gaussian function with a width σ chosen to be smaller than the experimental energy-resolution ΔE. This is necessary in order to remove fluctuation arising from counting statistics. The resulting spectrum is called $g(E_{\mathrm{x}})$ hereafter.

3. Similarly, the background-subtracted spectrum obtained in step 1 above is folded with a Gaussian function with a width $\sigma_{>}$ chosen to be greater than ΔE. The reason for this step is to remove any gross structure in the spectrum. This second spectrum is referred to as $g_{>}(E_{\mathrm{x}})$ hereafter. This spectrum defines the mean about which the original points fluctuate.

4. The ratio of $g(E_{\mathrm{x}})$ and $g_{>}(E_{\mathrm{x}})$ is calculated and the resulting dimensionless spectrum is called the stationary spectrum, and it is defined as

$$\langle d(E_{\mathrm{x}})\rangle = \langle \frac{g(E_{\mathrm{x}})}{g_{>}(E_{\mathrm{x}}}\rangle. \tag{2.57}$$

The value of $d(E_{\mathrm{x}})$ fluctuate around an average intensity $\langle d(E_{\mathrm{x}})\rangle = 1$. Furthermore, the stationary spectrum can be expressed in terms of the autocorrelation function

$$C(\epsilon) = \frac{\langle d(E_{\mathrm{x}}).d(E_{\mathrm{x}}+\epsilon)\rangle}{\langle d(E_{\mathrm{x}})\rangle.\langle d(E_{\mathrm{x}}+\epsilon)\rangle} \tag{2.58}$$

The value $C(\epsilon = 0) - 1$ is the variance since

$$C(\epsilon = 0) - 1 = \frac{\langle d^2(E_{\mathrm{x}})\rangle - \langle d(E_{\mathrm{x}})\rangle^2}{\langle d(E_{\mathrm{x}})\rangle^2}. \tag{2.59}$$

As stated by Jonson *et al.* [Jon76], this experimental autocorrelated function can be approximated by the expression

$$C(\epsilon) - 1 = \frac{\alpha\langle D\rangle}{2\sigma\sqrt{\pi}} \times f(\epsilon, \Delta E), \tag{2.60}$$

where

$$f(\epsilon, \Delta E) = \left\{ exp\left(-\frac{\epsilon^2}{4\Delta E^2}\right) + \frac{1}{y} exp\left(-\frac{\epsilon^2}{4\Delta E^2 y^2}\right) - \sqrt{\frac{8}{1+y^2}} exp\left(-\frac{\epsilon^2}{4\Delta E^2(1+y^2)}\right)\right\}, \tag{2.61}$$

and

$$y = \frac{\sigma_>}{\sigma}. \tag{2.62}$$

The function $f(\epsilon, \Delta E)$ depends on properties of the experimental spectrum only and is normalised such that $f(\epsilon = 0) = 1$. It has been shown that by setting $\sigma = \frac{1}{2}$ and $y = 2.5 - 3.5$ the most stable results can be obtained. For a spectrum consisting of states with the same spin and parity J^π (where $J^\pi = 0^+$ in the present study), the quantity α is the sum of the normalized variances of the spacing and transition width distributions assumed to be of Wigner and Porter-Thomas type, respectively,

$$\alpha = \alpha_W + \alpha_{PT} = 0.273 + 2.0. \tag{2.63}$$

The mean level spacing $\langle D\rangle$ can be extracted from the value $C(\epsilon = 0) - 1$ and the corresponding nuclear level density $\rho(E)$ can be obtained from

$$\rho(E) = \frac{1}{\langle D\rangle}. \tag{2.64}$$

Chapter 3

Experimental procedure and data extraction

The main purpose of this experimental study is to better understand the phenomenon of fine structure in the region of the Isoscalar Giant Monopole Resonance (ISGMR) as it relates to neutron excess in selected calcium isotopes (^{40,42,44,48}Ca). The experiment, which was assigned project number PR260 by the iThemba LABS Program Advisory Committee (PAC) [Usm16], involves high energy-resolution measurements of the ISGMR in the neutron-rich isotopes of calcium (^{42,44,48}Ca). Data for the nucleus ^{40}Ca from project number PR236 was also included in this study. The measurements were performed using the K600 magnetic spectrometer together with a 200 MeV dispersion-matched α-particle beam, which was delivered by the Separated Sector Cyclotron (SSC) of iThemba Laboratory for Accelerator Based Sciences (iThemba LABS), situated near Somerset West in Cape Town.

This chapter gives a detailed description of the experimental facility, experimental techniques, data acquisition and the procedures for data extraction and analysis.

3.1 iThemba LABS Separated Sector Cyclotron

Activities at iThemba LABS are based around a number of sub-atomic particle accelerators. The largest of these is the K200 SSC. The SSC produces fast moving charged particle beams which are used for various purposes such as nuclear physics research, radioisotope production and radiation biophysics research. For nuclear physics research, the SSC is used together with other experimental facilities such as the K600 magnetic spectrometer, the gamma detector array AFRODITE and the A-line nuclear reaction scattering chamber.

A schematic view of the SSC and the beamlines is shown in Fig. 3.1. There are two injector cyclotrons which are used to produce and pre-accelerate beam. The first is the $K = 8$ Solid Pole Cyclotron 1 (SPC1), which has an internal Penning Ionisation Gauge (PIG) ion source. The second is the $K = 8$ Solid Pole Cyclotron 2 (SPC2), which has two external ion sources: a polarised ion source and the Electron Cyclotron Resonance (ECR) ion source. The ECR ion source was used for this particular experiment.

A $^{4}He^{++}$ beam from the ECR ion source is injected into SPC2, accelerated to a certain suitable energy and then delivered through the K and J beamlines to the SSC where it is further accelerated to the desired energy of 200 MeV. Then the 200 MeV alpha particle beam is transported to the K600 magnetic spectrometer vault through a high-resolution double monochromator system consisting of the X, P, P2 and S beamlines as shown in Fig. 3.1. This system is equipped with sets of quadrupole magnets, dipole magnets and slits for optimisation.

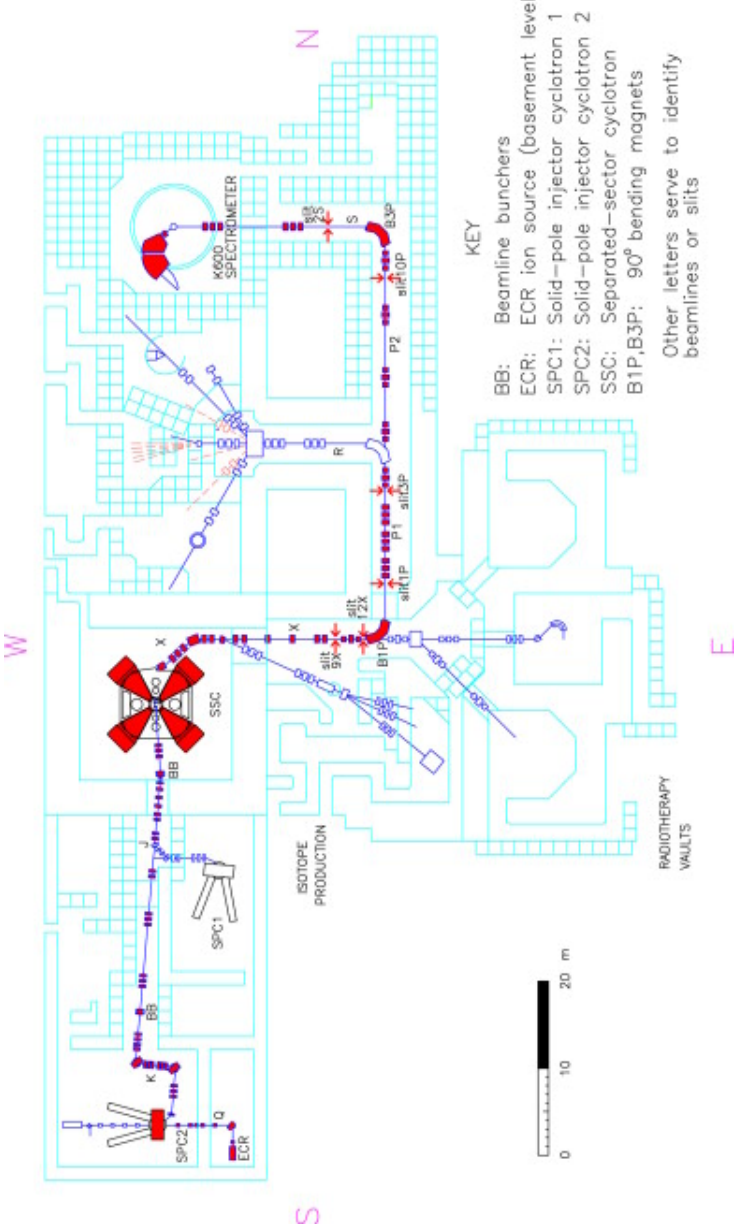


Figure 3.1: The layout of the cyclotron facility at iThemba LABS [Nev11].

3.2 iThemba LABS K600 magnetic spectrometer

The iThemba LABS K600 magnetic spectrometer is composed of five active elements, namely, a quadrupole magnet, two dipole magnets (D1 and D2) and two trim coils (K and H). The layout of these elements is shown in Fig. 3.2. The quadrupole is used to achieve vertical focusing. The two dipole magnets allow the momentum dispersion to be varied by varying the ratio of the two dipole magnets [Nev11]. The K and H trim coils are located inside the D2 and D1 magnets respectively. The K-coil is used for first-order corrections by adding a dipole and quadrupole field component inside D2. The H-coil provides second-order correction within D1 through a dipole and hexapole component. These corrections are necessary in order to mitigate the dependency of the focal plane position on the scattering angle of the scattered particles originating from a particular nuclear state.

Inside the scattering chamber of the spectrometer is a target ladder with six target positions and a turntable on which an internal beamstop can be mounted. The focal plane position-sensitive detector package is located behind the second dipole magnet. A detailed description of the focal plane detectors is presented in Section 3.2.1.

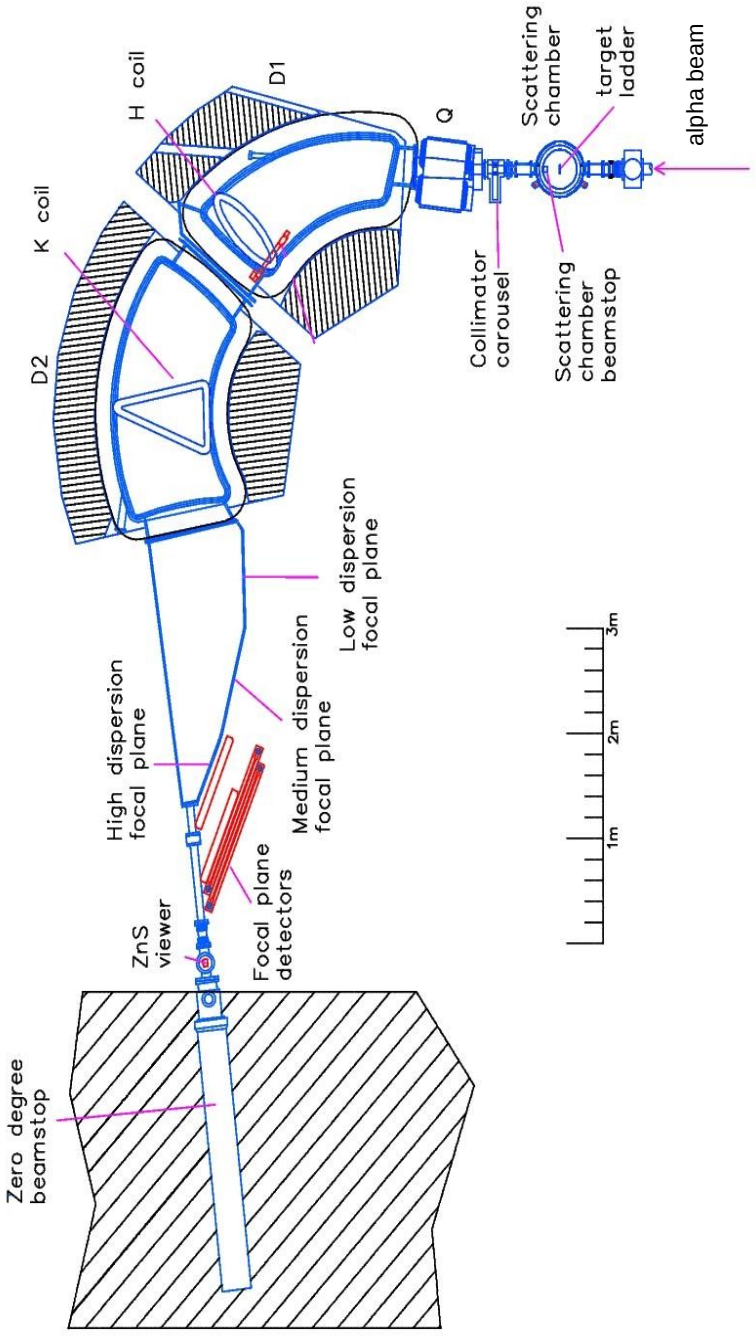


Figure 3.2: The layout of the K600 facility in the zero degree mode with the focal plane detectors positioned in the high-dispersion focal plane.

3.2.1 Focal plane detector suite

The focal plane detector package consist of two Vertical Drift Chambers (VDCs) and a pair of plastic scintillation detectors, colloquially referred to as "paddles" because of their geometry. Figure 3.3 shows the schematic top view of the focal plane with the inelastically scattered α-particles traversing the detectors at an average angle of 32.2°.

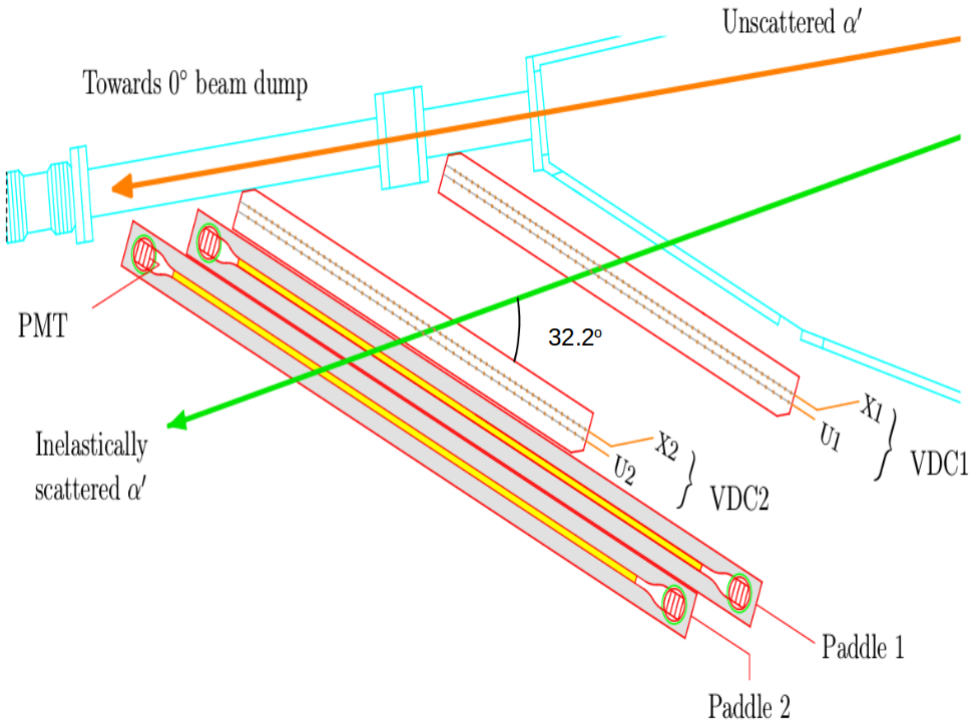


Figure 3.3: A schematic view of the focal plane detectors.

3.2.1.1 Vertical drift chambers

The VDCs are used to obtain the position and angle information of the scattered particles traversing the focal plane. The technical specifications of these detectors are presented in Table 3.1. Each VDC has an X wire plane which provide horizontal information of the scattered particle, and a U wire plane which provides a linear combination of horizontal and vertical information. The X-wires and the U-wires are at 90° and 50° to the scattering plane respectively [Nev11].

Table 3.1: Technical specifications of the vertical drift chamber [Nev17].

VDC Components	Specifications
XU wire configuration	vertical (X) and 50° (U)
Horizontal VDC acceptance	78 cm
Vertical VDC acceptance	10 cm
Signal wire	20μm gold plated tungsten
Guard wire	50μm gold plated tungsten
Cathode plane	20μm Al foil
Number of signal wires	198 (X) and 143 (U)
Number of guard wires	201 (X) and 146 (U)
Cathode-anode spacing	8 mm
Signal wire spacing	4 mm
Guard wire spacing	4 mm
Gas mixture	90% Ar 10% CO_2
Entrance and exit windows	25μm mylar
Pre-amplifier	Technoland (13 units (X) and 9 units (U))
Typical guard wire voltage for 200 MeV α-particles	$\sim$ -500 V
Typical cathode plane voltage for 200 MeV α-particles	$\sim$ -2950 V

The interior of each of the VDCs is isolated from the atmosphere by entrance and exit windows made of 25 μm thick mylar. The space in-between these mylar windows is filled with a gas mixture of Ar and CO_2 in a mass ratio of 90% and 10%, respectively. When the drift chambers are in operation and scattered charged particles pass through them, the molecules of the gas mixture are ionised and free electrons are created. These free electrons drift towards the signal wires (anodes) and hence generate electrical signals. The signals are pre-amplified and discriminated and then sent to time-to-digital converters (TDCs) in the data acquisition (DAQ) system through 16-channels twisted-pair ribbon cables. These TDCs are capable of 100 ps time resolution [Nev11]. A schematic view of the K600 trigger electronics is shown in Fig. 3.4. The position accuracy of the VDCs is known to be $\sim$ 80.9 μm [Nev17]. This parameter also determines the angle accuracy that can be obtained with the VDCs.

3.2.1.2 Plastic scintillators

The plastic scintillators are used to create a fast timing trigger and for particle identification purposes. Summarised in Table 3.2 is the technical specifications of the plastic scintillators [Nev17]. For this experiment only the first scintillator was used to create the trigger signal.

Table 3.2: Technical specifications of a plastic scintillator [Nev17].

Scintillator Components	Specifications
Scintillating material	Bicron BC-408
Scintillating dimensions	$48 \times 4 \times 0.5$ inch^3
Lightguide	Saint Gobain Crystals 90° adiabatic twisted pair
Photomultiplier Tube (PMT)	Hamamatsu R329-02 PMT tube with a Hamamatsu E934 base
Typical PMT voltage for 200 MeV α-particles	$\sim$ -1100 V
Maximum PMT voltage	-2700 V

When scattered particles pass through the scintillators interactions occur which cause it to scintillate. The emitted light is collected by the photomultiplier tubes, one at each end of the two scintillators, and electric signals are generated. These signals are sent to the charge-to-digital converter (QDC) which integrate them and provide digital output to the DAQ (see Fig. 3.4). The triggered time of the scintillator with respect to the Radio Frequency (RF) of the cyclotron is used as a relative measure of the Time-Of-Flight (TOF) of the scattered particles in the K600. This TOF, together with the energy lost in the detector by the particles can be used to distinguish between the various types of particles detected by the focal plane detectors. The trigger logic diagram in Fig. 3.4 illustrates how the signals from the four PMTs are manipulated to create a QDC gate signal which is used to define an event in the DAQ.

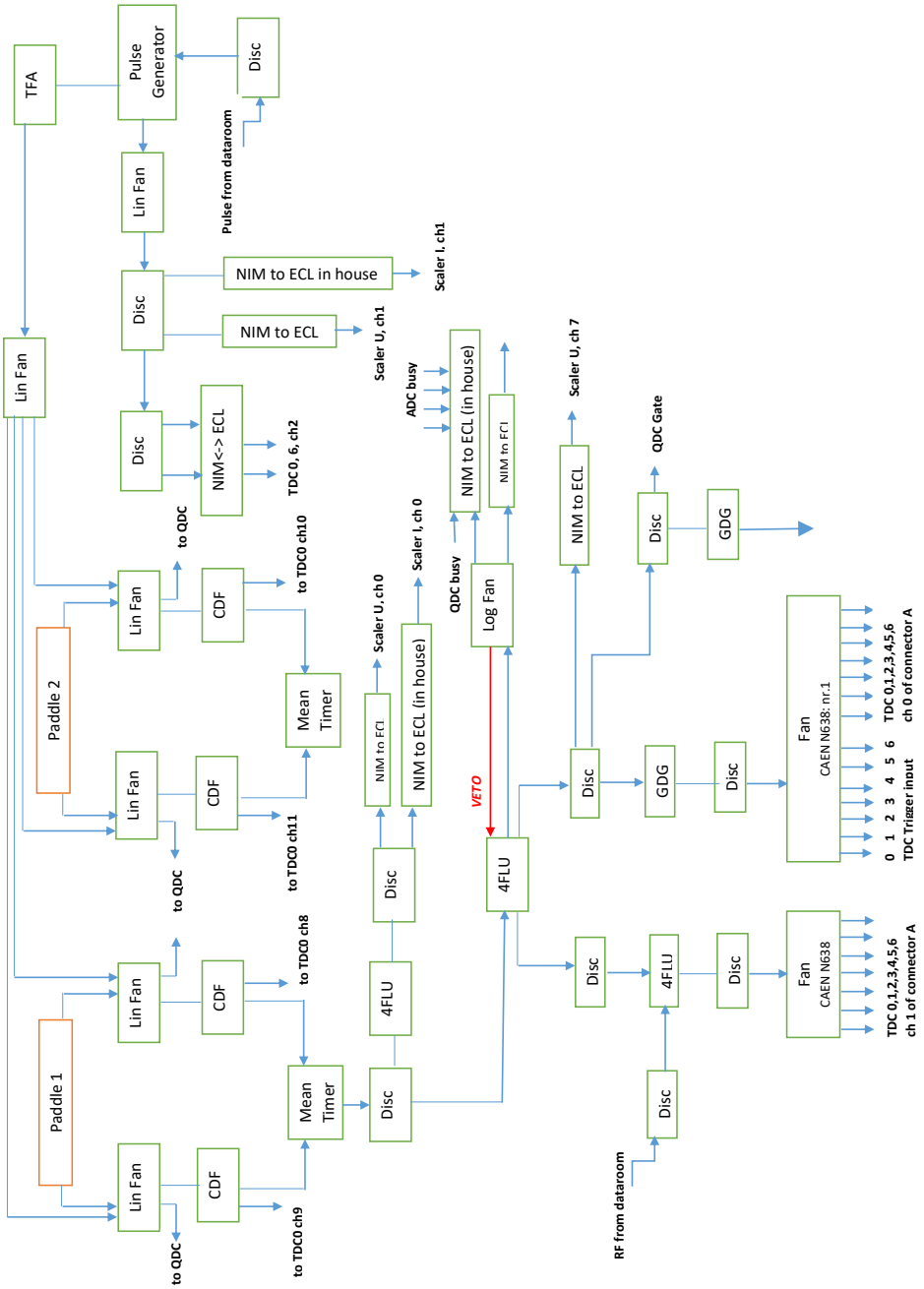


Figure 3.4: A layout of the K600 trigger electronics. Note that only signals from paddle 1 are used to create the QDC gate or trigger signal.

3.2.2 Dispersion matching techniques

Dispersion matching techniques involve the process of matching or aligning the beamline with the spectrometer in order to obtain a better (spatial and angular) spectral resolution at the spectrometer focal plane than the incident beam resolution. With this, the full high-resolution capability of the spectrometer can be exploited. This concept was first illustrated by Cohen *et al.* in 1959 [Coh59] and later demonstrated in 1971 by Blosser *et al.* [Blo71]. Ever since then the technique has been widely adopted and implemented in many places [Ike80, Mar83, Ber93, Wak02] including iThemba LABS [Nev11].

First achromatic focus at the target is achieved so that the position and incident angle of the incident particle on the target are independent of its momentum, that is

$$(x|\delta p/p) = 0 \tag{3.1}$$

and

$$(\theta|\delta p/p) = 0. \tag{3.2}$$

The beamspot is thus optimised to be as small as possible and this is achieved by adjusting the horizontal and vertical slits at 9X in the X-line (see Fig. 3.1). The typical spot size is 2 mm wide and 1 mm high. The maximum designed acceptance of the K600 is ± 2.14 degree in the vertical and horizontal. Beyond these angles the particles will hit the side of the vacuum chamber (vertically the dipole, horizontally the quadrupole). In this study, the experiments were performed with acceptance of (at maximum) ± 2 degree. This was chosen for safety reasons. The beamspot is small enough so that it does not appreciably affect the K600 acceptance. After this procedure, the K and H coils can be tuned in order to get the appropriate kinematic correction for the particular target in use. Then the magnets from 9X downstream are changed to the dispersion matched settings. The last two quadrupole magnets in the S-line, Q5S and Q6S, are involved in the final fine tuning to ensure the beam is dispersion matched to the K600 spectrometer.

There are two main dispersion matching conditions, namely, lateral and angular dispersion matching [Fuj97, Fuj02]. The former is achieved by adjusting the beamline magnets so that the particles with higher momenta have to travel a longer distance to the focal plane than the particles with

lower momenta. The angular dispersion allows for accurate determination of the scattering angles of particles. This particular experiment was carried out in focus mode, hence, the angular dispersion matching was not used.

3.2.2.1 Faint beam method

Faint beam simply refers to a beam of very low intensity of approximately 10^3 particles per second, as opposed to a beam current of 1 nA ($\approx 10^9$ particles per second). This beam of low intensity is used to achieve dispersion matching for zero degree experiments by changing the K600 fields to directly observe the beam. At iThemba LABS, the faint beam is achieved by inserting three beam-attenuation meshes in between the ECR ion source and SPC2. These meshes reduce the number of alpha particles in the beam by a factor of up to 10^6 without changing the beam profile [Nev11]. The three meshes are made of thin copper plates with very tiny holes and can reduce the beam going to SPC2 by a factor of 10, 100 and 1000, respectively. The one that attenuates the beam by a factor of 100 is listed as APP1 on the iThemba LABS accelerator control while the second mesh, which combines the factor 10 and 1000 meshes to attenuate the beam by a factor of 10000, is listed as APP2.

3.3 Target preparation and handling

A summary of all the relevant targets used in experiments PR260 and PR236 is presented in Table 3.3. The targets were prepared in the iThemba LABS target laboratory. The calcium targets were used in the PhD project of M. Latif, and a detailed description of how the targets are prepared is reported in his thesis (see [Lat17] and the references therein). Hence, only a brief summary of the target preparation is reported here.

The material used for manufacturing the ^{40}Ca, ^{42}Ca, ^{44}Ca and ^{48}Ca targets were supplied as metal lumps by Oakridge National Laboratory. These metal lumps were rolled to a desired thickness. The calcium targets are very sensitive and undergo oxidation quickly, hence special measures were taken to prevent any exposure to air. The whole process was, therefore, carried out inside a

glove box under an inert argon environment using stainless steel plates as carriers for rolling.

Table 3.3: Areal thickness and corresponding isotopic enrichment of targets used [Lat17].

Target	Areal thickness (mg/cm^2)	Isotopic enrichment (%)
^{24}Mg	2.100± 0.2	99.9
^{40}Ca	1.000± 0.1	96.94
^{42}Ca	1.315± 0.1	98.68
^{44}Ca	1.435± 0.1	93.71
^{48}Ca	1.090± 0.1	90.04

Transport of the targets between the target laboratory and the scattering chamber was achieved using a special target-ladder-transfer chamber (see Fig. 3.5) which was constructed at iThemba LABS. The target ladder with the mounted targets was kept in the transfer chamber under vacuum before and after the experiment. During the experiment, the transfer chamber is mounted on top of the scattering chamber (see Fig. 3.5c) and the target ladder is carefully transfered into the scattering chamber. This process is colloquially called a "fishing exercise", as it is not always possible to see if the target ladder goes smoothly into the target ladder fork.

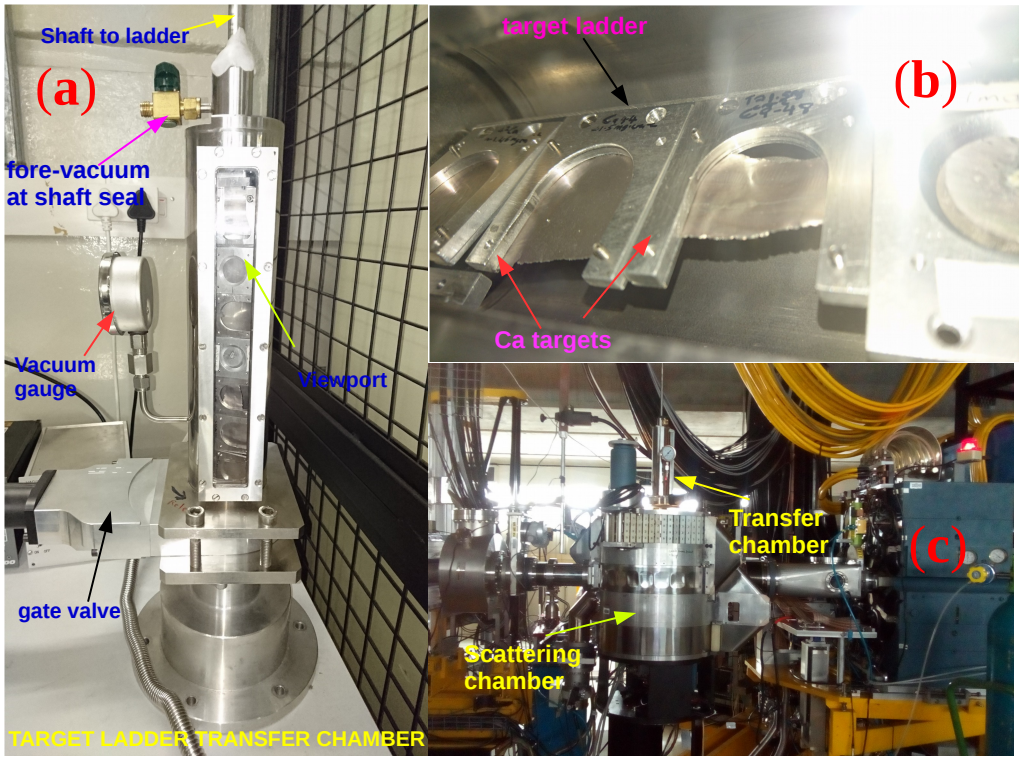


Figure 3.5: (a) Target-ladder-transfer chamber. (b) Ca targets mounted on the target-ladder inside the transfer chamber. (c) The transfer chamber mounted on the spectrometer scattering chamber.

3.4 Experimental procedure

The ^{24}Mg, ^{42}Ca, ^{44}Ca and ^{48}Ca targets were bombarded with a 200 MeV beam of alpha particles with the K600 positioned at zero degrees for a weekend in February 2017. This scattering angle was selected to match the peak of the cross sections for $\Delta L = 0$ excitations in the corresponding targets, and thereby exciting predominantly the Isoscalar Giant Monopole Resonance (ISGMR) which is the main focus of this study. In order to estimate the contribution of other multipoles to the cross sections, especially the Isoscalar Giant Quadrupole Resonance (ISGQR), additional measurements were taken at 4° in June 2017.

In a zero degree experiment, both the beam and the scattered particles travel through the spectrometer. The beam goes into the beam-dump while the scattered α-particles are directed to the focal plane detectors, positioned at the high-dispersion focal plane. The plastic scintillator detectors provide a trigger

signal to the DAQ indicating data is to be acquired (see Section 3.2.1.2). Data was typically taken for 20 minutes with a ^{24}Mg calibration target and one hour for each of the calcium targets. This was typically followed by empty target frame run for 10 minutes to check the beam halo condition. This routine was maintained until sufficient data were acquired for all the targets of interest.

During the zero degree measurements, the beam profile was good and the entire data acquisition system was functioning at its optimum such that by the end of the first weekend sufficient statistics were already collected for all the targets of interest. This February 2017 beam period ran from Thursday afternoon to Monday morning. On Sunday afternoon it was clear that sufficient data were already collected for the calcium isotope targets, which allowed for data acquisition till the Monday for mylar and ^{12}C targets. The reason for these measurements was to have data available to investigate oxygen contamination in the calcium targets. Calcium isotope targets are known to be highly sensitive and reactive in air, and oxygen contamination was envisaged despite the precautionary measures that were put in place.

3.5 Data extraction and offline analysis: zero degrees measurements

One of the main quantities to be obtained from this measurement is the cross section as a function of excitation energy, and for this to be achieved the measured raw data must be sorted and analysed offline. The first step to be taken in the analysis is to identify the scattered alpha particles using the ΔE information of the first paddle in the focal plane and a TOF measurement. The next step is to obtain the position and angle information of the alpha particles traversing the focal plane using the Vertical Drift Chambers (VDCs). Finally, the energy calibration is done and the cross sections are determined.

3.5.1 Particle identification

In an experimental measurement where a beam of 200 MeV α-particles interact with a target, many other particles from other reaction channels are also opened. These other particles may be observed by the focal plane detectors and hence contribute to the experimental yield. It is, therefore, necessary to carry out a particle identification (PID) process in order to focus on the particles of interest. The PID regions of interest are defined by the measured energy loss in the plastic scintillators together with the TOF of the scattered particles.

The magnetic field of the spectrometer enables separation of charged particles on the basis of their rigidity. The rigidity is defined as,

$$R = B\rho = \frac{p}{Q}, \tag{3.3}$$

where ρ is the gyroradius of the charged particle's circular motion in a constant magnetic field B, and p and Q are the momentum and charge of the charged particle, respectively.

For zero degree measurements the K600 fields are set to allow clean transportation of the beam to the 0° beamstop. This field and the position of the focal plane detectors then define the rigidities that can be accessed in the focal plane detectors and hence the excitation energy range that can be studied. The excitation energy range studied in this experiment is from $\sim$ 6 MeV to 26 MeV, as will be shown later in Section 3.5.5.1.

Figure 3.6 is a plot of energy deposited in Paddle 1 against the TOF for the ^{48}Ca target, showing various PID loci. Clearly identified on the plot are loci representing the scattered alpha particles, protons and halo. The source of the background below the α-particle locus is unknown. These particles have a similar TOF to the α-particles. From rigidity calculations it follows that these may be low energy deuterons ($\sim$ 86 – 91 MeV) which has a similar TOF to the $\sim$ 174 – 194 MeV α particles. Also, from this plot it is clear that the protons and the halo are not as abundant as the alpha particles, which is represented by the strongest locus. The energy structure of each locus is examined by making a paddle1-versus-TOF PID plot together with

the corresponding position spectrum as shown in Figs. 3.7 to 3.9. In Fig. 3.7 the protons region is selected. The ^{48}Ca(α,p) reaction has a Q–value of -5.860 MeV, and the proton energies covered for the rigidity equivalent of α's between 6 and 26 MeV excitation energy equals proton energies from 162.7 – 180.3 MeV. It is clear from the bottom panel that the position spectrum for the proton is not well defined when compared with the alpha particles spectrum. While it is unclear how strong this (α,p) reaction will be, the rigidity range accessible to protons puts us above the any known excited states for the residual nucleus. The TOF difference between α's and p and the difference in ΔE strongly indicates these selected events to be protons even though the structure of the residual nucleus could not be verified. The target related halo gives a position spectrum that increases towards the low excitation energy region as shown in bottom panel of Fig. 3.8. The beam halo to be found inside the α-particles gate represents scattered α-particles from sources other than the target, and can be identified in the paddle 1 versus TOF plot for the empty target, shown in Fig. 3.10.

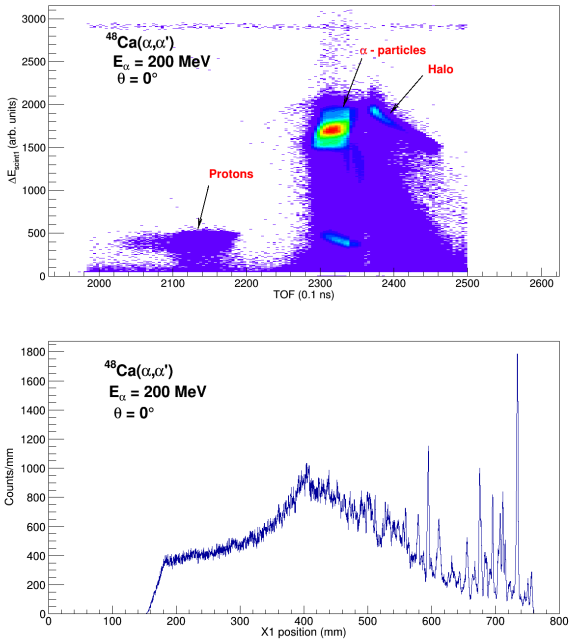


Figure 3.6: Top: A plot of energy deposited in paddle 1 versus TOF for α particles incident on ^{48}Ca target showing various PID loci. Bottom: Position spectrum obtained from the α PID gate.

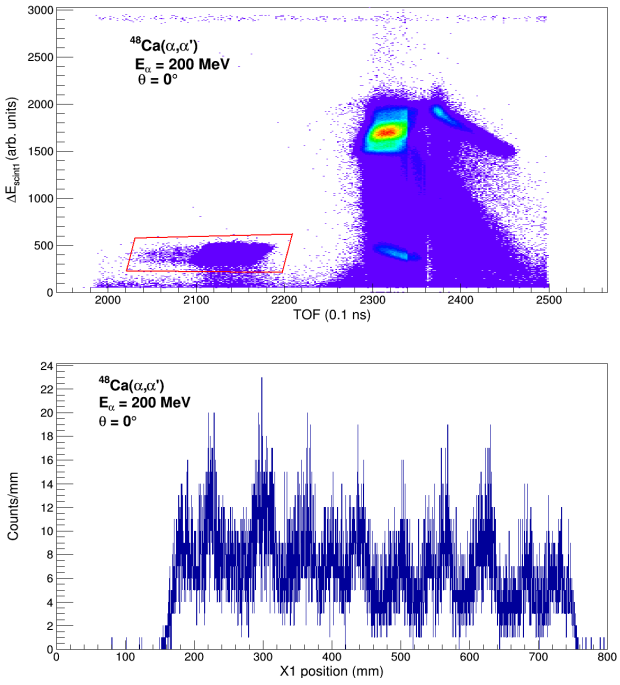


Figure 3.7: Top: Paddle1-versus-TOF PID plot for α particles incident on ^{48}Ca target showing the proton PID gate. Bottom: Position spectrum obtained from the proton PID gate.

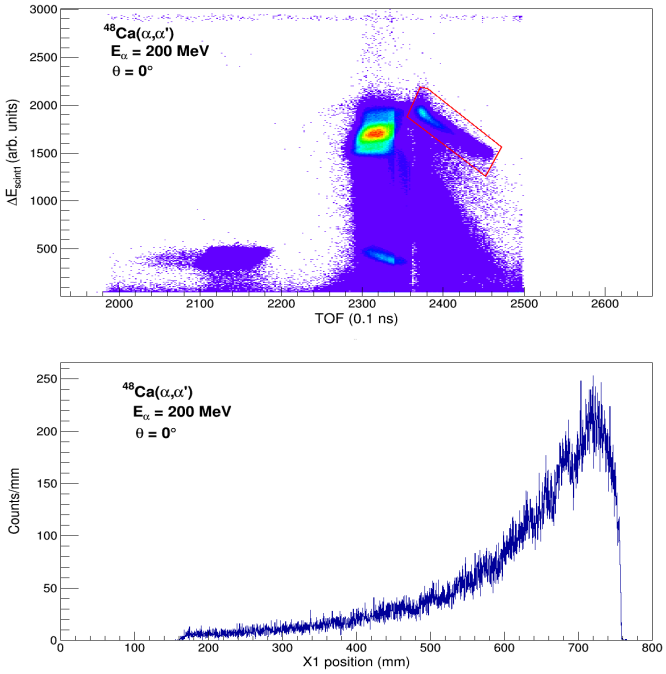


Figure 3.8: Top: Paddle1-versus-TOF PID plot for α particles incident on ^{48}Ca target showing the beam halo PID gate. Bottom: Position spectrum obtained from the beam halo PID gate.

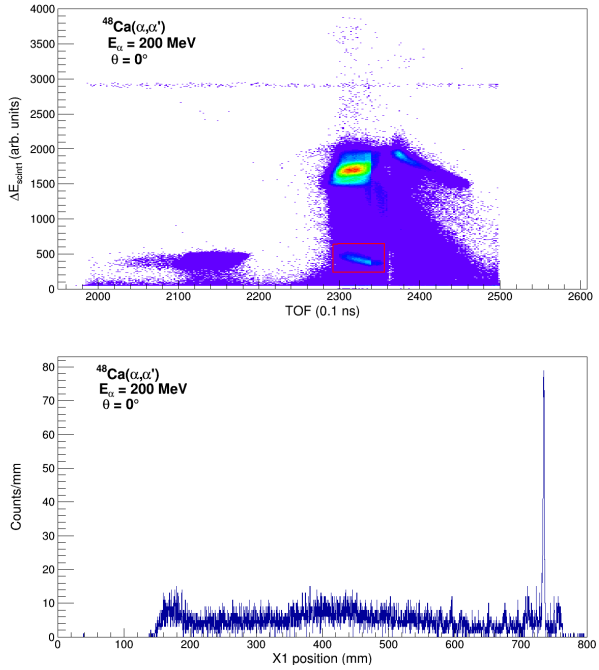


Figure 3.9: Top: Paddle1-versus-TOF PID plot for α particles incident on a ^{48}Ca target showing the background below the alpha PID gate. Bottom: Position spectrum obtained from the background below the alpha PID gate.

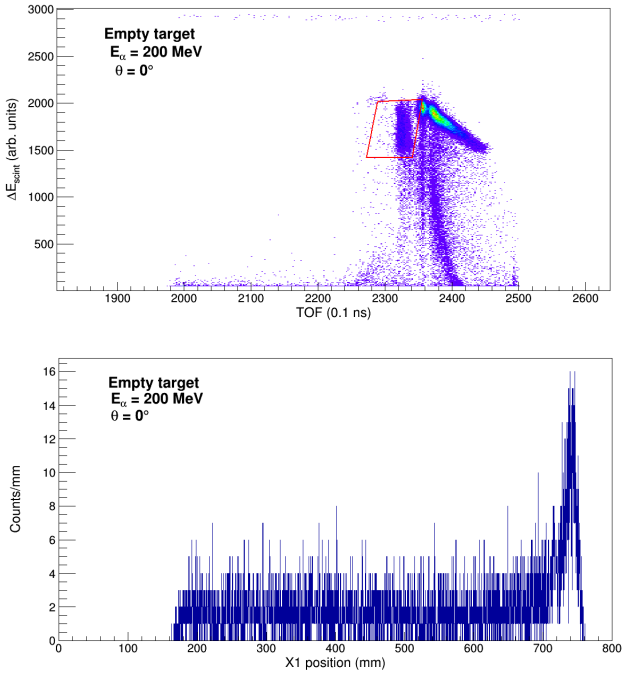


Figure 3.10: Top: Paddle1-versus-TOF PID plot for α particles incident on an empty target showing the alpha PID gate. Bottom: Position spectrum for the empty obtained from the alpha PID software gate (marked in red).

3.5.2 Data alignment and chained data

During the beam-time the value of the measured TOF changes. The TOF changes are mainly due to small SSC RF phase and voltage changes over time, done by the SSC operators to maintain the beam intensity when compensating for small changes in the SSC magnetic fields. A Gaussian fitting was applied to the alpha region in the TOF spectrum to quantify these shifts, in order to correct for it relative to the alpha peak in the TOF spectrum of the first run of the particular beam period. This correction in the TOF then allows for a single PID gate to be used for a whole beam period, which simplifies the analysis. The above mentioned SSC changes also have the effect of small energy changes in the beam, which manifests itself in small position changes in the focal pane. In order to take these drifts into account, the position of a prominent peak in the ^{24}Mg(α, α') spectrum was determined for each run. These were then used to calculate offsets for each run relative to a run in the beginning of the weekend. Typical shifts in both the focal plane position and the TOF for each run of the calibration target (^{24}Mg) relative to the first run in the list, with their corresponding position resolutions, are presented in Table 3.4. The big difference between run number 1051 and 1084 is due to a retune of the beam due to problems with the accelerator cooling water supply.

These position shifts are factored into the analysis to ensure that optimum position resolution of the chained data is achieved, where all relevant data files of a particular isotope are combined to form a single chained data set. The position resolution (σ) of the chained data set is 1.42362 mm.

3.5.3 Lineshape correction

The horizontal focal plane position, $X1_{pos}$, is known to show dependence on the scattering angle, θ_{SCAT}, and the vertical focal plane position, Y1. This dependence is a result of kinematics and first and second order aberrations in the K600 magnetic fields which are corrected only to first order during the experimental procedures with the two trim coils (K and H) as stated in Section 3.2. However, the aberrations are not fully corrected, as indicated by the shape of the excited state shown in Fig. 3.11. The consequence of this is a

Table 3.4: TOF and position offsets with the corresponding position resolutions for different experimental runs. The position offsets and resolution were obtained for the 9.305 MeV 0^+ state in ^{24}Mg.

Run Number	TOF Offset (ns)	Position Offset (mm)	Position Resolution σ (mm)
1041	0	0	1.165
1045	-0.9	-0.181	1.190
1051	0.7	+0.962	1.135
1084	6.8	-8.156	1.212
1090	6.0	-9.844	1.317
1094	5.8	-10.264	1.304
1099	5.6	-10.339	1.309
1105	6.0	-9.455	1.347
1112	7.4	-8.505	1.295
1117	6.4	-8.72	1.294
1123	5.5	-9.815	1.360
1128	5.4	-10.105	1.340
1133	5.8	-9.894	1.400
1138	5.1	-9.941	1.355
1144	5.6	-9.452	1.349
1149	5.7	-8.699	1.306

poor position and thus energy resolution. In order to obtain the best possible energy resolution, the remaining corrections are done offline with software by employing a lineshape correction procedure. Offline corrections also includes the correction of the dependence of the horizontal focal plane position, $\mathrm{X1_{pos}}$, on the vertical position, Y1.

The corrected focal plane position, $X1_{\mathrm{posC}}$, is given as

$$X1_{\mathrm{posC}} = X1_{\mathrm{pos}} - (f_1\theta_{\mathrm{SCAT}} + f_2{\theta^2}_{\mathrm{SCAT}} + f_3{\theta^3}_{\mathrm{SCAT}} + f_4{\theta^4}_{\mathrm{SCAT}} + f_5{\theta^5}_{\mathrm{SCAT}}) - g_1 Y1, \tag{3.4}$$

where $f_1 = 0.239$, $f_2 = 0.433$, $f_3 = -0.036$, $f_4 = -0.044$, $f_5 = -0.005$, and $g_1 = 0.010$. The corrected lineshapes for the ^{24}Mg target are shown in Fig. 3.11.

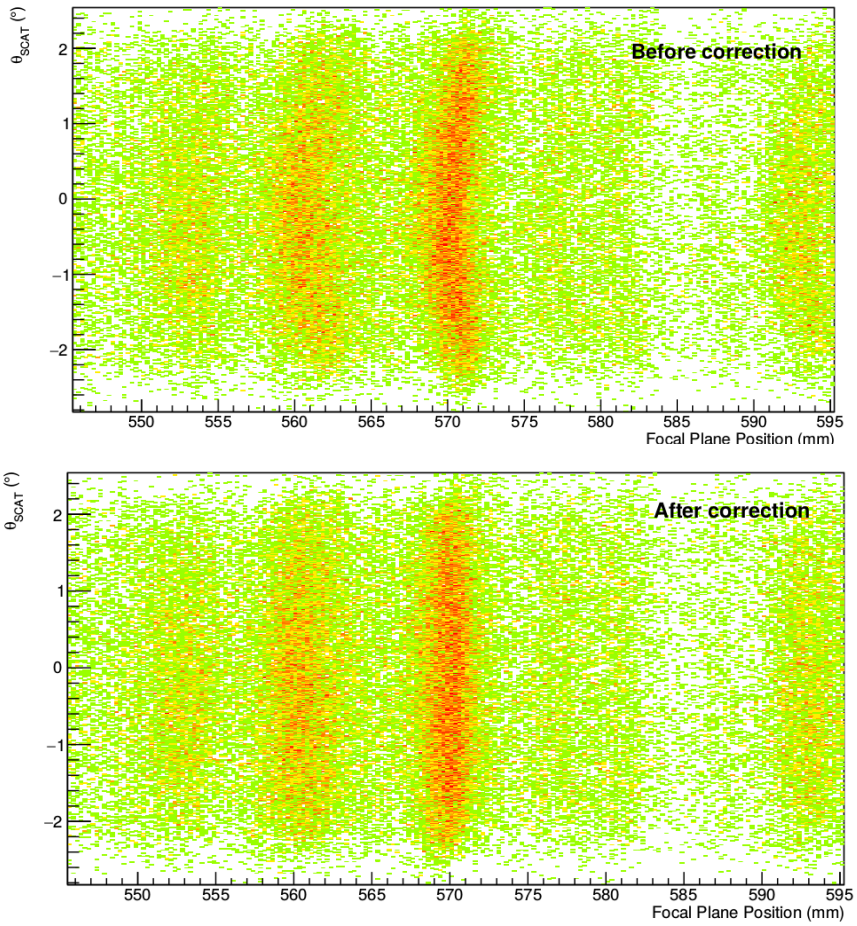


Figure 3.11: A plot of scattering angle versus the focal plane position (top) before and after (bottom) lineshape correction for ^{24}Mg.

3.5.4 Background subtraction

Background subtraction is necessary to remove the remaining background in the position spectrum after the PID gate is applied. The remaining background is due to beam halo and target related halo where α-particles undergo scattering inside the K600 which produce reaction products with similar ΔE and TOF characteristic to that of scattered α-particles of interest as indicated in Fig. 3.10. The only way one can distinguish these particles from the physics events is by looking at the vertical scattering information. Figure 3.12 shows the vertical focal plane position, Y_{fp}, versus the horizontal position, X_{fp}. Since the K600 was operated in a vertical focused mode for zero degree measurements the background regions B1 and B2 could be chosen to be distinct from the central region ΔY, which contains the contributions from both the good events and background. The range of B1 is

Y1 > −32 mm to Y1 < −12 mm and that of B2 is Y1 > 25 mm to Y1 < 30 mm. The central region has a range of Y1 > −12 mm to Y1 < 25 mm. The experimental background is assumed to be evenly distributed in the vertical direction, so that the sections B1 and B2 can be used to estimate the background.

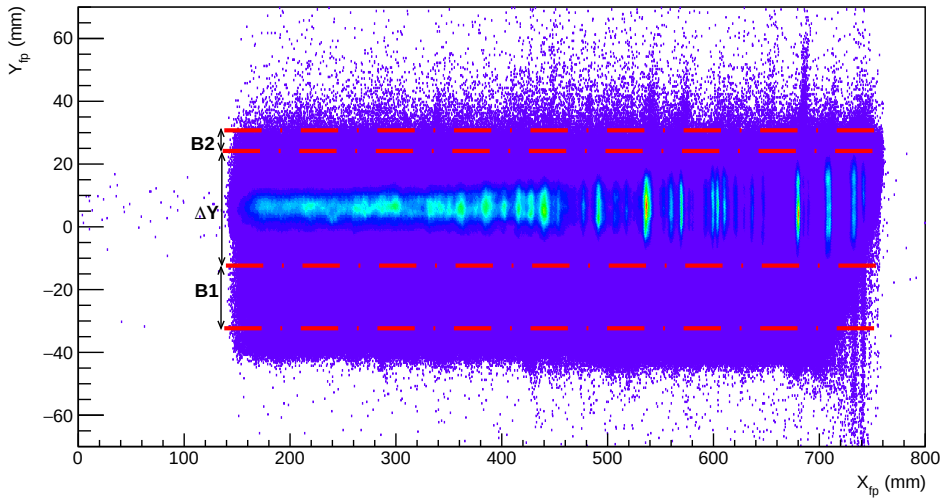


Figure 3.12: A scatter plot of Y_{fp} versus X_{fp} showing the background regions B1 and B2, and the central region ΔY containing events of interest on top of the backgrounds.

The focal plane position spectrum before the background subtraction for ^{24}Mg(α,α') at 0° is shown in Fig. 3.13. A background-free focal plane position spectrum for ^{24}Mg(α,α') at 0° is shown in Fig. 3.14.

3.5.5 Energy calibration

In order to determine the excitation energies for different targets, it is essential to calibrate the focal plane in terms of the α-particle momentum (p). In the experiment reported in this thesis, the momentum calibration was achieved through the ^{24}Mg(α,α') reaction, which has a well-known spectrum with multiple resolved excited states.

A gaussian-plus-polynomial fit was employed to determine the peak position of the well-resolved peaks in the ^{24}Mg(α,α') lineshape corrected position spectrum. Excitation energies were assigned to these peaks by a direct

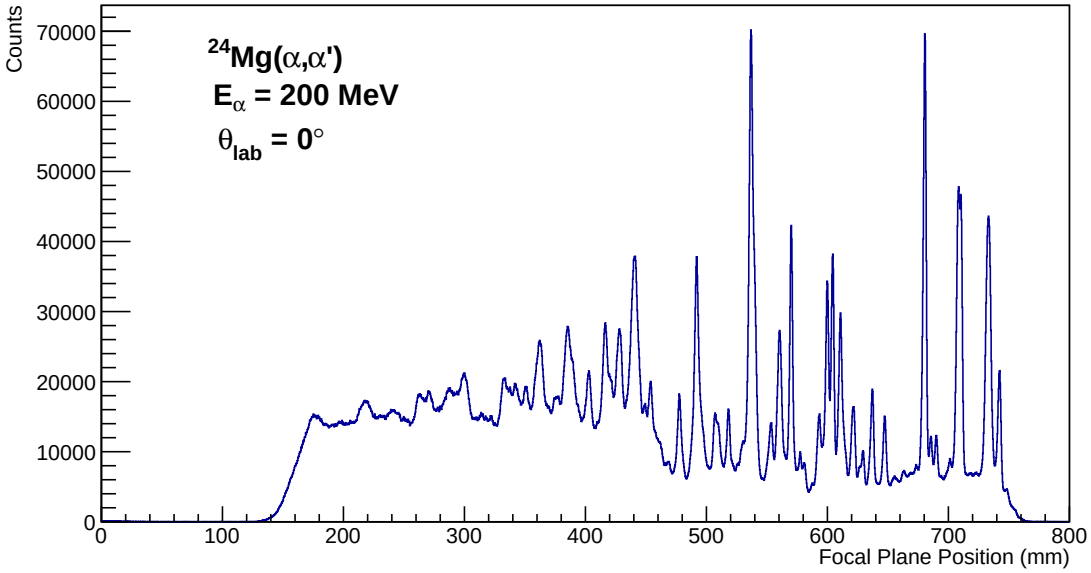


Figure 3.13: The focal plane position spectrum for inelastic α scattering from ^{24}Mg target before the background subtraction.

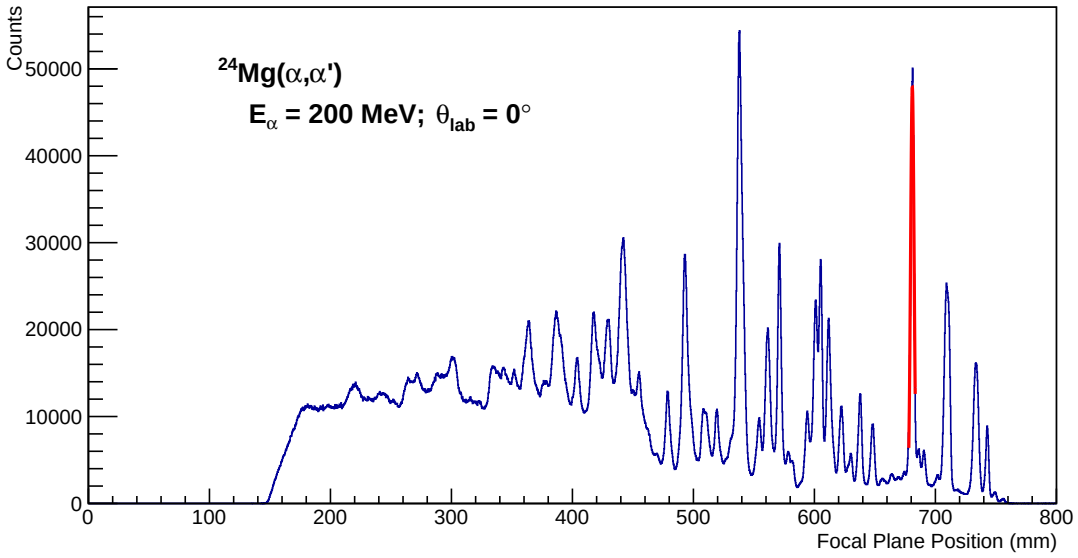


Figure 3.14: The lineshape-corrected and background-subtracted focal plane position spectrum for inelastic α scattering from ^{24}Mg. The peak in red is the 9.305 MeV 0^+ state that was used to obtain the TOF and position offsets.

comparison of the measured position spectrum with the excitation energy spectrum of ^{24}Mg(α,α') from existing literature [Kaw10]. The α-particle momentum, p (= QBρ), for each of the assigned excitation energies was calculated using a code JRelKin [Vis03]. The assigned energies with the corresponding calculated momentum, based on a beam energy of 200 MeV and scattering angle 0°, are summarised in Table 3.5.

The calculated scattered particle momentum, p was fitted accordingly with a second-order polynomial (see Fig. 3.15) of the form:

$$p = a_0 + a_1 X1_{\mathrm{posC}} + a_2 X1^2{}_{\mathrm{posC}}, \tag{3.5}$$

where $\mathrm{X1_{posC}}$ is the corrected focal plane position. The calibration parameters were obtained to be: $a_0 = 3.74314 \times 10^3$, $a_1 = 3.57009 \times 10^{-1}$ and $a_2 = -5.71374 \times 10^{-6}$.

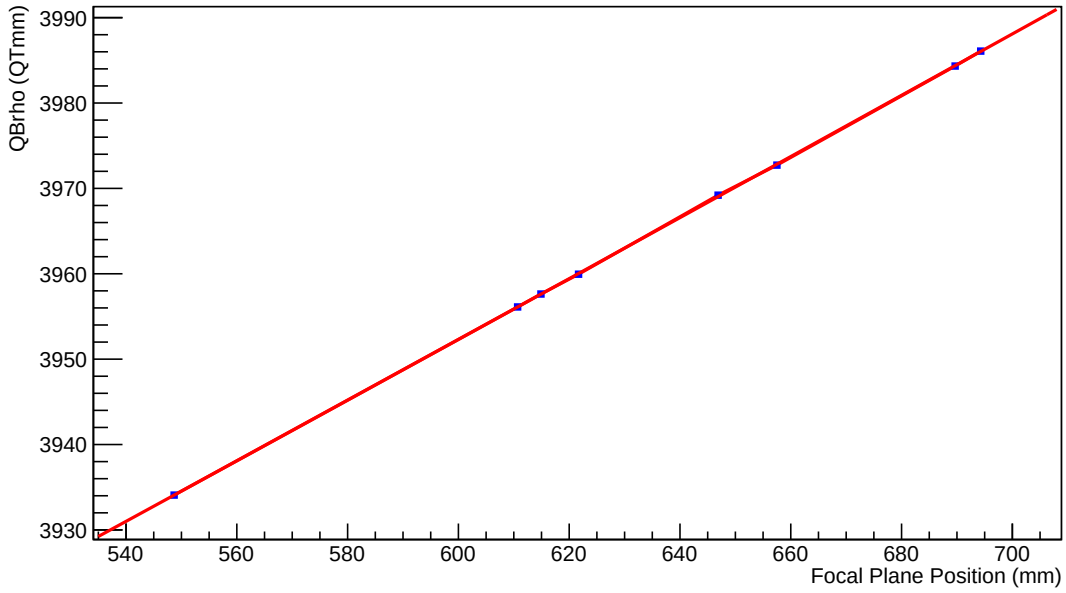


Figure 3.15: A second-order polynomial fit of the momentum of the scattered particle plotted against the corrected focal plane position.

Calculation of the excitation energy from the momentum is achieved using standard relativistic equations for binary kinematics [Whe14],

$$E_{\mathrm{x}} = E_0 + m_1 + \sqrt{p_2^2 - m_2^2} - (p_0^2 + p_2^2 + 2p_0p_2cos(\theta) + m_3^2)^2, \tag{3.6}$$

where the projectile, target, scattered particle and recoil nucleus are denoted

as 0, 1, 2 and 3, respectively. In this way, the calibration obtained for the ^{24}Mg could be applied to all the calcium isotopes (^{40,42,44,48}Ca) considered in the experiment.

3.5.5.1 Target thickness effects

Since the targets utilised in this experiment are more than 1 mg/cm^2 thick, the α-particles lose a significant amount of energy in the target. This was taken into account during the calibration procedure.

Consider the two extreme scenarios where either the 200 MeV α-beam lose energy as it pass through the target, and the nuclear reaction of interest happens at the down stream surface of the target, or a nuclear reaction of interest occurs at the upstream face of the target and the scattered α-particle undergoes energy loss when traversing the target. The energy of the particle observed in the focal plane is, therefore, influenced not purely by the reaction kinematics, but also the energy loss in the target.

It is important to take this energy loss into account in the position–to–momentum calibration. When doing the calibration for the ^{24}Mg target, the momentum associated with a specific excited state must take the energy loss in the target into account, so that the momentum of the alphas reaching the focal plane can be correctly calculated. This then also means that in the reverse calculation, from momentum (calculated from the position spectrum) to excitation energy, the target thickness of any particular target must be incorporated in the excitation energy determination. In other words, the momentum calibration procedure will give a correct momentum as observed in the focal plane. Translating this momentum to the correct excitation energy for a random target of thickness Z means that the average energy loss ΔE_{Z} in the target must be subtracted.

The target thickness effect in the momentum calibration procedure was determined using a relativistic kinematic code called JRelkin [Vis03]. With a finite target thickness the code calculates the kinematics for beam interaction at the front (upstream side) and back (downstream side) of the target, and for each excitation energy two $QB\rho$ values were produced. The average of

the two values, for each excitation energy, was taken for the $QB\rho$ (or momentum) values in this analysis.

Table 3.5 shows the excited states in ^{24}Mg and the average $QB\rho$ obtained from the JRelKin calculation. According to this calculation, for a 200 MeV α beam on 2.1 mg/cm^2 ^{24}Mg, the average energy loss is 0.086 MeV. Similar calculations were done for the calcium targets using the thicknesses listed in Table 3.3 and the energy loss due to target thickness effect for ^{40}Ca, ^{42}Ca, ^{44}Ca and ^{48}Ca targets are 0.040 MeV, 0.053 MeV, 0.057 MeV and 0.044 MeV, respectively. This effect is accounted for in this analysis by subtracting the average energy loss from the calculated excitation energy values.

Table 3.5: Focal-plane positions of well-known excited states in ^{24}Mg and the calculated average $QB\rho$ for a 200 MeV alpha beam on 2.1 mg/cm^2 thick target. See text for detail.

Position (mm)	Excitation Energy (MeV)	J^π	Average $QB\rho$ (QTmm)
689.90	9.00334(9)	2^+	3986.794
685.40	9.14599(15)	1^-	3985.228
680.40	9.30549(24)	0^+	3983.476
647.40	10.3605(13)	2^+	3971.868
637.00	10.6797(4)	0^+	3968.348
610.77	11.5182(6)	2^+	3959.086
604.30	11.7281(10)	0^+	3956.764
599.80	11.8649(13)	1^-	3955.250
536.90	13.8500(20)	Not assigned	3933.205

The calibrated excitation–energy spectrum for ^{24}Mg was obtained from the position–to–momentum calibration together with the excitation energy calculation as shown in Eq. 3.6 after which 0.086 MeV was subtracted. The resulting excitation–energy spectrum is shown in Fig. 3.16. A magnified version of the spectrum showing peaks of identified states is shown in Fig. 3.17. The correctness of the calibration was ascertained by comparing the values of excited states in ^{24}Mg reported by NNDC [Fir07] and Kawabata [Kaw10] with the values obtained in this experiment as shown in Table 3.6. The difference is less than 10 keV. Figure 3.18 shows the differences versus the corresponding focal plane positions as listed in Table 3.5. The displayed errors correspond to the uncertainties (standard deviation) of resonance

energies within literature [Fir07] and are of Gaussian distribution.

Table 3.6: Comparison of ^{24}Mg excited states obtained in this work with values reported in NNDC [Fir07] and by Kawabata *et al.* [Kaw10]. The last column shows the difference between calibrated excited states and assigned excited states.

J^{π}	NNDC (MeV)	Kawabata (MeV)	This work (MeV)	Difference (MeV)
2^+	9.00334	-	9.004	0.0006
1^-	9.14599	-	9.148	0.002
0^+	9.30539	-	9.304	-0.0014
2^+	10.3605	-	10.364	0.0035
0^+	10.6797	-	10.684	0.0043
2^+	11.5182	-	11.517	-0.0012
0^+	11.7281	-	11.724	-0.0041
1^-	11.8649	-	11.864	-0.0009
Not assigned	13.8500	-	13.854	0.004
Not assigned	-	15.2500	15.260	0.010
Not assigned	-	17.6400	17.634	-0.006

3.5.6 Experimental double differential cross-sections

Experimental double differential cross-sections (in units of mb/srMeV) were obtained for the ^{24}Mg(α,α') and ^{40,42,44,48}Ca(α,α') reactions using the following equation:

$$\frac{d^2\sigma}{d\Omega dE} = \frac{10^{27} \times N_{\mathrm{c}}}{N_{\mathrm{o}} \times \rho \times D \times \Delta\Omega \times \Delta E \times \varepsilon}, \tag{3.7}$$

where N_{c} is the corrected number of counts in an energy bin ΔE (MeV), N_{o} is the total number of incident α-particles on the target, ρ is the number of target nuclei per unit area (in mb), D is the electronic dead time correction factor (about 0.99 for this experiment), $\Delta\Omega$ is the solid angle of the K600 magnetic spectrometer in sr (3.48 msr) and ε is the total VDC efficiency.

The total number of incident α-particles, N_o, is calculated by:

$$N_{\rm o} = \frac{CI \times R \times 10^{-12}}{q}, \tag{3.8}$$

where CI is the scalar read-out of the current integrator, R is the selected range (in nA) of the current integrator and q $(= 2e)$ is the α-particle electric charge in Coulombs, while e is the charge of a proton.

The number of target nuclei per unit area, (ρ), is given by:

$$\rho = \frac{\lambda \times N_{\rm A}}{A}, \tag{3.9}$$

where λ is the target thickness in g cm^{-2}, $N_{\rm A}$ is the Avogadro number and A is the mass number of the nucleus under consideration.

The total VDC efficiency, ε, which is an indication of the ability of all the wireplanes (X1, U1, X2, U2) to detect scattered charged particles in the focal plane, is given by the product of the efficiencies of all the wireplanes.

$$\varepsilon = \varepsilon_{\rm X1} \times \varepsilon_{\rm X2} \times \varepsilon_{\rm U1} \times \varepsilon_{\rm U2}. \tag{3.10}$$

However, during the experiment reported here, the X2 chamber was, for reasons unknown, always less efficient. Therefore, in this study data from the X2 wire-plane was not considered, and the total VDC efficiency is calculated as follows:

$$\varepsilon = \varepsilon_{X1} \times \varepsilon_{U1} \times \varepsilon_{U2}. \tag{3.11}$$

It should be noted that the use of three wire planes does not in any way compromise the extracted data in the present study. This is because the X1 wire-plane was used to obtained the focal plane position, a combination of the X1 and U1 wire-planes was used to obtain the vertical dimension Y1, and the two U wire-planes were used to obtain the horizontal component of the focal plane angle, especially since the experiment was perform in the focus mode. The horizontal component of the focal plane angle is related to the horizontal component of the scattering angle through the ion optics of the K600.

The associated statistical errors in the double-differential cross-sections were

obtained as follows:

$$\Delta \frac{d^2\sigma}{d\Omega dE} = {N_{\rm c}}^{-1/2} \frac{d^2\sigma}{d\Omega dE}. \tag{3.12}$$

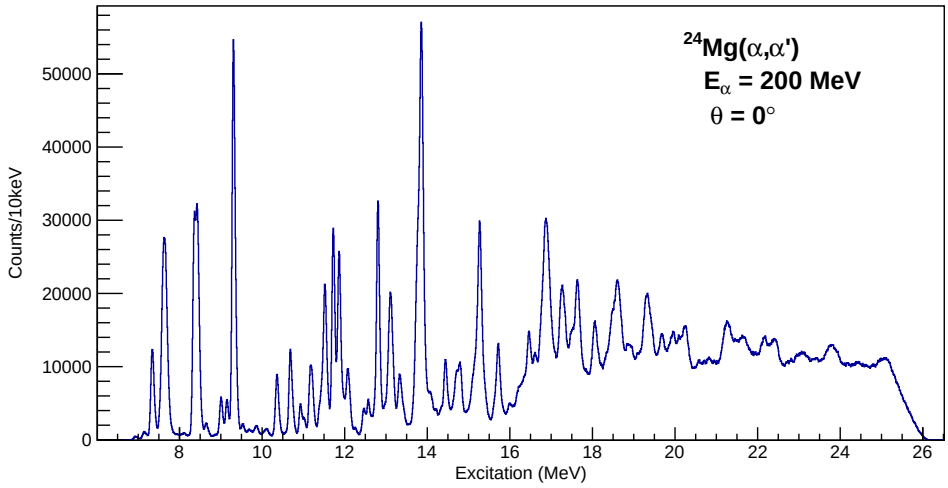


Figure 3.16: The ^{24}Mg excitation-energy spectrum accessible in the PR260 0° measurements.

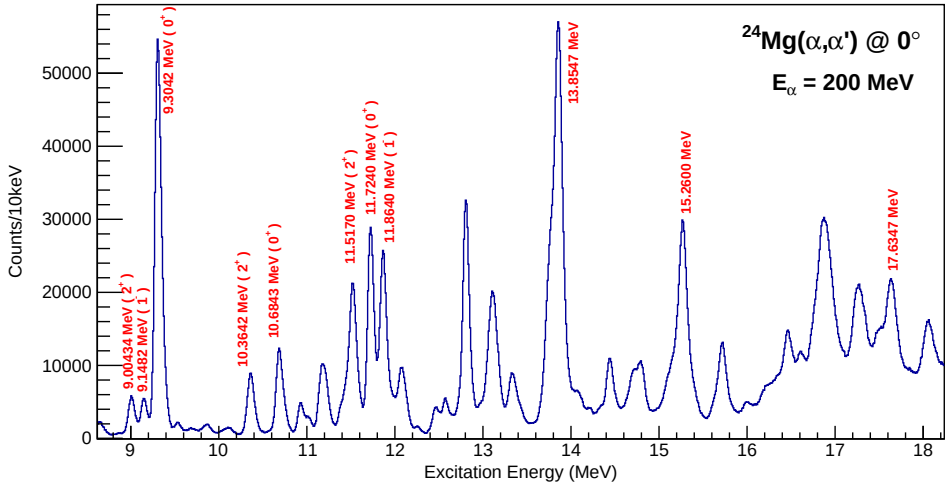


Figure 3.17: A magnified ^{24}Mg excitation-energy spectrum showing identified states used for the calibration. The energy resolution is 85.7 keV full width at half maximum (FWHM), based on the 9.305 MeV 0^+ state.

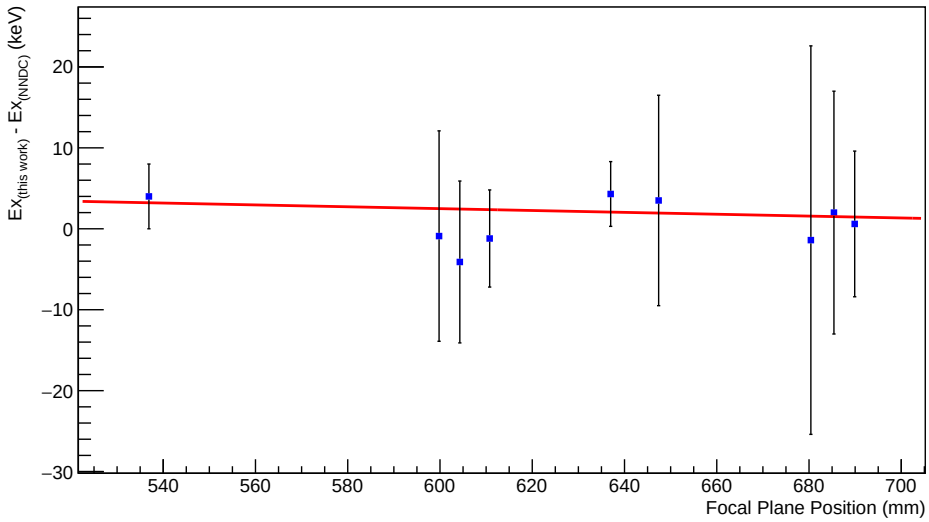


Figure 3.18: A plot of the difference between the calibrated (this work) and the assigned excited states versus the focal plane position

3.6 Data extraction and offline analysis: 4° measurements

In the last two weekends of June 2017, under the project number PR260, additional data were acquired with the K600 spectrometer set at 4°. This additional measurement was necessary in order to determine the contributions of other multipoles, especially the ISGQR, in the ISGMR region at zero-degrees.

During the 4° (α,α') measurements, unlike the case for the 0° data, only the scattered particles were transported through the spectrometer, while the primary beam was stopped before entering the spectrometer by an internal beamstop installed just in front of the K600 quadrupole.

The steps involved in extracting and optimising 4° data sets are similar in many respects to that of 0° data analysis. The first step is the identification of the α-particle at the focal plane using the TOF and energy deposited in the first scintillator (paddle 1). A typical PID spectrum is shown in Fig. 3.19. This can be compared to Fig. 3.6. Also, before moving on with the rest of the analysis, it was necessary to ascertain the Look Up Table (LUT) was good and properly constructed. A typical driftlength spectrum in Fig. 3.20 indicates a good LUT.

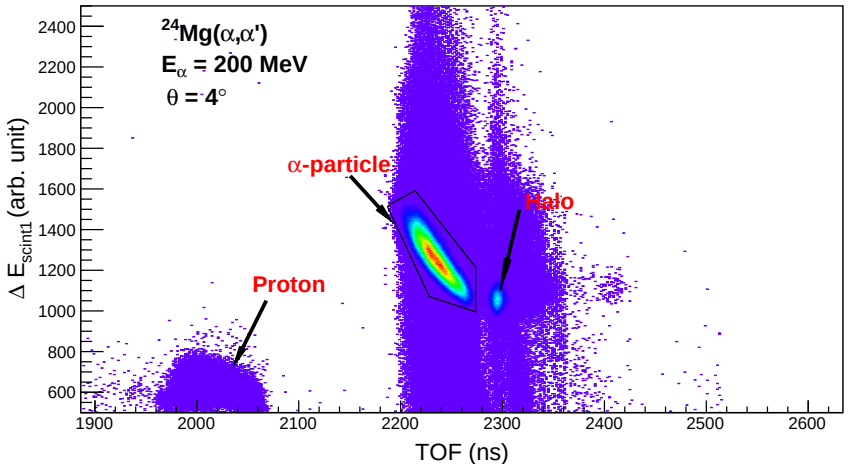


Figure 3.19: A plot of energy deposited in paddle 1 versus TOF for α particles incident on a ^{24}Mg target showing various PID loci.

It was necessary to correct for the changes in the TOF as well as both in the horizontal- and vertical focal-plane positions (x_{fp} and y_{fp}), as discussed in Section 3.5.2. Furthermore, it was necessary to account for the y_{fp} offset because the vertical scattering angle was calculated from the y_{fp} and changes in this variable would affect scattering angle calculation. Accurate determination of the scattering angle in 4° measurements requires precise information of both the horizontal and the vertical positions in the focal plane. Table 3.7 shows a list of TOF, x_{fp} and y_{fp} offsets per run for ^{48}Ca. After this, the data were chained and the analysis proceeded with lineshape correction, angle calibration (See Section 3.6.1 below), energy calibration, background subtraction and cross-section calculations (See Section 3.2.1.2).

3.6.1 Angle calibration

Angle calibration measurements were performed with the spectrometer positioned at 4° and with a multi-hole collimator (colloquially called 'the pepperpot') positioned downstream the target in the normal K600 collimator position. Using the above mentioned spectrometer setup, ^{12}C(α,α') measurements were performed in order to obtain the angle calibration. During these measurements, the fields of the D1 magnet of the spectrometer were adjusted appropriately to shift the elastic scattering peak across the focal plane in order to be able to reconstruct both the horizontal (θ_{SCAT}) and

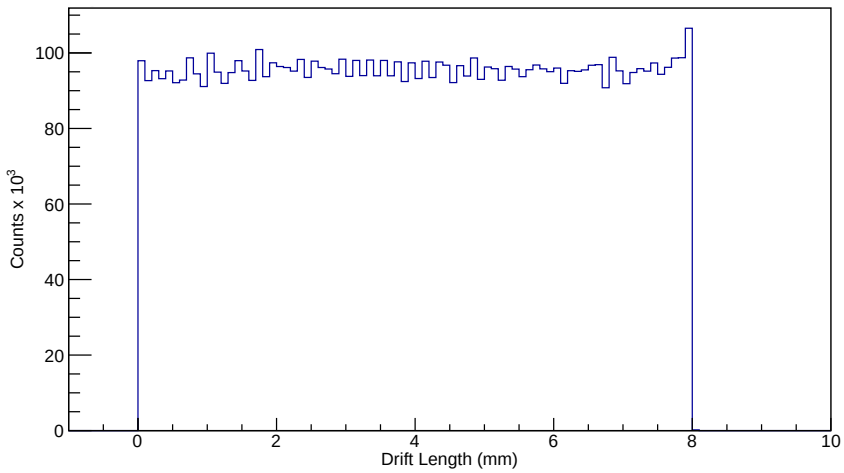


Figure 3.20: Drift length.

Table 3.7: The horizontal and vertical focal plane position offsets, and the TOF offset per run for ^{48}Ca relative to run 3024.

Run Number	x_{fp} Offset (mm)	y_{fp} Offset (mm)	TOF Offset (ns)
3024	0	0	0
3046	24.5203	-1.4673	-7
3052	23.2999	-3.0834	-6
3057	22.8566	-4.4208	-7
3062	23.1394	-4.9329	-6
3067	24.0122	-4.1800	-3
3073	24.2176	-5.7047	-4
3078	25.0571	-4.7810	-5
3084	24.6221	-2.7954	-8
3089	24.4000	-2.0760	-9
3092	24.2819	-1.6667	-10
3096	24.6516	-2.1777	-10
3101	24.4422	-2.5601	-11
3106	24.4438	-2.5732	-11
3111	24.6916	-3.6992	-11
3116	24.4813	-3.3337	-12

the vertical (ϕ_{SCAT}) scattering angles from the measured focal plane angle, θ_{fp}. It should be noted that θ_{SCAT} is the horizontal scattering angle relative to the value of θ_{K600}. In the offline analysis, the reconstruction was done using the equations of the form:

$$\theta_{\mathrm{SCAT}} = \theta_{\mathrm{fp}} \sum_{i=0}^{2} a_i x_{fp}^{i} + \sum_{i=0}^{2} b_i {x^i}_{\mathrm{fp}}, \tag{3.13}$$

and,

$$\phi_{\mathrm{SCAT}} = y_{\mathrm{fp}} \sum_{i=0}^{3}\sum_{j=0}^{2} c_{ij} {x^i}_{\mathrm{fp}} {\theta^i}_{\mathrm{SCAT}} + \sum_{i=0}^{3}\sum_{j=0}^{2} d_{ij} {x^i}_{\mathrm{fp}} {\theta^i}_{\mathrm{SCAT}} \tag{3.14}$$

where the constants a_i, b_i, c_{ij} and d_{ij} are the fit parameters.

The procedure listed below summarises the method used to obtain the fit parameters required for horizontal scattering-angle reconstruction:
1. Plots of the observed θ_{fp} were made for the elastic peak at different positions using the pepperpot runs.

2. Multiple-gaussian curve fitting was performed on the seven peaks as shown in Fig. 3.21. The purpose of this was to determine the centroids of the seven peaks in the θ_{fp} and assign to them the known values of θ_{SCAT}. Similar plot for θ_{SCAT} is shown in Fig. 3.22.

3. A plot of θ_{fp} versus θ_{SCAT} was created, at specific x_{fp}, in order to determine the function which converts θ_{fp} to θ_{SCAT}. As this function also depends on x_{fp} an equation of the form of Eq. (3.13) is necessary.

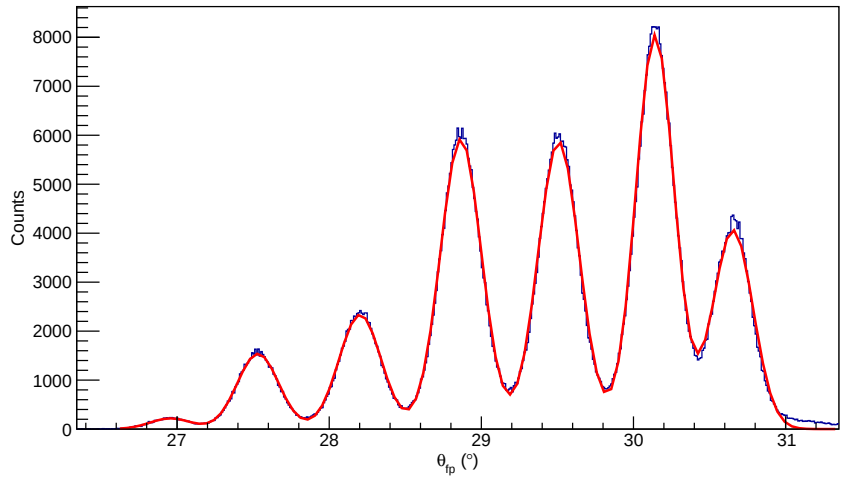


Figure 3.21: A focal plane angle θ_{fp} plot for the pepperpot run showing the associated Gaussian fits to the observed peaks for $x_{\mathrm{fp}} = 613$ mm.

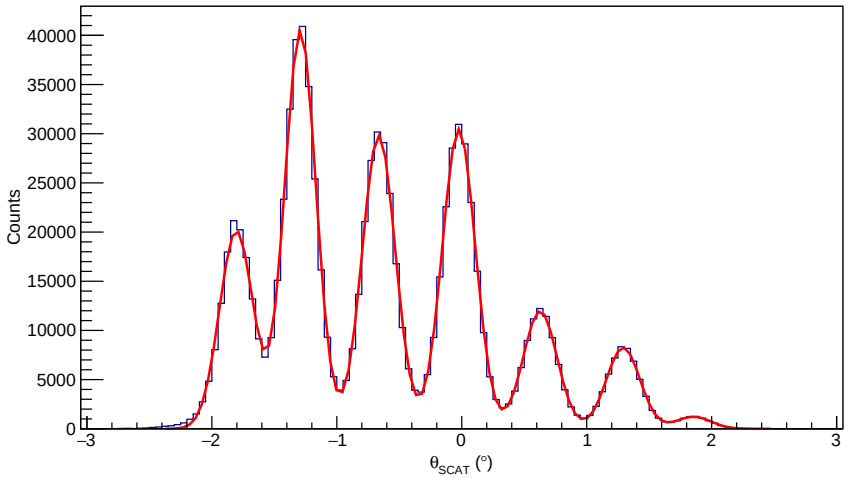


Figure 3.22: The resultant scattering angle θ_{SCAT} plot for the pepperpot run 2022 at $x_{\mathrm{fp}} = 613$ mm which illustrates the reconstructed scattering angle relative to θ_{K600}.

Similarly, for various x_{fp} regions across the focal plane as well as values of

θ_{SCAT} the y_{fp} values were obtained by fitting with a Gaussian distribution. The corresponding ϕ_{SCAT} for each hole was assigned, and then fitted with equation 3.14 via a multi-dimension linear fitter. The values of ϕ_{SCAT} and θ_{SCAT} range from -2 to +2 degrees, which is the angular size of the spectrometer aperture. The final calibrated plot of ϕ_{SCAT} versus θ_{SCAT} is shown in Fig. 3.23.

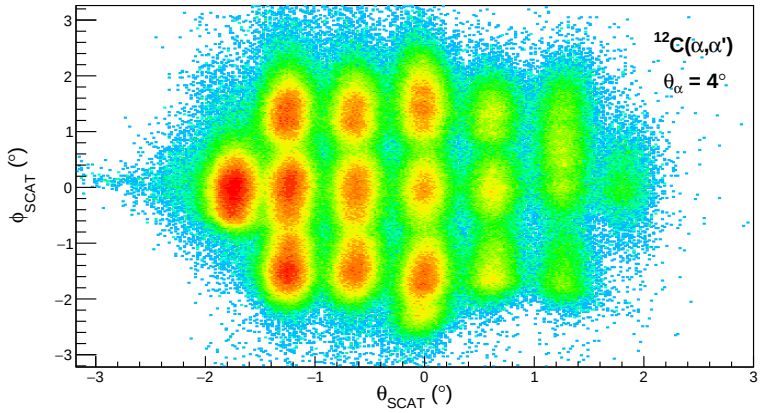


Figure 3.23: Calibrated horizontal and vertical scattering angle for the pepperpot collimator relative to $\theta_{\mathrm{K600}} = 4°$.

The polar angle Θ at which the scattered α-particle was emitted can be calculated from calibrated values of ϕ_{SCAT} and θ_{SCAT} using the equation of the form [Nev11]:

$$\Theta^2 = \phi^2{}_{\mathrm{SCAT}} + (\theta_{\mathrm{SCAT}} + \theta_{\mathrm{K600}})^2, \tag{3.15}$$

where θ_{K600} is the horizontal angle of the K600 spectrometer aperture with respect to the beam direction. The polar angle Θ was used to obtain angular distributions with a finer granularity than the 4 degree aperture of the spectrometer. A plot of ϕ_{SCAT} versus θ_{SCAT} from the normal collimator is shown in figure 3.24, with the red circle signifying the 4 degree aperture of the K600 spectrometer. Similar plots with scattering angle $\Theta = \sqrt{\phi^2{}_{\mathrm{SCAT}} + (\theta_{\mathrm{SCAT}} + \theta_{\mathrm{K600}})^2} \leq 1°$, in the regions of 2°-3°, 3°-4°, 4°-5° and 5°-6° are shown in Fig. 3.25.

The solid angle $\Delta\Omega$ is required in order to calculate the double-differential cross-sections. For a given region of Θ and θ_{K600} the solid angle $\Delta\Omega$ can be calculated as follows [Hub18]:

$$\Delta\Omega = \int_{\Theta_1}^{\Theta_2} 2sin\Theta\Phi_{\mathrm{max}}(\Theta, \theta_{\mathrm{K600}})d\Theta, \tag{3.16}$$

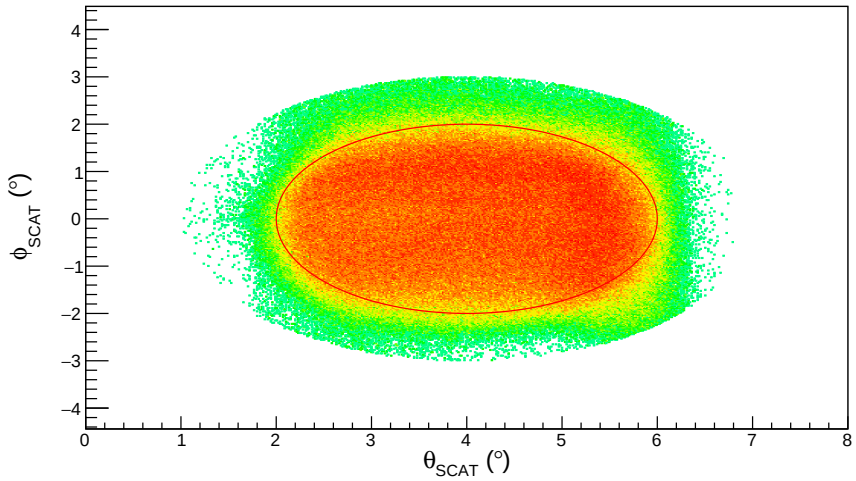


Figure 3.24: The focal plane angle versus scattering angle plots from the normal collimator showing the 4° aperture of the K600 spectrometer represented by the red circle.

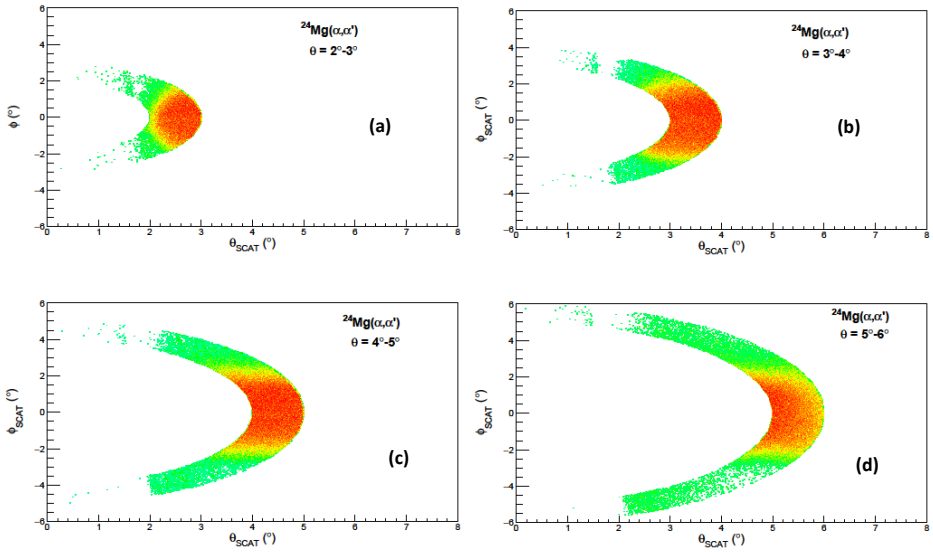


Figure 3.25: The focal plane angle versus scattering angle plots at various angle cut.

Table 3.8: Calculated solid angle $\Delta\Omega$ for various range of Θ.

Θ (deg.)	$\Delta\Omega$ (msr)
2-3	0.609404
3-4	1.10423
4-5	1.24358
5-6	0.876741
2-6	3.48

where

$$\Phi_{\max}(\Theta, \theta_{\mathrm{K600}}) = cos^{-1}\left(\frac{1}{sin\Theta sin\theta_{\mathrm{K600}}}\left(\frac{r_0}{\sqrt{\alpha^2 + r_0^2}} - cos\Theta cos\theta_{\mathrm{K600}}\right)\right), \tag{3.17}$$

where r_0 and α represent the distance between the target and the aperture, and the radius of the aperture, respectively. For the various regions of Θ shown in Fig. 3.25, the calculated $\Delta\Omega$ with $\theta_{\mathrm{K600}} = 4^\circ$ are presented in Table 3.8.

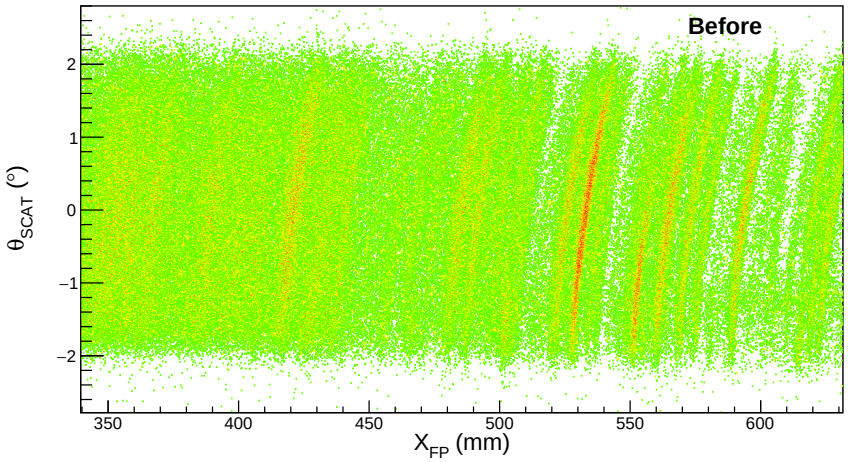


Figure 3.26: x_{fp} versus θ_{SCAT} plot before the lineshape correction.

3.6.2 Energy calibration

Energy calibration was a crucial part of the data optimisation. To achieve this, a calibration ^{24}Mg target, was bombarded with a 200 MeV α beam. After a good angle calibration has been established and the focal plane position

corrected for kinematic aberrations, the lineshape-corrected position can be converted into excitation energies of the populated ^{24}Mg nucleus as explained in Section 3.5.5. Figure 3.28 shows the final excitation energy spectrum for ^{24}Mg(α,α'). Applying a Gaussian-plus-polynomial fit the peak around 7.6 MeV in both spectral, energy resolutions of 91 keV and 120 keV were obtained for ^{24}Mg and ^{48}Ca, respectively.

A step-by-step procedure employed in the energy calibration is detailed as follows:
1. Final background-subtracted position and lineshape corrected spectrum of ^{24}Mg(α,α') was obtained as explained in Section 3.5.4.

2. Peaks were identified, fitting Gaussian-plus-polynomial on the individual peaks and recording their respective centroids.

3. Excitation energies of each peak were estimated and assigned, according to the energy levels of ^{24}Mg in the Table of Isotopes [Fir07] together with the ones published by K. van der Borg *et al.* [Bor81].

4. Two-body kinematics calculations were performed using JRelKin [Vis03]. This provides the expected α-particle energies of the identified excited states at the focal-plane.

5. Alpha-particle energies obtained in step 4 above were converted to

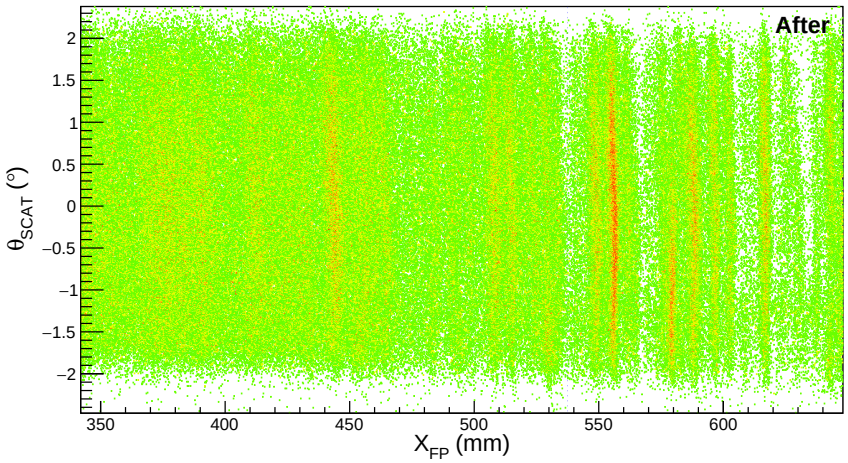


Figure 3.27: x_{fp} versus θ_{SCAT} plot after the lineshape correction.

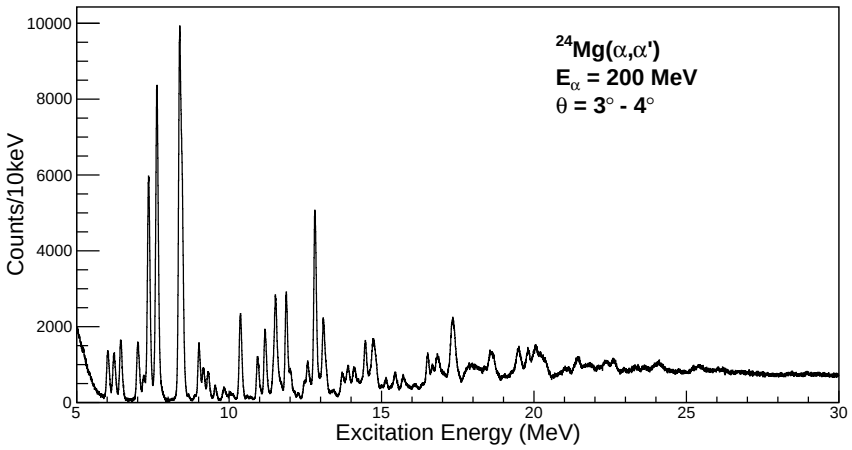


Figure 3.28: Measured excitation energy spectrum for the ^{24}Mg(α,α') reaction, used for energy calibration.

α-particle momenta P_α.

6. A plot of P_α versus X_{fp} was obtained. A quadratic polynomial fit of the form in Eq. (3.5) was fitted. The resulting calibration parameters for the 4° dataset are $a_0 = 3.68773 \times 10^3$, $a_1 = 4.87479 \times 10^{-1}$ and $a_2 = -3.4479 \times 10^{-6}$.

7. The momenta were converted into excitation energies using Eq. (3.6). The components of Eq. (3.6) were calculated for the calibration target as well as for each of the calcium nuclei, and the conversion from excitation-energy calibration was implemented across all of the 4° datasets.

Chapter 4

Results, analysis and discussion

In this chapter firstly oxygen contamination background-free experimental spectra for ^{48,44,42,40}Ca(α,α') are obtained for the 0° and 4° data. Discrete peaks from ^{16}O(α,α') are identified at the lower end of the measured excitation energy spectra for the four calcium isotopes and a detailed procedure of how the contaminant peaks and continuum were removed is given in Section 4.1.1. The Difference-of-Spectra (DoS) technique is applied using the 0° and 4° data to determine the strength of the ISGMR. Experimental determination of ISGMR is somewhat challenging, mainly due to overlap with the ISGQR. In order to determine the appropriate scattering angle cut from the 4° data for which the background from other multipoles, predominantly the ISGQR, can be removed from the 0° data, DWBA calculations were performed and the results are presented in Section 4.2.1. Section 4.2.2 deals with the detailed explanation of the DoS technique. A step-by-step procedure for obtaining the fractional $E0$ EWSR and the corresponding $E0$ strength function from the difference spectra is discussed in Section 4.2.3. Then follows Section 4.4 which deals with the extraction of characteristic energy scales in the excitation energy region of the ISGMR from both experimental data and theoretical calculations using the Continuous Wavelet Transform (CWT) technique. The chapter ends with the extraction of the level density of 0^+ states in ^{48}Ca and ^{40}Ca described in Section 4.5. It should be noted that, for the sake of readability, figures are placed at the end of each section.

4.1 Overview of the measured experimental (α, α') data

Experimentally measured excitation-energy spectra for ^{48}Ca, ^{44}Ca, ^{42}Ca and ^{40}Ca at $\theta_{\mathrm{Lab}} = 0^{\circ}$ and 4° are presented in Figs. 4.1 and 4.2, respectively. Contaminants from oxygen are identified and shown as can been seen in the figures. Detailed procedure of how the contaminants were removed is presented in the section below.

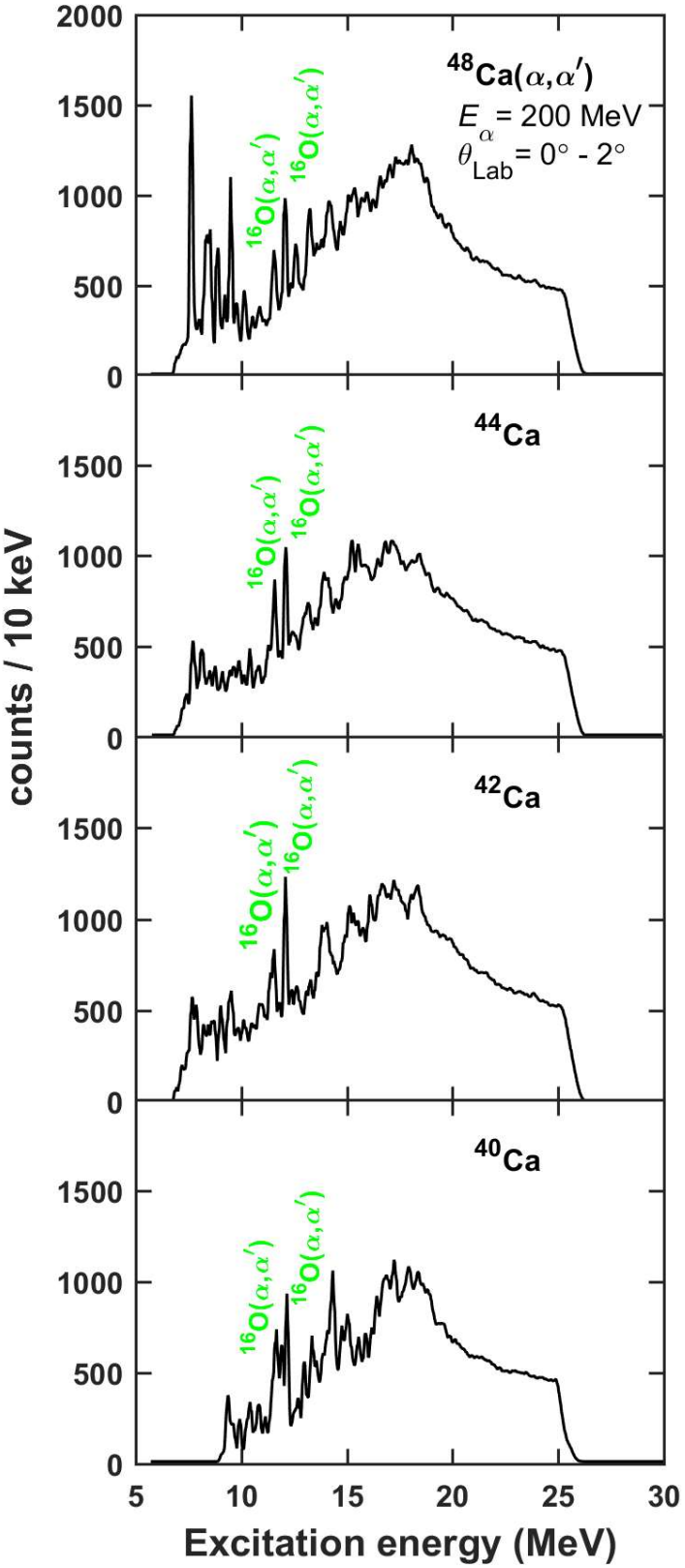


Figure 4.1: Measured excitation energy spectrum for the ^{40,42,44,48}Ca(α,α') at E_α = 200 MeV and $\theta_{\rm Lab} = 0°$ showing the ^{16}O contaminant peaks.

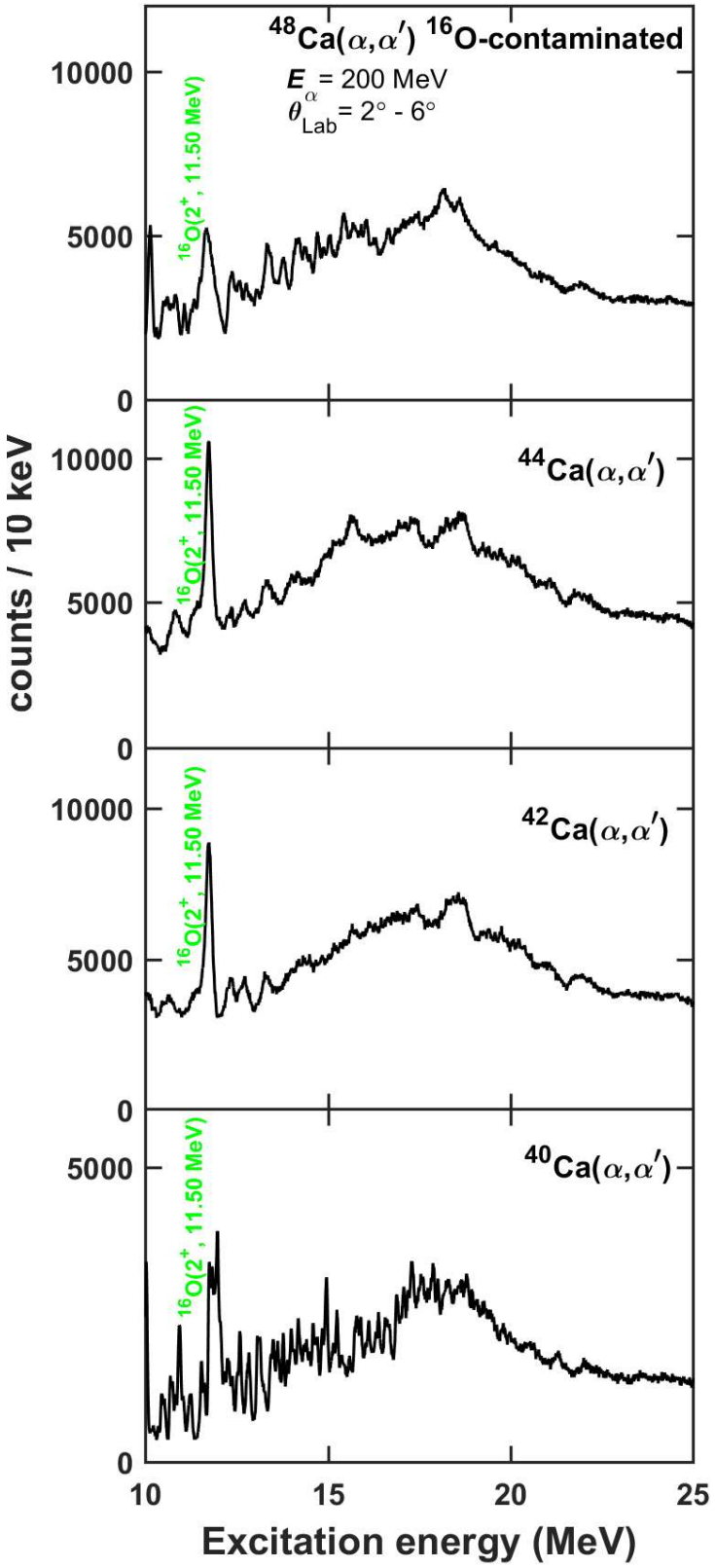


Figure 4.2: Measured excitation energy spectrum for the ^{40,42,44,48}Ca(α,α') at E_α = 200 MeV and $\theta_{\rm Lab}$ = 4° showing the ^{16}O contaminant peaks.

4.1.1 Experimental ^{40,42,44,48}Ca cross-sections after removal of ^{16}O contamination

Calcium is an element which oxidizes easily in air (see Section 3.3). As such, discrete peaks from ^{16}O(α,α') can be identified in the measured ^{40,42,44,48}Ca spectra, as shown in Fig. 4.1 for the 0° data. These peaks sit at the lower energy side of the excitation energy spectra and the ^{16}O background extends underneath the ISGMR region as a broad continuum. It was, therefore, necessary to obtain a good ^{16}O(α,α') spectrum for a satisfactory background subtraction from the Ca spectra. To this end, mylar $C_{10}H_8O_4$(α,α') and ^{12}C(α,α') measurements were taken also at 0° and 4°. By way of example for ^{48}Ca, Fig. 4.3(a) shows mylar and ^{12}C spectra with the identified states. A direct background subtraction approach was used to remove the ^{12}C spectrum from the mylar. The spectrum from the ^{12}C target was normalised to the strength of the ^{12}C 9.641 MeV peak in the mylar spectrum as in Fig. 4.3(a). The mylar spectrum with the normalised ^{12}C removed is shown in Fig. 4.3(b) which can be taken as the ^{16}O(α,α') spectrum. Similarly, the obtained ^{16}O(α,α') spectrum was normalised to the strength of the ^{16}O 12.049 MeV peak in the calcium isotopes spectra. Figure 4.3(c) shows the normalised ^{16}O spectrum superimposed on the ^{48}Ca spectrum. Again, using the direct background subtraction method, the normalised ^{16}O spectrum was removed from each of the Ca isotopes spectra. It should be noted that all the ^{16}O peaks in the region of the GMR have widths that are naturally much higher than the 12.049 MeV peak resulting in a continuum-like relatively small background in the region of the calcium ISGMR. The excitation-energy spectra for the various calcium isotopes, before and after the ^{16}O spectrum subtraction, are presented in Fig. 4.4. Following which the double-differential cross sections were evaluated from the oxygen-free spectra of all four calcium isotopes using Eq. (3.7) and are shown in Fig. 4.5 for the 0° data.

The same process was repeated for the 4° data but the obtained ^{16}O(α,α') spectrum at 4° was normalised to the strength of the ^{16}O 11.50 MeV peak in the calcium isotopes spectra. The results are shown in Figs. 4.6, 4.7 and 4.8 for the 4° data.

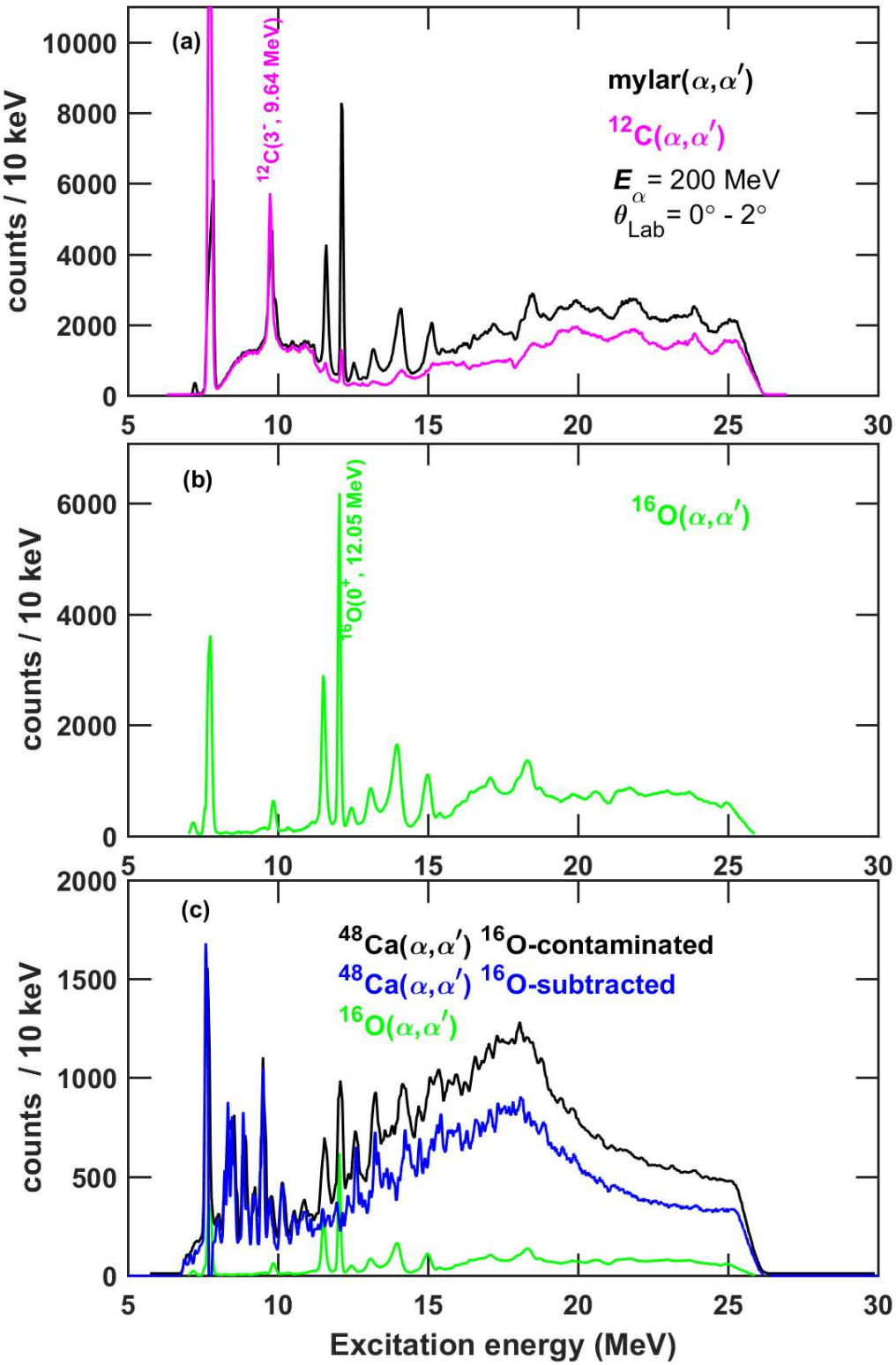


Figure 4.3: Panel (a): Mylar spectrum (black) with superimposed ^{12}C spectrum (magenta). Panel (b): Extracted ^{16}O spectrum. Panel (b): Spectra of oxygen-contaminated ^{48}Ca (black), extracted ^{16}O (green) and oxygen-free ^{48}Ca (blue).

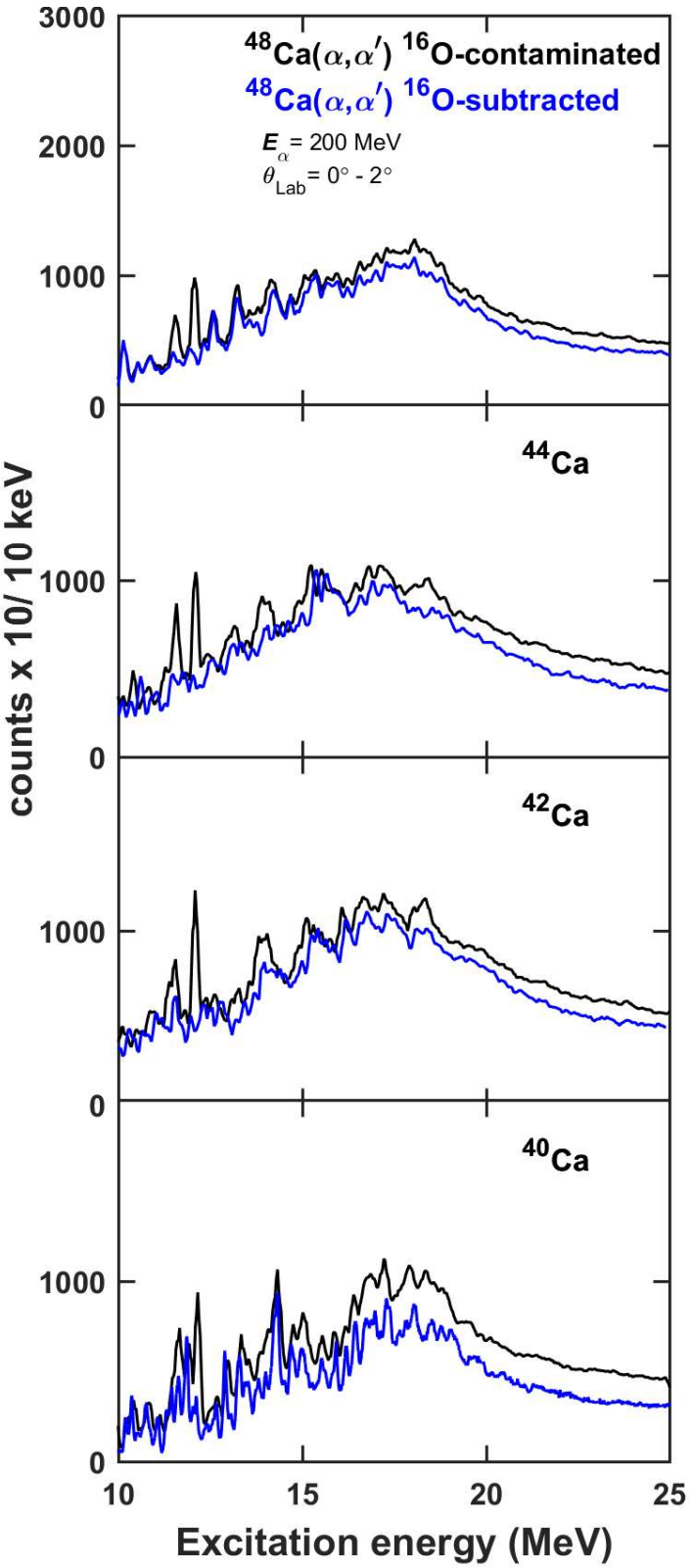


Figure 4.4: Superposition of experimental oxygen-contaminated and oxygen-subtracted excitation energy spectra for ^{48,44,42,40}Ca(α,α') at E_α = 200 MeV and θ_{Lab} = 0° - 2°.

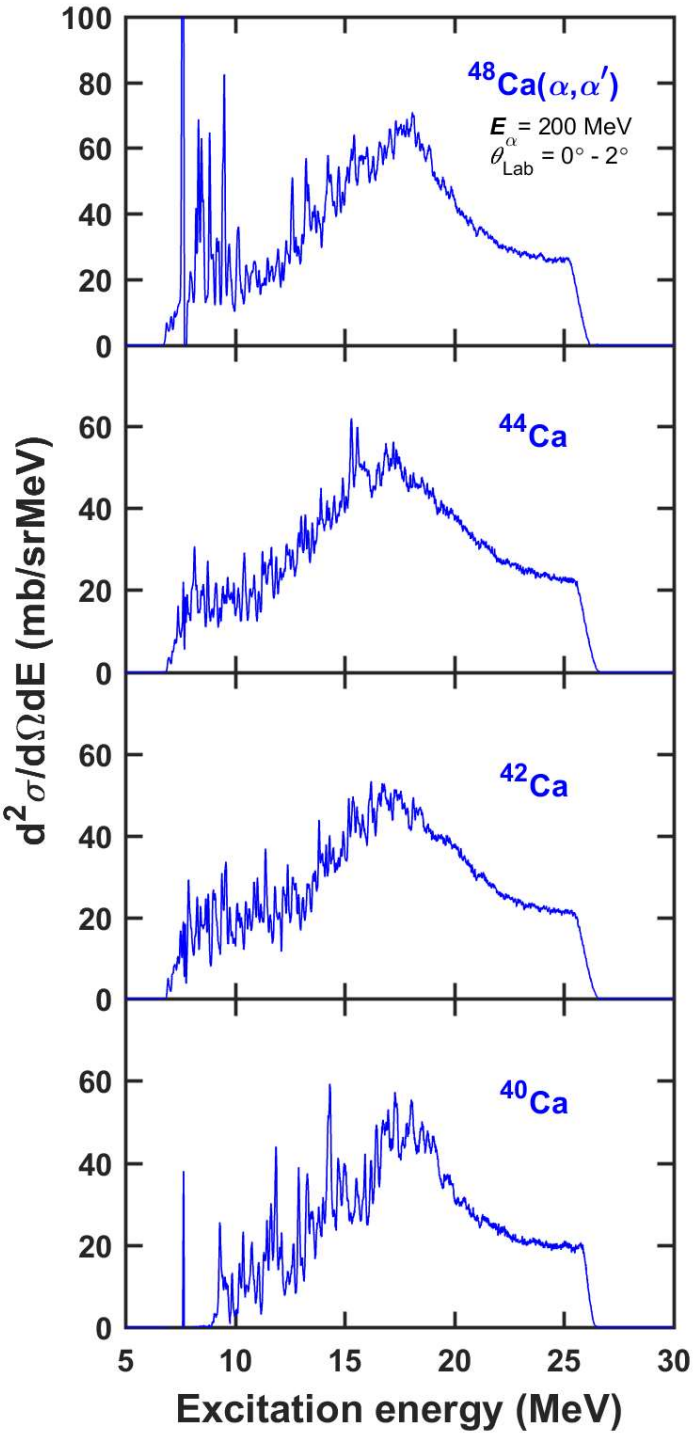


Figure 4.5: Double-differential cross sections obtained from oxygen-free spectra of ^{48,44,42,40}Ca.

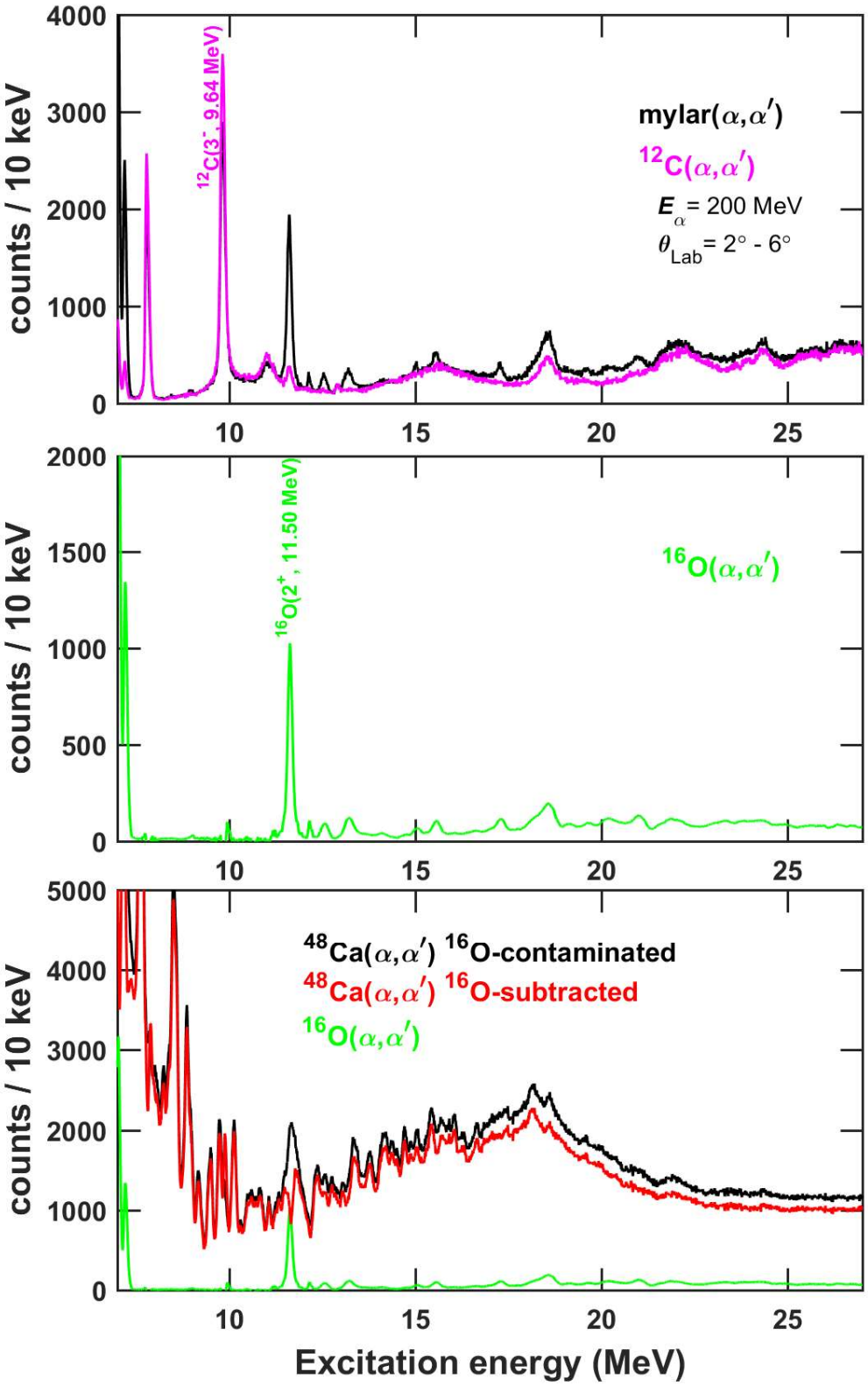


Figure 4.6: Panel (a): Mylar spectrum (black) with superimposed ^{12}C spectrum (magenta). Panel (b): Extracted ^{16}O spectrum. Panel (b): Spectra of oxygen-contaminated ^{48}Ca (black), extracted ^{16}O (green) and oxygen-free ^{48}Ca (red)

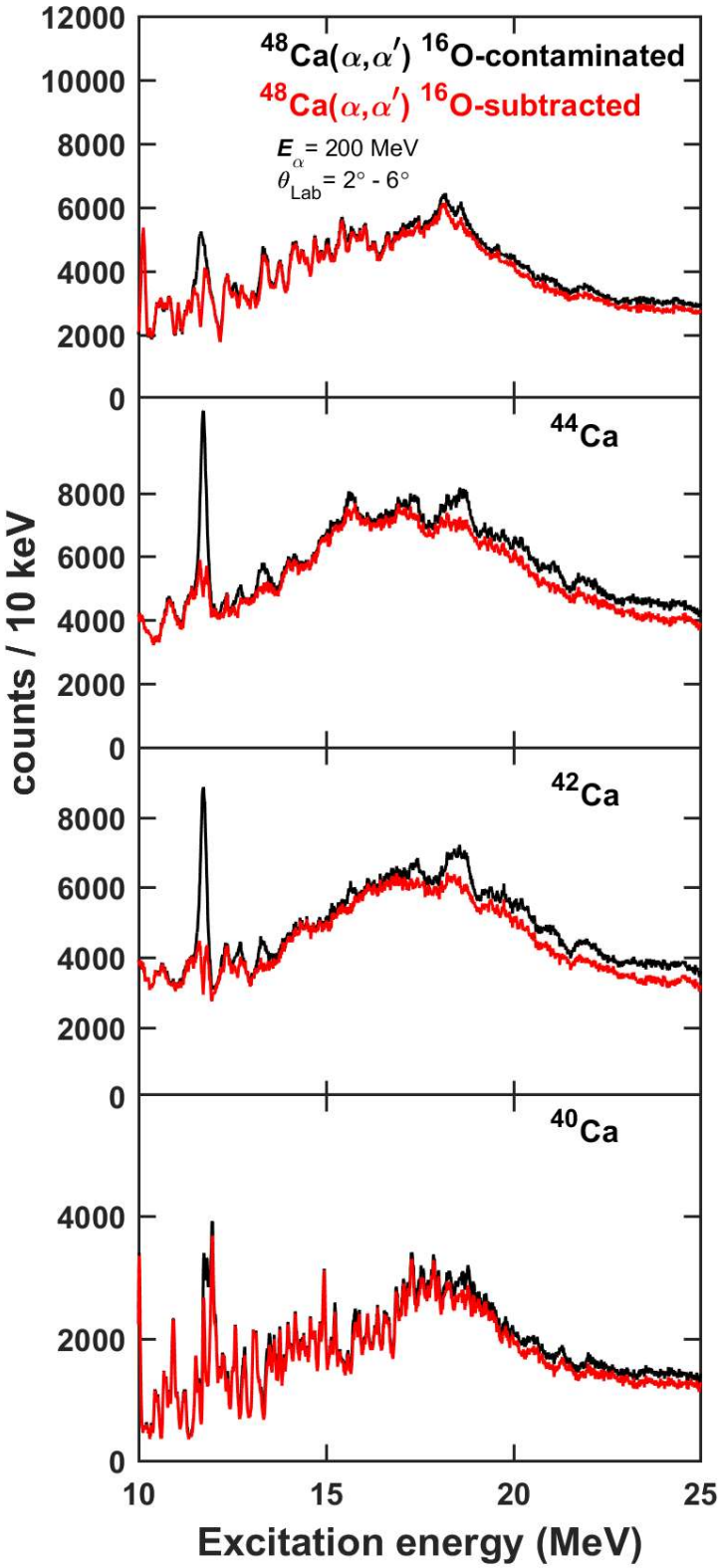


Figure 4.7: Superposition of experimental oxygen-contaminated and oxygen-subtracted excitation energy spectra for ^{48,44,42,40}Ca(α,α') at E_α = 200 MeV and $\theta_{\mathrm{Lab}} = 4°$.

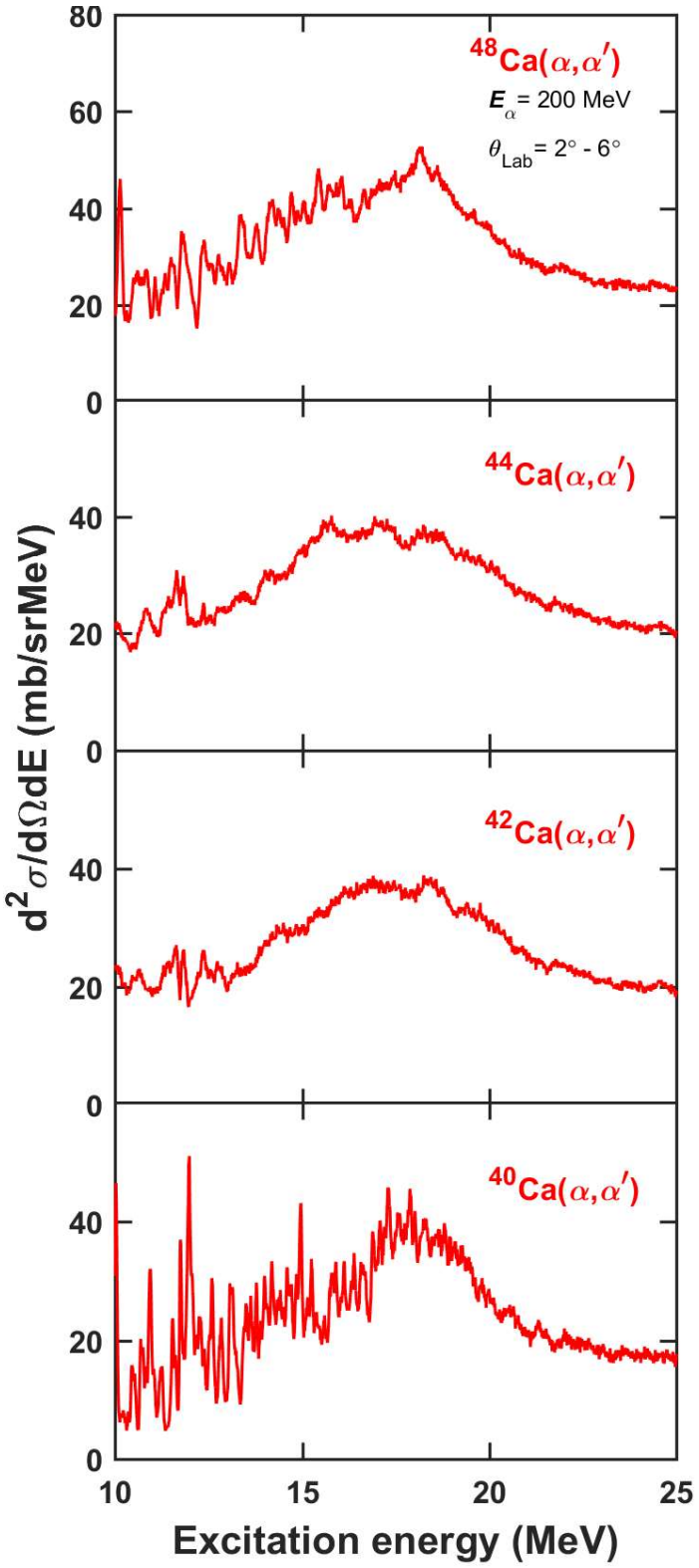


Figure 4.8: Double-differential cross sections obtained from oxygen-free spectra of ^{48,44,42,40}Ca at $\theta_{\mathrm{Lab}} = 4°$.

4.2 Extraction of $E0$ strength for ^{40,42,44,48}Ca

Typically, the Multipole Decomposition Analysis (MDA) technique is applied to (α,α') experimental data in order to extract the $E0$ strength. This requires a measured angular distribution $0^\circ \leq \theta_{\rm Lab} \lesssim 10^\circ$ in steps of about 0.5° for incident energies in the range $150 \lesssim E_\alpha \lesssim 400$ MeV on targets across the periodic table. A magnetic spectrometer is used capable of measuring at zero-degrees scattering angle, generally with an angular acceptance $\theta_{\rm Lab} = 0^\circ$- 2° and with good angle discrimination within this angular range (see, for example, TAMU Refs. [You97, Lui11, But17] and RCNP Refs. [Gup16, How20]). In the present project, the Zero-degree Facility of the K600 magnetic spectrometer of iThemba LABS was used which, due to ion-optics limitations, does not have scattering angle sensitivity in the range $0^\circ \leq \theta_{\rm Lab} \leq 2^\circ$. Therefore, a measured zero degree cross-section is the average within the 2° angular acceptance.

In order to apply the Difference of Spectra (DoS) technique for determination of $E0$ strength for ^{40,42,44,48}Ca(α,α') at E_α= 200 MeV, the angle cut from the measurement at $\theta_{\rm Lab} = 4^\circ \pm 2^\circ$ is determined from DWBA calculations, see Section 4.2.1. Following which the DoS technique is applied as detailed in Section 4.2.2 to determine the $E0$ strength in the region of the ISGMR for the various calcium isotopes. Finally, in Section 4.2.3, centroids and widths are determined for the ISGMR from the corresponding strength functions for the various calcium isotopes.

4.2.1 DWBA multipole calculations

There are a number of references to the use of Multipole Decomposition Analysis (MDA) for the extraction of $E0$ strength from calcium isotopes (see, for example, [You97, Lui11, But17, How20]). However, the most useful and detailed closest to the present work is that of Lui *et al.* [Lui11] for ^{48}Ca. Using this reference as a starting point, the results of the DWBA calculations for ^{48}Ca(α, α') at $E_\alpha = 240$ MeV and $E_{\rm x} = 16.23$ MeV excitation energy are shown in the upper panel of Fig. 4.9. This was achieved by varying the spectroscopic factors for each multipole in order to reproduce the multipole fit line through the measured data points of Lui *et al.* [Lui11], as shown in the left topmost panel of Fig. 4 in [Lui11]. Using the same spectroscopic factors, angular distributions were calculated for ^{48}Ca(α, α') at $E_\alpha = 200$

MeV and $E_{\rm x}$ = 16.23 MeV and the results are shown in the lower panel of Fig. 4.9. Here, the $L = 0$ multipole exhibits a very sharp minimum at $\theta_{\rm c.m.} \approx$ 3.5° and is used to determine the scattering-angle cut region for the 4° data used in the DoS method in the following section. Similar DWBA calculations were performed for other calcium isotopes ^{40,42,44}Ca(α,α') using the parameters given in Table 4.1. The shape of the various multipole components remains the same for all the calcium isotopes. In addition, when taking into account variations in the centroid of the ISGMR by varying the excitation energy $E_{\rm x}$ over a small energy range of a few MeV for the DWBA calculations, very little difference is seen in the multipole distributions.

In this study, the computer code PTOLEMY [Rho80] was used for the DWBA calculations, with the hybrid optical model of the form:

$$U(r) = V_{\rm F}(r) + i\frac{W}{1+\exp(\frac{r-R_{\rm i}}{a_{\rm i}})}, \tag{4.1}$$

where W is the depth of the Woods-Saxon type imaginary part of the potential, with the reduced radius $R_{\rm i}$ and diffuseness $a_{\rm i}$. $V_{\rm F}(r)$ is the real single-folding potential:

$$V_{\rm F}(r) = V\int d^3r'\rho(r')[1-\beta\rho(r')^{2/3}]\exp(-s^2/t^2). \tag{4.2}$$

Here, V is the depth of the real part of the potential, $s = |r-r'|$ is the distance between the center of mass of the alpha particle and a target nucleon, and $\rho(r')$ is the ground-state density of the target nucleus. The parameters β = 1.9 fm^2 and t = 1.88 fm were adopted from [Sat97]. Also, calculations were performed with the Fermi form for the mass distribution [Sat87]

$$\rho(r) = \frac{\rho_0}{1+\exp(\frac{r-c}{a})}, \tag{4.3}$$

where a and c are from [Fri95] and are shown in Table 4.1.

Table 4.1: Optical-model and Fermi distribution parameters [You97, Lui11] used in DWBA calculations. Note: a and c are from [Fri95].

Nucleus	V (MeV)	W (MeV)	R_{i} (fm)	a_{i} (fm)	c (fm)	a (fm)
^{40}Ca	24.700	23.800	4.852	0.755	3.654	0.550
^{42}Ca	47.392	31.495	4.907	0.677	3.769	0.523
^{44}Ca	47.392	31.495	4.907	0.677	3.784	0.523
^{48}Ca	47.392	31.495	4.907	0.677	3.723	0.523

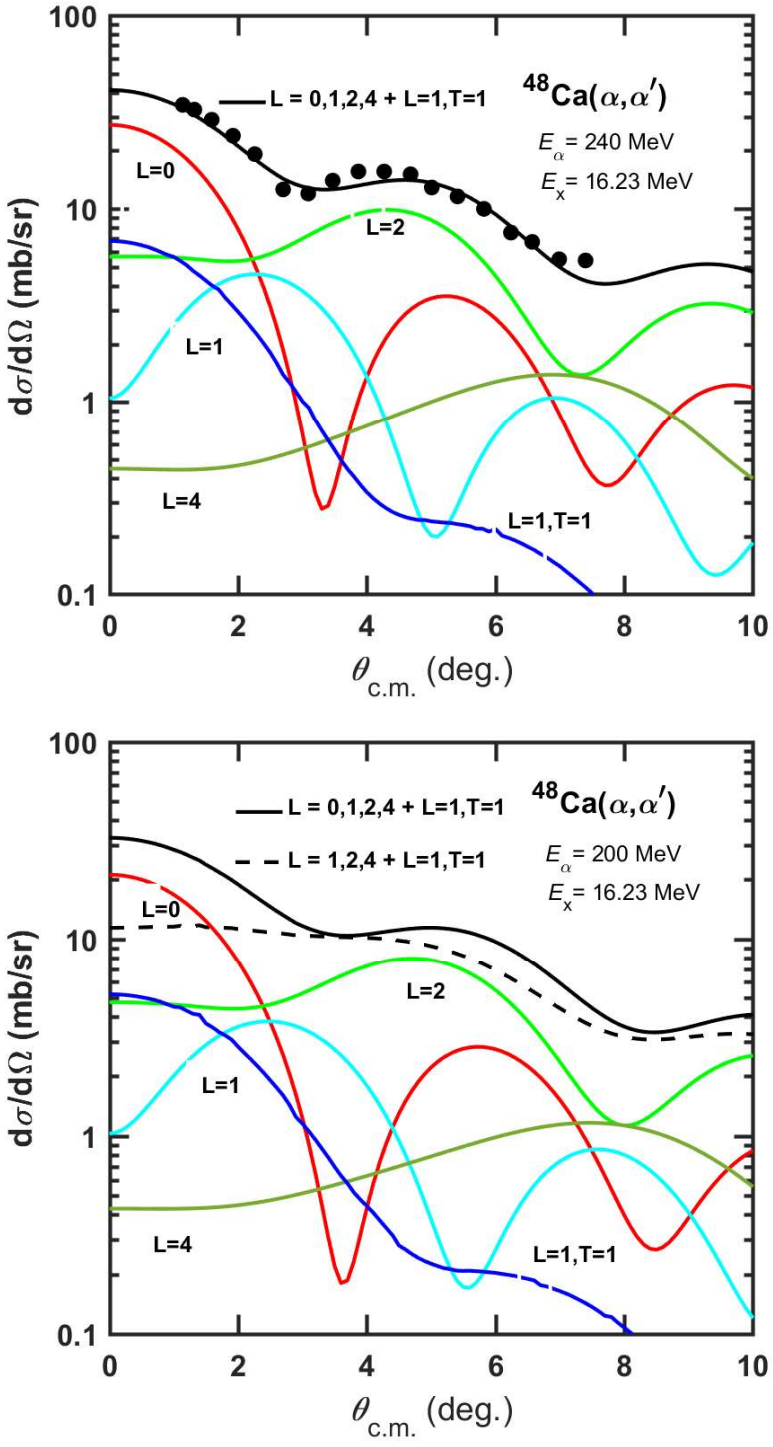


Figure 4.9: Angular distributions of the differential cross-sections for inelastic alpha particle scattering on ^{48}Ca at E_{x} = 16.23 MeV and at E_{α} = 240 MeV (upper panel) and E_{α} = 200 MeV (lower panel) for L = 0, 1, 2, 4 and L = 1, T = 1. The black dashed line represent the sum of L = 1, 2, 4 and L = 1, T = 1, while the solid black line represents the sum of all the multipoles shown. Note that the data shown in the upper panel are from Lui *et al.* [Lui11].

4.2.2 Difference-of-Spectra (DoS) technique

The Difference of Spectra (DoS) technique is used to extract $E0$ strength from medium energy (α,α') experiments at and near 0° scattering angles using a magnetic spectrometer, the excitation energy region covered for the target nucleus is generally in the range $8 \lesssim E_{\mathrm{x}} \lesssim 40$ MeV with the ISGMR lying at the lower end of the range and additional $E0$ strength above the ISGMR. The Fraction $E0$ EWSR and $E0$ strength distributions extracted are referenced to the $E0$ strength at a scattering angle of 0°.

The rationale behind the DoS technique is that the angular distribution of the $L = 0$ (ISGMR) has a maximum at $\theta_{\mathrm{c.m.}} = 0°$ and a nearby first minimum, which for the case of ^{48}Ca is at $\theta_{\mathrm{c.m.}} \approx 3.5°$, as shown in Fig. 4.9. The sum of angular distributions of other multipoles, especially the $L = 2$ (ISGQR), represented by the dashed black line in Fig. 4.9, is almost flat within the range $0° \leq \theta_{\mathrm{c.m.}} \leq 4.5°$. Therefore, the subtraction of the inelastic scattering spectrum at the first minimum of the $L = 0$ angular distribution from that at $\theta_{\mathrm{c.m.}} = 0°$ is essentially $E0$ strength (ISGMR and above) [Bra83, You97, Gup16, Gar18]. This resulting spectrum is called the "difference spectrum".

In this study, the difference spectrum for each of the calcium isotopes considered was obtained by subtracting the spectrum for the angle cut at $2.76° \leq \theta_{\mathrm{Lab}} \leq 4.31°$ (or $3.0° \leq \theta_{\mathrm{c.m.}} \leq 4.5°$) from the spectrum at $0° \leq \theta_{\mathrm{Lab}} \leq 2°$. These are shown in Figs. 4.10, 4.11, 4.12 and 4.13 for ^{48}Ca, ^{44}Ca, ^{42}Ca and ^{40}Ca, respectively. Here, the blue spectrum is for $0° \leq \theta_{\mathrm{Lab}} \leq 2°$ (see Fig. 4.5), the red is for $2.76° \leq \theta_{\mathrm{Lab}} \leq 4.31°$ and the black, which is the difference spectrum, is the difference between the blue and the red spectra. However, before the subtraction, the spectra for $0° \leq \theta_{\mathrm{Lab}} \leq 2°$ were scaled up by certain factors (1.32, 1.45, 1.33 and 1.35 for ^{48}Ca, ^{44}Ca, ^{42}Ca and ^{40}Ca, respectively) in order to make the cross-sections equivalent to those that would be measured at $\theta_{\mathrm{Lab}} = 0°$. Scaling up factors vary within a range of 9% and can be attributed to uncertainty in the normalisation of absolute cross-sections between 0° and 4° data across all four calcium isotopes measured. Scaling-up factors of the measured $\theta_{\mathrm{Lab}} = 0°$ - 2° energy spectra to determine the equivalent 0° spectra were obtained by rebinning to 1 MeV the $\theta_{\mathrm{Lab}} = 0°$ - 2° and the 4° angle cut spectra to smooth out the peak structure near $E_{\mathrm{x}} = 10$ MeV where $E0$ cross-section falls to low values. Any negative cross-section produced after subtraction due to mismatch between

the 0° and the 4° angle cut discrete peaks due to energy calibration were then set to zero.

These scaling-up factors are also consistent with

1) that for $E_\alpha = 200$ MeV the average cross-section in the angle range $0° \leq \theta_{\text{c.m.}} \leq 2.2°$ ($0° \leq \theta_{\text{Lab}} \leq 2°$) from the sum of multipoles in the lower panel of Fig. 4.9 is 25.3 mb/sr which when scaled up by a factor 1.32 gives a value of 33.2 mb/sr, the cross section at $\theta_{\text{c.m.}} = 0°$, and

2) that the resulting difference spectra have $E0$ cross-sections averaging zero close to and just below $E_{\text{x}} = 10$ MeV and then steadily increase above $E_{\text{x}} = 10$ MeV which is consistent with previous measurements for ^{48}Ca [Lui11], ^{44}Ca [But17] and ^{40}Ca [You97].

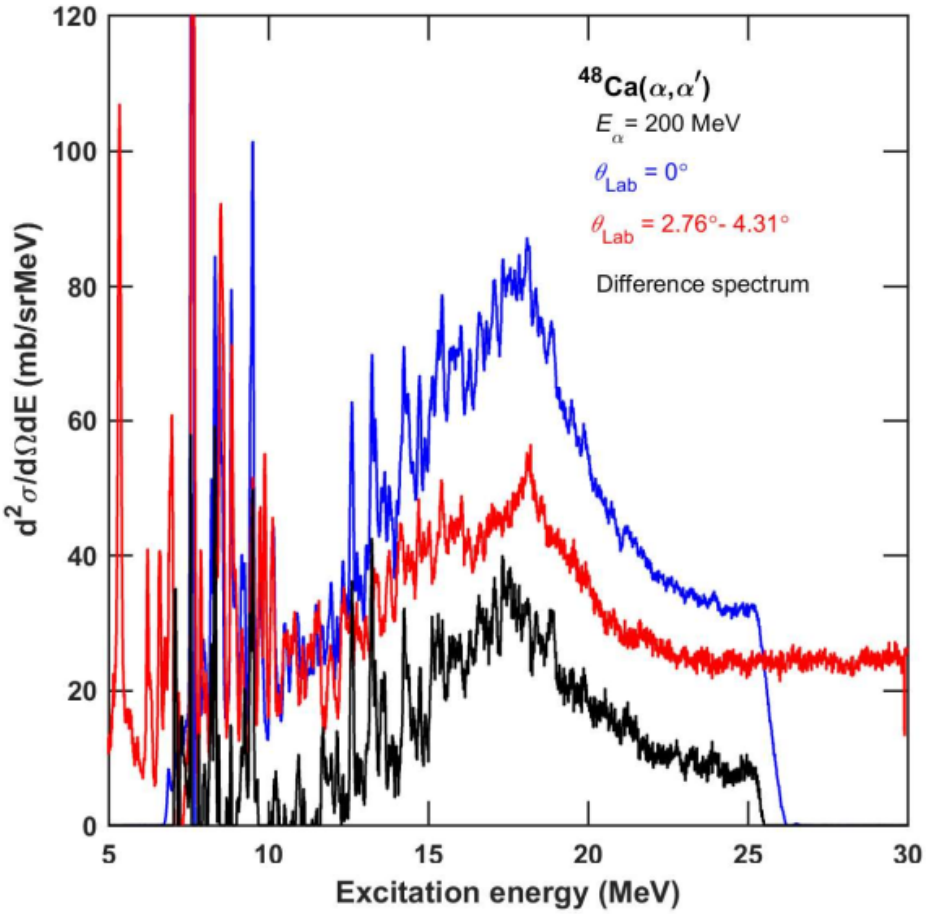


Figure 4.10: Double-differential cross section for ^{48}Ca(α, α') at $E_\alpha = 200$ MeV. The blue spectrum is for $0° \leq \theta_{\text{Lab}} \leq 2°$ (see Fig. 4.5), the red is for $2.76° \leq \theta_{\text{Lab}} \leq 4.31°$ (which correspond to $3° \leq \theta_{\text{c.m.}} \leq 4.5°$, see angle region shown in Fig. 4.9 and is cut from the ^{48}Ca spectrum shown in Fig. 4.8) and the black is the difference spectrum obtained by subtracting the $2.76° - 4.31°$ spectrum (red) from the $0°$ spectrum (blue). Note that the $0° - 2°$ spectrum was scaled by a factor of 1.32 in order to make the cross-section equivalent to that which would be measured at $\theta_{\text{Lab}} = 0°$.

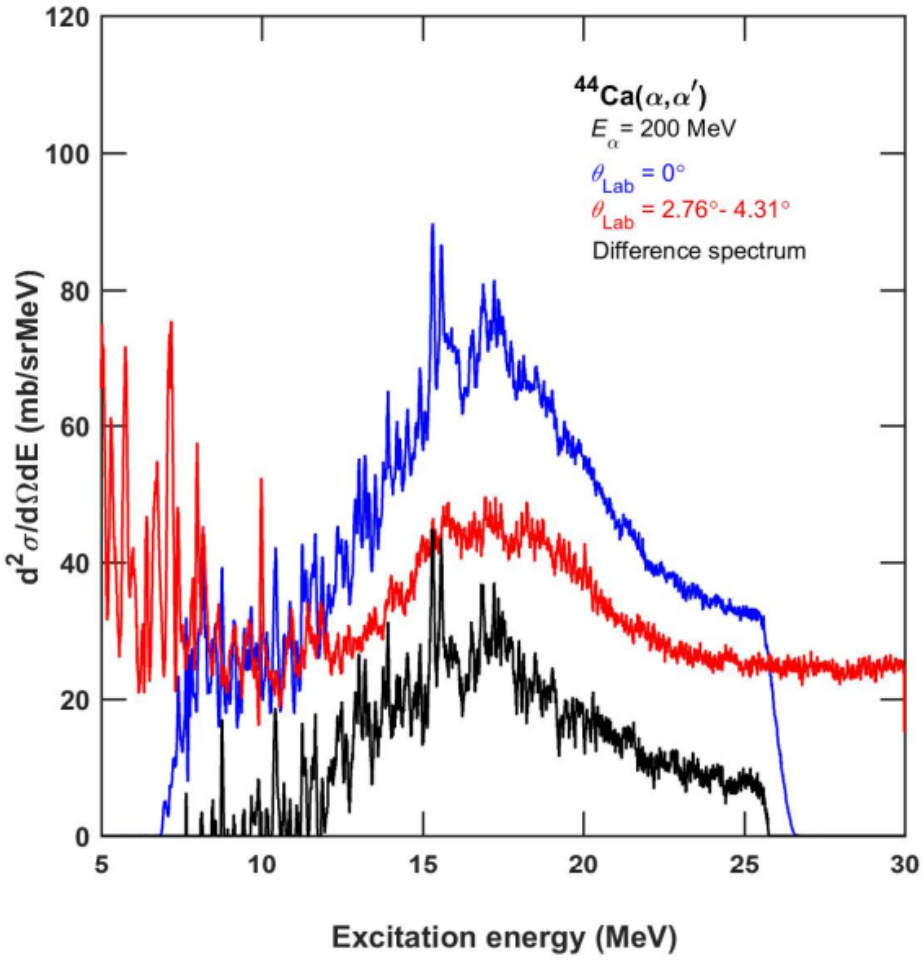


Figure 4.11: Same as Fig. 4.10 but for ^{44}Ca(α,α'). The $0° - 2°$ spectrum was scaled by a factor of 1.45.

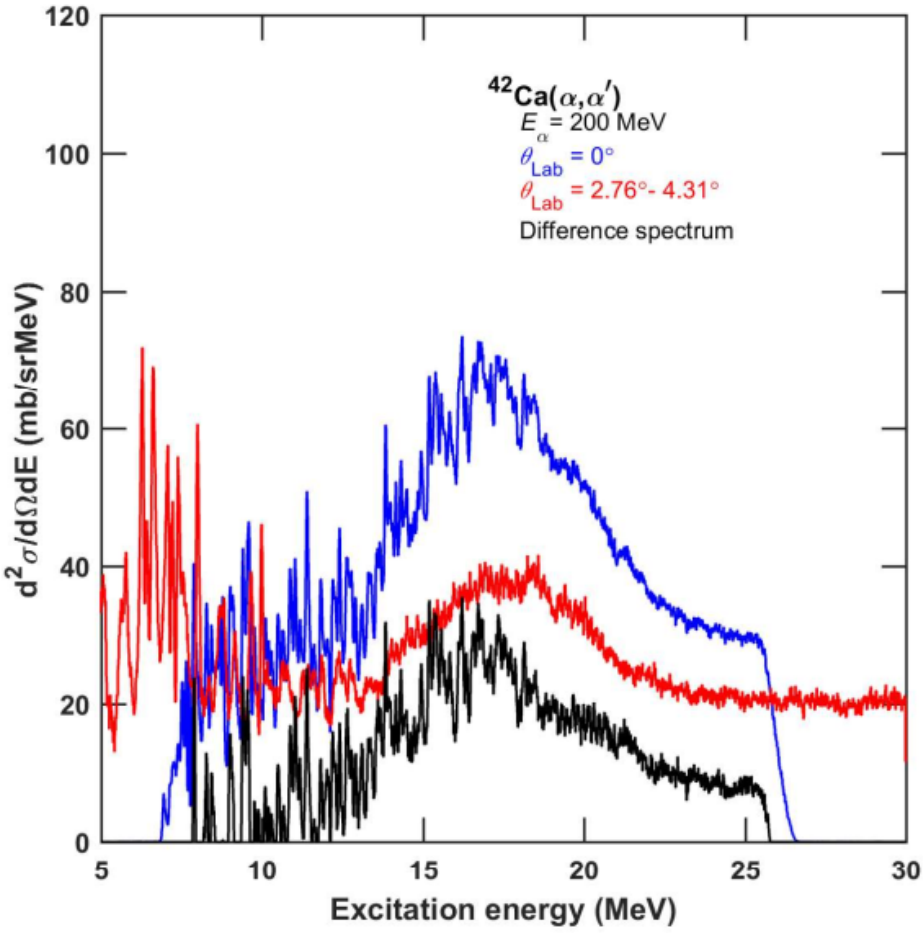


Figure 4.12: Same as Fig. 4.10 but for ^{42}Ca(α,α'). The $0° - 2°$ spectrum was scaled by a factor of 1.33.

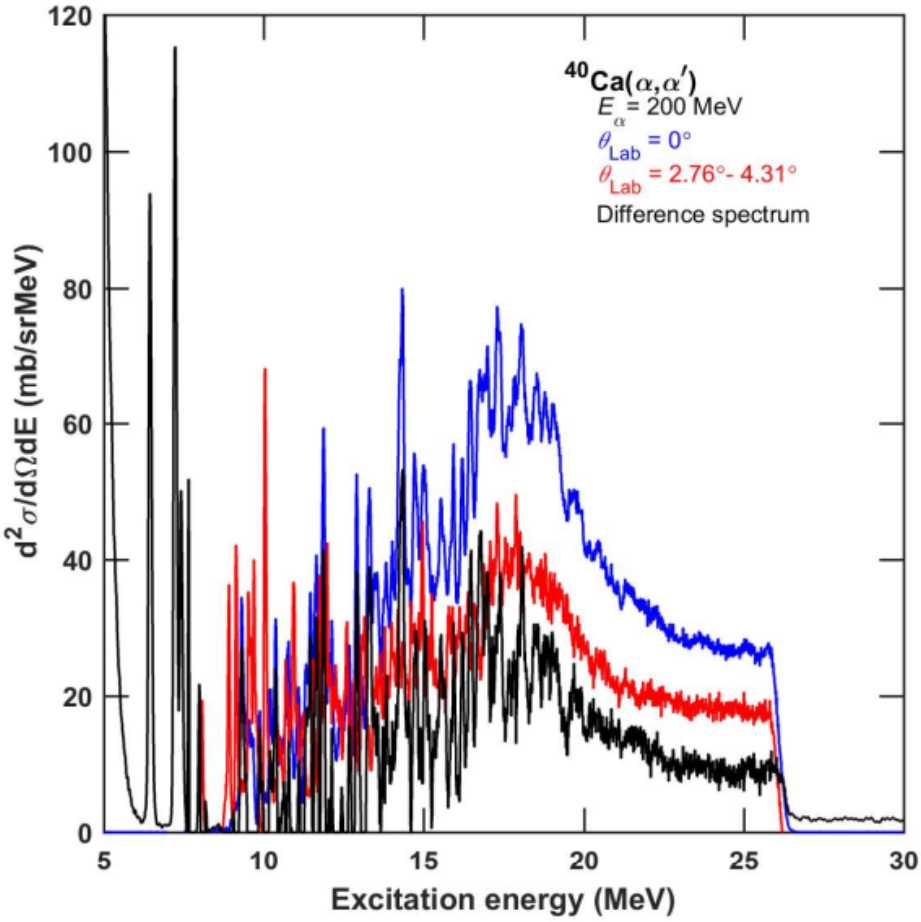


Figure 4.13: Same as Fig. 4.10 but for ^{40}Ca(α,α'). The $0^\circ - 2^\circ$ spectrum was scaled by a factor of 1.35.

4.2.3 Determination of the Fraction $E0$ EWSR and the $E0$ strength distributions

A step-by-step analysis of how the Fraction $E0$ EWSR and $E0$ strength distribution are obtained from the difference spectrum is given below.

Using ^{48}Ca as the detailed example:

1) **Figure 4.14(a)** This double-differential cross section spectrum is obtained using the DoS technique as shown in Fig. 4.10.

2) **Figure 4.14(b)** The spectrum in Fig. 4.14(a) is rebinned from 10 keV to 750 keV to allow for comparison with Texas AMU (TAMU) results at $E_\alpha = 240$ MeV and RCNP results at $E_\alpha = 386$ MeV.

3) **Figure 4.14(c)** The spectrum in Fig. 4.14(b) is converted from the laboratory to the centre-of-mass frame (factor 0.841 [Cat05]). This represents the actual equivalent cross section at $\theta_{\text{c.m.}} = 0°$.

4) **Figure 4.14(d)** Shows the $L = 0$ DWBA cross-section at $\theta_{\text{c.m.}} = 0°$ for 100% of the EWSR as a function of excitation energy E_x calculated using PTOLEMY [Rho80] and the parameters in Table 4.1.

5) **Figure 4.14(e)** Shows the Fraction $E0$ EWSR/MeV (see Eq. (2.41)) obtained by dividing the extracted $E0$ component at $\theta_{\text{c.m.}} = 0°$ of Fig. 4.14(c) by the corresponding $L = 0$ 100% EWSR at $\theta_{\text{c.m.}} = 0°$ of Fig. 4.14(d). Also shown for comparison purposes are the TAMU and RCNP results in the region of the ISGMR. This is just for comparison purposes as the error bars are not indicated.

6) **Figure 4.14(f)** Here, Fig. 4.14(e) is re-plotted up to $E_\text{x} = 40$ MeV to show the full extent of the TAMU and RCNP results for comparison purposes.

7) **Figure 4.14(g)** Here, the Fractional $E0$ EWSR/MeV as shown in Fig. 4.14(e) was converted to $E0$ strength using Eq. (2.41) and the corresponding parameters of Table 4.2. Also shown are TAMU and

RCNP results for comparison purposes.

8) **Figure 4.14(h)** Here, Fig. 4.14(g) is re-plotted up to $E_x = 40$ MeV to show the full extent of the TAMU and RCNP results for comparison purposes.

The steps above were repeated for ^{44}Ca, ^{42}Ca and ^{40}Ca and the results are shown in Figs. 4.15, 4.16 and 4.17, respectively. In these cases, a rebinning from the measured 10 keV bin size to 250 keV bin size was necessary for comparison with TAMU and RCNP results. Note that there are no data from TAMU for ^{42}Ca.

Table 4.2: Moments of the ground state density for ^{40,42,44,48}Ca, taken from [Fri95].

Nucleus	A	$\sqrt{\langle r^2 \rangle}$ (fm)
^{40}Ca	40	3.478
^{42}Ca	42	3.508
^{44}Ca	44	3.518
^{48}Ca	48	3.479

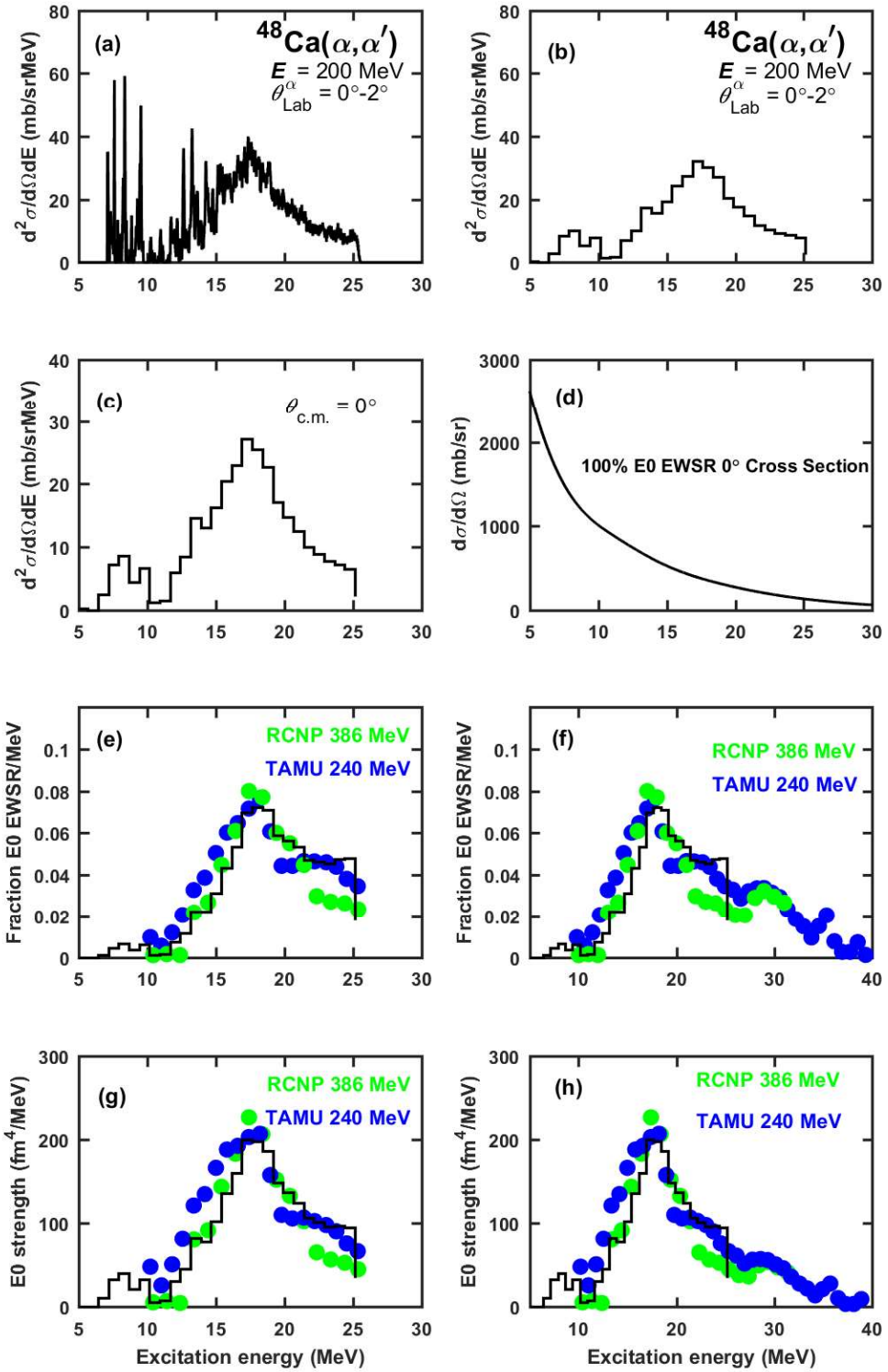


Figure 4.14: An outline of the conversion process from the double-differential cross section of ^{48}Ca(α, α') to fraction $E0$ EWSR per MeV and then to $E0$ strength distribution. See text for detailed explanation.

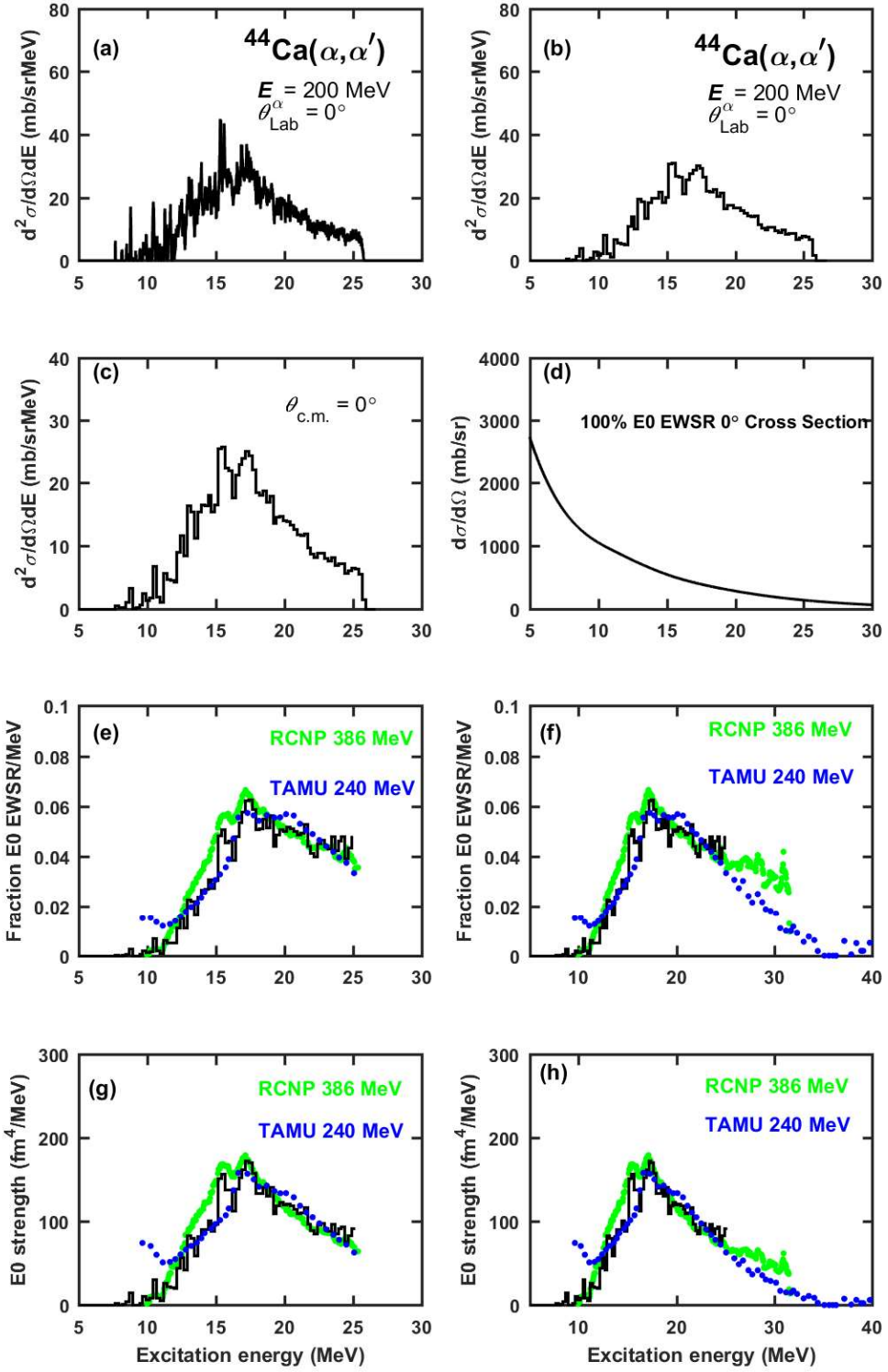


Figure 4.15: Same as Fig. 4.14 but for ^{44}Ca(α,α').

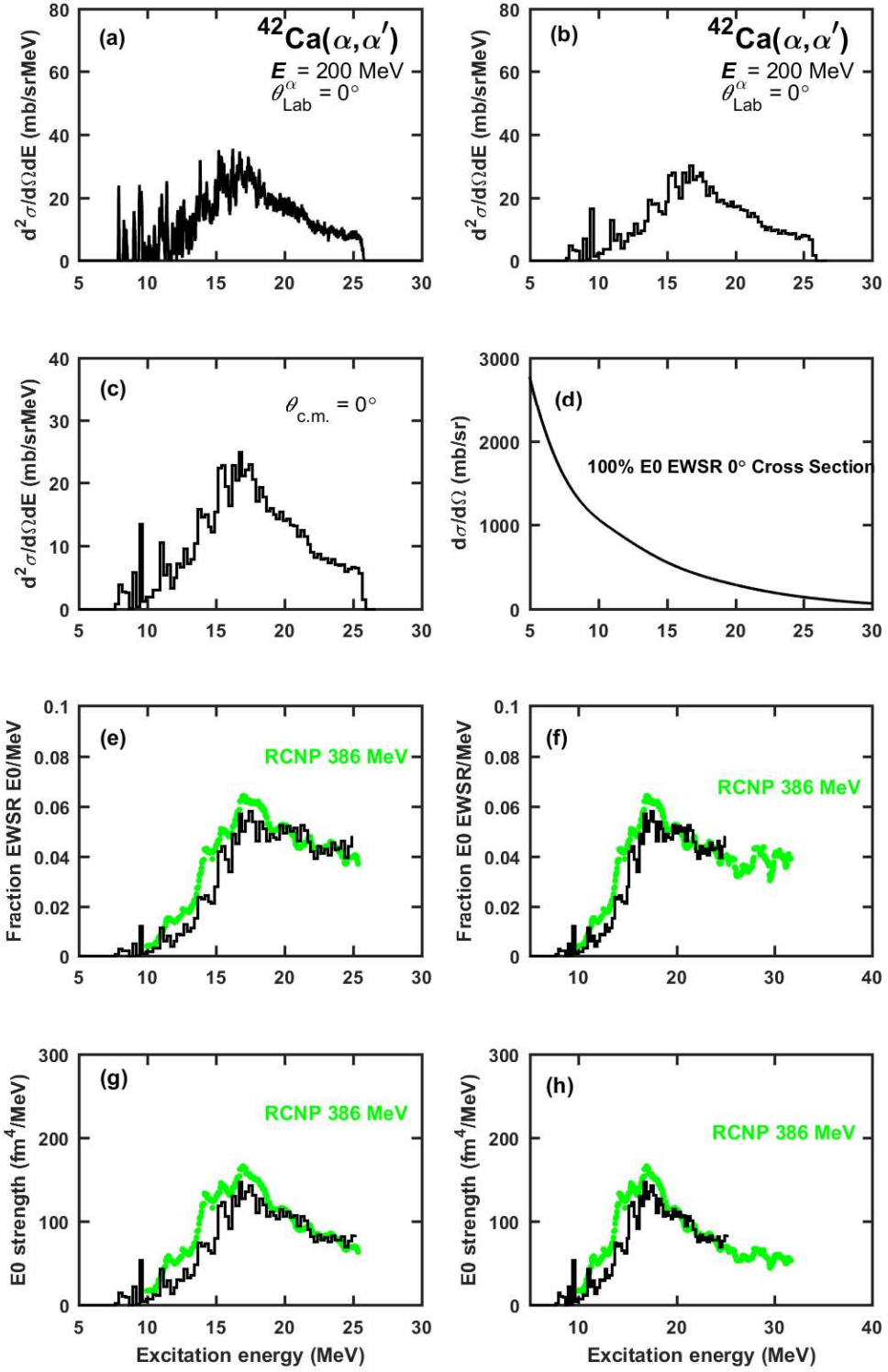


Figure 4.16: Same as Fig. 4.14 but for ^{42}Ca(α,α').

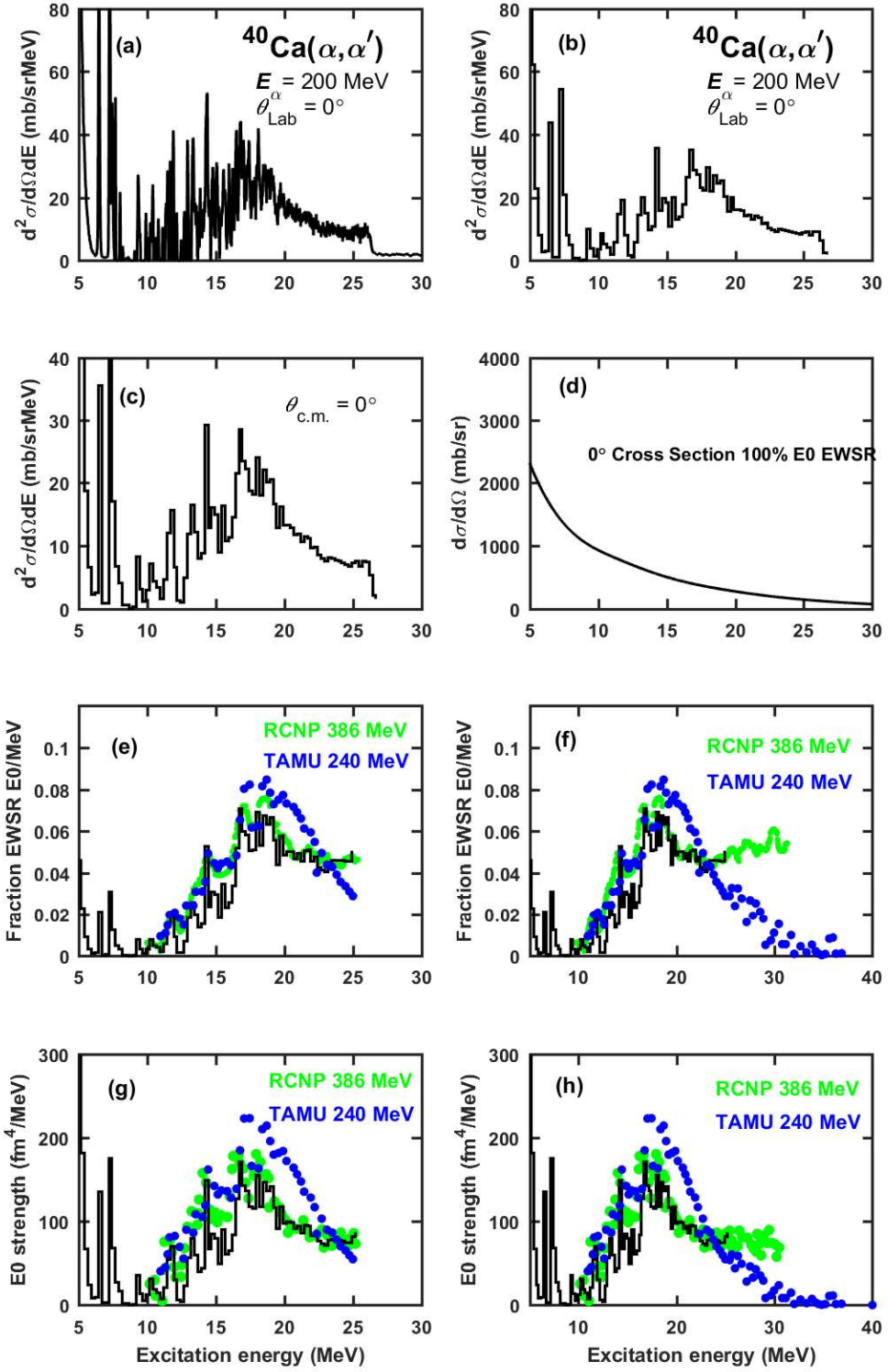


Figure 4.17: Same as Fig. 4.14 but for ^{40}Ca(α,α').

4.2.4 Discussion

It can be seen from Figs. 4.14(e) and (g) for ^{48}Ca that there is a reasonable agreement with peak positions and amplitudes up till about 22 MeV, but the RCNP data become lower between 22 and 25 MeV. The degree of agreement in the $E0$ strength observed in the three data sets with different experimental conditions, different beam energies and different techniques (i.e. MDA and DoS) raises the confidence that the observed structure is purely due to $E0$ strength in ^{48}Ca with little or no contributions from other multipoles.

Furthermore, the RCNP group also reported $E0$ strength distributions in ^{40,42,44}Ca from inelastic α scattering at 386 MeV [How20] using the MDA technique. Again, the present data on ^{40,42,44}Ca were also compared with theirs following the same approach mentioned above for ^{48}Ca. The comparison plots are presented in Figs. 4.15, 4.16 and 4.17 for ^{44}Ca, ^{42}Ca and ^{40}Ca, respectively. Panels (a), (b), (c), (d) and (e) in each of the figures show a step-by-step procedure of how the Fraction $E0$ EWSR and the $E0$ strength distributions are obtained from the difference spectra of each target. The procedure is exactly the same with that explained for ^{48}Ca above. Comparisons of the present data with that of RCNP are shown in panels (e) and (g) in Figs. 4.15, 4.15 and 4.17. It can be seen from these figures that for each target nucleus, within $10 \leq E_{\mathrm{x}} \leq 25$ MeV region, there is an excellent agreement between the two data sets both in peak positions and amplitudes. This also increases the confidence that the observed structure is purely due to $E0$ strength in ^{40,42,44}Ca with no significant contributions from other multipoles.

4.3 Discussion of ISGMR strength distributions in ^{40,42,44,48}Ca

An overview of the double-differential cross sections for the calcium isotope chain is provided in Section 4.3.1. Section 4.3.2 presents the comparison of the extracted ISGMR strength distributions with the theoretical $E0$ strength functions, which were calculated using the PPC, QTBA, QRPA, SRPA and RPA formalisms (see Section 2.2.1). Using the Continuous Wavelet Transform (CWT) technique, characteristic energy scales were extracted from both the experimental data and theoretical predictions, the results are compared and presented in Section 4.4.

4.3.1 Overview of ISGMR in ^{40,42,44,48}Ca

The Multipole Decomposition Analysis (MDA) technique has been used extensively over the last two decades or so to determine in particular, the isoscalar $L = 0$ ($E0$ strength distribution and the ISGMR) for (α, α') scattering on targets across the periodic table. This technique has also been used to extract, in addition, other isoscalar strength distributions and corresponding giant resonances $L = 1$ ($E1$ strength distribution), $L = 2$ ($E2$ strength distribution) and $L = 3$ ($E3$ strength distribution), the high-energy octupole (see for example Ref [Kri15]). In some cases "unexpected" results have been reported. Here, in particular, the ISGMR in the $A \approx 90$ region investigated by the TAMU group [You13] was reported to have "implication for nuclear compressibility" due to "unexpected characteristics of the isoscalar monopole resonance in the $A \approx 90$ region. However, later in 2016 an independent investigation by the RCNP group for ^{90,92}Zr, 92Mo(α, α') at E = 386 MeV [Gup16] using the Difference of Spectra (DoS) technique came to the conclusion that "The ISGMR strength distributions for the three nuclei coincide with each other, establishing clearly that nuclear compressibility is not influenced by nuclear shell structure". Retrospectively, it became clear that the MDA technique used by TAMU has a significant shortcoming with the use of a somewhat arbitrary subtraction of a "background" strictly from just below the maximum of the ISGMR (E_x = 10 MeV) up to the maximum of the excitation energy region measured ($E_x \lesssim 40$ MeV).

In the present project, the measured scattering data for ^{40,42,44,48}Ca(α, α') at E_α = 200 MeV were analysed using the DoS technique. The underlying background from all other multipoles (except $L = 0$) using an angle cut from the measured 4° data (where the $L = 0$ contribution is reduced to a negligible amount) is subtracted from the measured $\theta_{\rm Lab}$ = 0° - 2° data converted to the equivalent $\theta_{\rm Lab} = 0°$ spectrum. Thus, the use of an arbitrary background subtraction is avoided. The extraction $E0$ cross-section for the measured calcium isotopes chain are shown together in Fig. 4.18. Here, it can be seen that the doubly-magic ^{40}Ca and ^{48}Ca have maxima in cross-section of $\sim$ 40 mb/srMeV at around $E_{\rm x} \approx 17$ MeV but in comparison ^{40}Ca exhibits a lot more fine structure from below to above the maximum of the ISGMR than does ^{48}Ca. In contrast, the singly magic ^{42}Ca and ^{44}Ca have much reduced maxima at just over $\sim$ 20 mb/srMeV in comparison to ^{40}Ca and ^{48}Ca. Also, the ^{42}Ca and ^{44}Ca exhibit a reduced amount of fine structure in comparison to ^{40}Ca and ^{48}Ca.

Table 4.3: Extracted values of centroids and widths of the ISGMR using Lorentzian fits.

Nucleus	Centroid (MeV)	Width (MeV)
^{48}Ca	17.9 ±0.1	5.8 ±0.2
^{44}Ca	17.2 ±0.1	6.0 ±0.2
^{42}Ca	17.3 ±0.1	6.0 ±0.2
^{40}Ca	18.0 ±0.1	6.7 ±0.3

It should be noted that as target mass increases from the present $40 \leq A \leq 48$ range fine structure below the maximum of the ISGMR decreases, the ISGMR becomes narrower and maximum of the ISGMR steadily decreases with an $A^{-1/3}$ dependence. On the other hand, below the present $40 \leq A \leq 48$ the ISGMR becomes less identifiable with the $E0$ strength being spread out over a large excitation energy range. Thus, the present $40 \leq A \leq 48$ range could be seen as a transition region and in order to extract centroids and widths of the ISGMR the essentially $E0$ cross-sections of Fig. 4.18 were converted to ISGMR strength (see Section 4.2) and are displayed in Fig. 4.19 after being rebinned to 1 MeV in order to smooth out the fine structure. Then for each of the isotopes a very constrained Lorentzian fit was performed, requiring the

Table 4.4: Values for centroid positions and widths for the ISGMR across the periodic table.

Nucleus	Centroid (MeV)	Width (MeV)	Reference
^{40}Ca	18.0 ±0.1	6.7 ±0.3	Present work
^{42}Ca	17.3 ±0.1	6.0 ±0.2	Present work
^{44}Ca	17.2 ±0.1	6.0 ±0.2	Present work
^{48}Ca	17.9 ±0.1	5.8 ±0.2	Present work
^{58}Ni	17.0 ±0.3	4.0	[You91]
^{58}Ni	16.9 ±0.5	4.0 ±0.8	[Moo19]
^{90}Zr	16.55 ±0.08	4.2 ±0.3	[Gup16]
^{90}Zr	16.12 ±0.04	4.5 ±0.2	[Gup16]
^{92}Mo	16.79 ±0.11	4.2 ±0.4	[Gup16]
^{90}Zr	16.6 ±0.1	4.9 ±0.2	[Uch04]
^{116}Sn	15.4 ±0.1	5.5 ±0.3	[Uch04]
^{114}Sn	15.3 ±0.1	3.7 ±0.12	[Ito03]
^{208}Pb	13.4 ±0.2	4.0 ±0.4	[Uch04]

low excitation-energy region below the corresponding maximum to be fitted well while including in the fit only a few data points above the corresponding maximum. It was thus possible to obtain centroids and widths for ISGMR for each of the calcium isotopes which are given in Table 4.3. It should be noted from Fig. 4.19 that additional $E0$ strength lies above the Lorentzian fits that indicate the ISGMR, limited by the excitation energy range of the oresent measurement. However, in other calcium isotope measurements the $E0$ strength distribution has been measured up to $E_x \approx 40$ MeV by the TAMU and RCNP groups, as seen in Fig. 4.14, 4.15, 4.16 and 4.17 for ^{48}Ca, ^{44}Ca, ^{42}Ca and ^{40}Ca, respectively. Typically, a moments analysis has been performed on such $E0$ strength distributions from which a centroid of the distribution can be extracted (see, for example, Refs. [You13, Lui11, How20]). Values for the extracted centroids depend on the extended excitation energy range and are very sensitive to the arbitrary background subtraction used in the MDA

Table 4.5: Centroid energies (in MeV) calculated from the moment ratio (m_1/m_0) over the energy range 10 to 25 MeV. For comparison purpose centroid energies were also calculated for TAMU and RCNP data set over the excitation energy range 10 MeV to 25 MeV.

Nucleus	m_1/m_0 (MeV)		
	This work	RCNP	TAMU
^{40}Ca	18.30±0.1	17.74±0.1	18.18±0.4
^{42}Ca	18.46±0.1	17.65±0.1	
^{44}Ca	18.31±0.1	17.71±0.1	17.77±0.35
^{48}Ca	18.15±0.1	18.00±0.1	17.36±0.2

analysis. These values do not represent the corresponding centroids of the ISGMRs but rather the centroids of the $E0$ distributions themselves. Table 4.3 has been extended to include measured ISGMR centroid values up to ^{208}Pb, as shown in Table 4.4. The values are plotted in Fig. 4.20. Here, the trend is clearly obvious as mass decreases and would result in only an increase of about ± 0.5 MeV for centroids in the $40 \leq A \leq 48$ region if the $E0$ strength distribution from $10 \leq E_{\mathrm{x}} \leq 25$ MeV was included as opposed to a constrained Lorentzian fit in this region.

Furthermore, the centroid energies were calculated from moment ratio, m_1/m_0, over the excitation energy range $E_{\mathrm{x}} = 10$ to 25 MeV. This was done in order to allow a comparison with the TAMU and RCNP datasets. These datasets however has access to data at much higher excitation energies. The same calculation was therefore performed on TAMU and RCNP data sets over the same energy range as that applicable to the data acquired at iThemba LABS and the results are compared in Table 4.5. From Table 4.5 it is clear that centroid energy obtained from moment ratio analysis strongly depends on the range of excitation energy chosen as it is shown from TAMU and RCNP data sets. For these two data set, the trend of the centroid energy along the calcium isotope chain for the smaller energy range ($E_{\mathrm{x}} = 10$ to 25 MeV) is the exact opposite of the trend observed for the bigger energy range ($E_{\mathrm{x}} = 10$ to 40 MeV) for TAMU [Lui11, But17] and $E_{\mathrm{x}} = 10$ to 31 MeV for RCNP [How20]). However, the differences in ^{48}Ca and ^{40}Ca is much smaller in RCNP data than

it is for TAMU data. In the present work, the trend seen from the moment ratio analysis (see Table 4.5) is the same as the one observed from fitting the data to a Lorentzian function (see Table 4.3), which is that the centroid energy of ^{48}Ca is slightly smaller than that of ^{40}Ca. In between ^{42}Ca and ^{44}Ca the result seems to be outside of the trend in ^{48}Ca and ^{40}Ca.

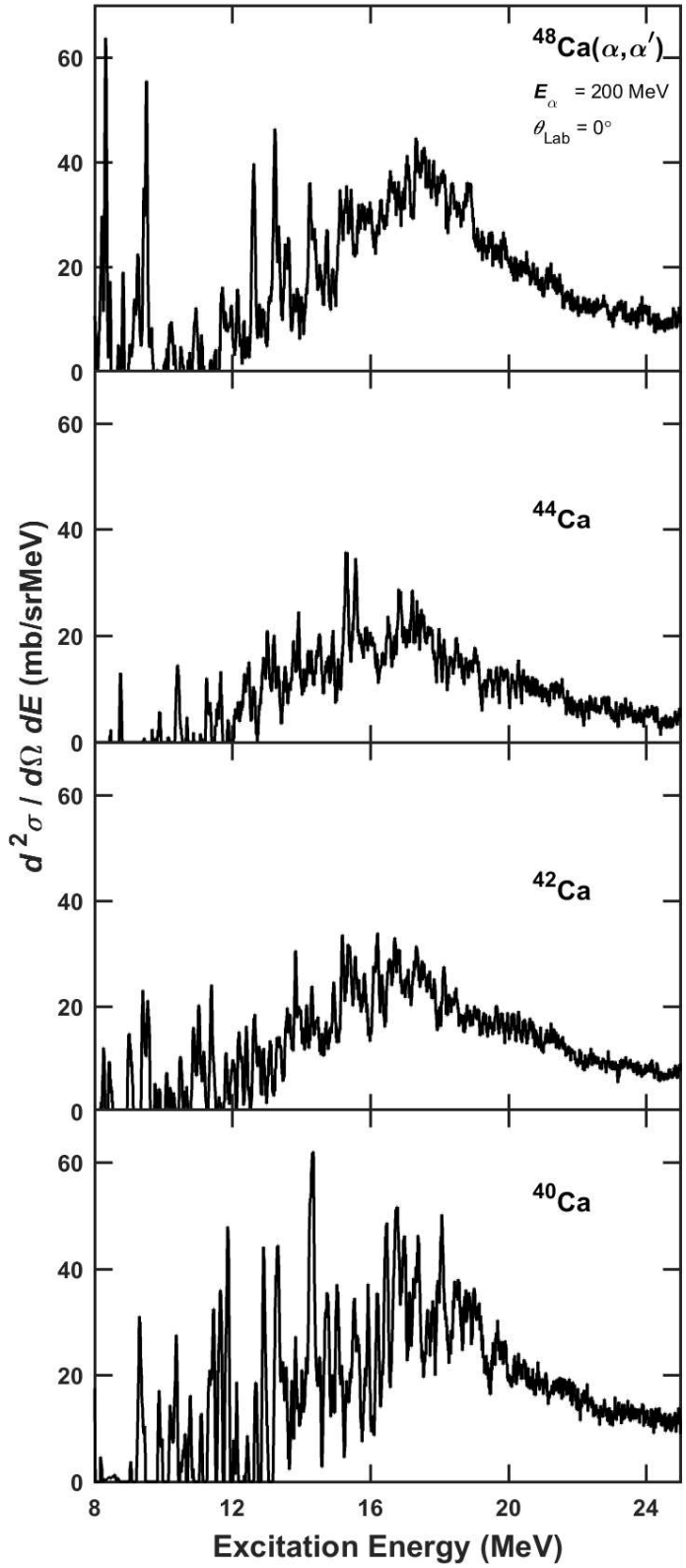


Figure 4.18: Double-differential cross section of the difference spectra for ^{40,42,44,48}Ca at $E_\alpha = 200$ MeV.

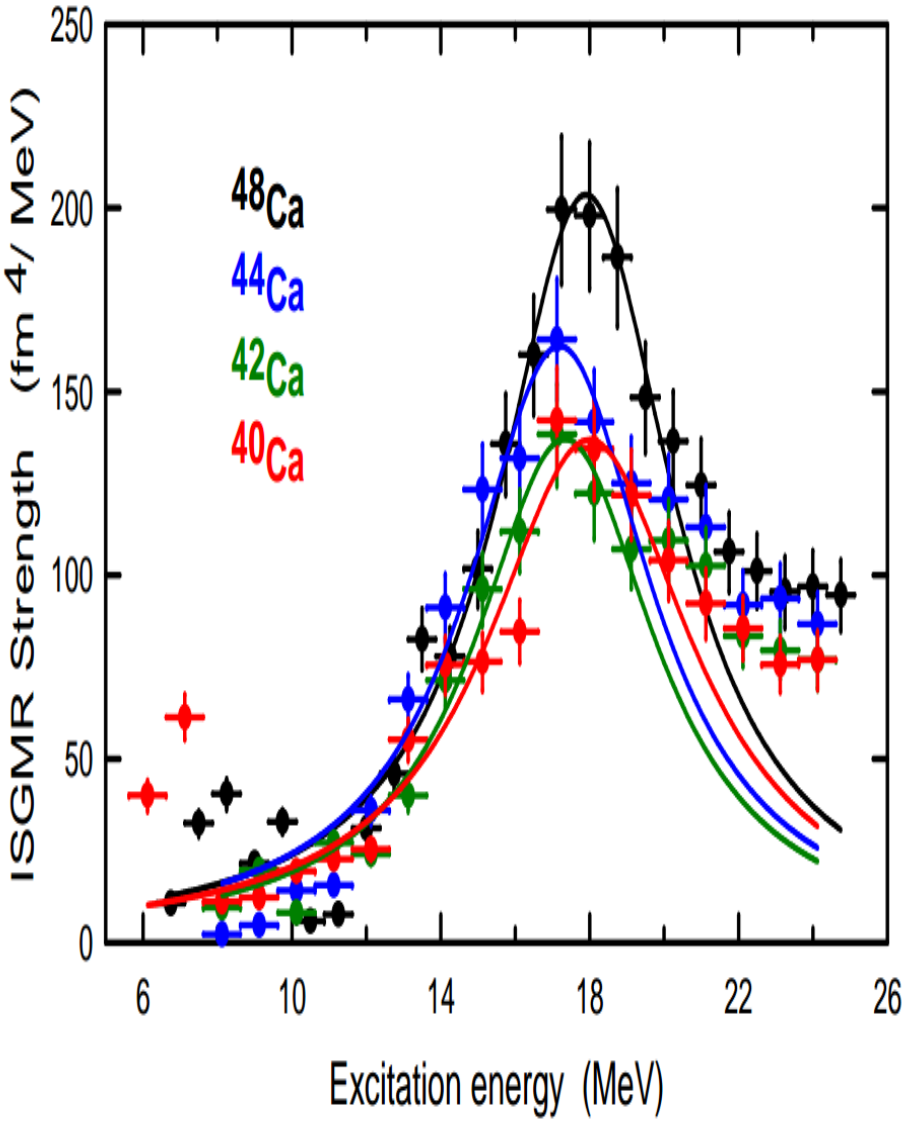


Figure 4.19: ISGMR strength distribution for ^{48}Ca (black circles), ^{44}Ca (blue circles), ^{42}Ca (green circles) and ^{40}Ca (red circles). The solid lines represent the Lorentzian fit.

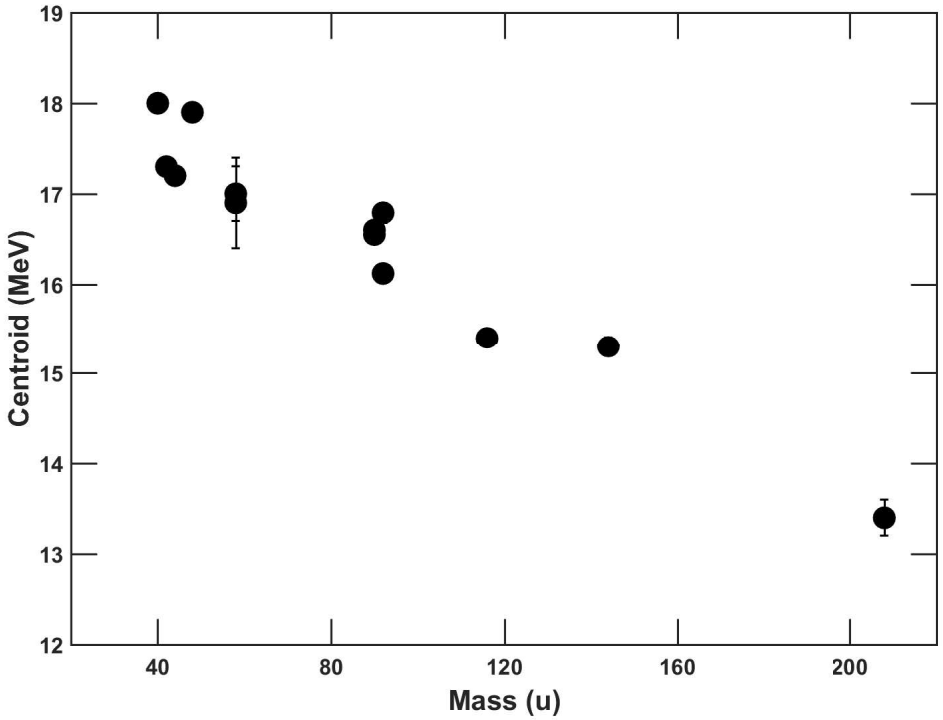


Figure 4.20: Overview of the centroid values for the ISGMR across the periodic table (see Table 4.4).

4.3.2 Comparison of experimental ISGMR and theoretical predictions for ^{48,44,42,40}Ca

In order to compare the experimentally measured excitation-energy spectra for the calcium isotopes in the region of the ISGMR, $E0$ strength functions were calculated using the various microscopic models described in Section 2.2.1. Starting from the simplest to the most complex these include:

- RPA (Random Phase Approximation) [Pap19] (see Section 2.2.1.1).
- SRPA (Second RPA) [Pap19] (see Section 2.2.1.2).
- QRPA (Quasi-particle RPA) [Lit19] (see Section 2.2.1.3).
- QTBA (Quasi-particle Time Blocking Approximation) [Lit19] (see Section 2.2.1.4).
- PPC (Phonon Phonon Coupling) [Ars19] (see Section 2.2.1.5).

The experimental data together with calculated ISGMR strength functions in ^{48}Ca, ^{44}Ca, ^{42}Ca, and ^{40}Ca are presented in Figs. 4.21, 4.22, 4.23 and 4.24, respectively.

The calculated $E0$ strength distributions for the different models were smoothed with a Gaussian function with a width comparable to the energy resolution of the experiment, i.e. FWHM = 85 keV, and put into a bin size of 10 keV. This is to allow for a direct comparison between experiment and theory. The results of such process are shown in the second panel from the top in Figs. 4.21 - 4.24 for all the calcium isotopes.

The result from the PPC model is shown in the second panel of each figure, while the QTBA is shown in the third panel and the QRPA in the fourth panel. Appreciable fine structure is seen in both the QTBA and the QRPA calculations, although less than in the case of the PPC calculations. While the position of the main strength from the PPC calculations seems to agree with the experimental data, the QTBA and QRPA models place the main $E0$ strength above the ISGMR for all the calcium isotopes.

The SRPA and RPA calculations were performed only for ^{48}Ca, ^{42}Ca, and ^{40}Ca and the results are shown in the fifth and sixth panels down of Figs. 4.21, 4.23 and 4.24, respectively. Both calculations show no fine structure as expected. The SRPA places the $E0$ strength in the region of the ISGMR while the RPA shifts the strength to higher energies for all three calcium isotopes.

Overall, the PPC best represents the experimental data in terms of the $E0$ strength in the region of the ISGMR and above, as shown in the top panel in each of the figures where the corresponding experimental ISGMR strength distribution is overlaid with the PPC result folded with a 2 MeV wide Lorentzian. The PPC model also displays considerable fine structure for all of the calcium isotopes.

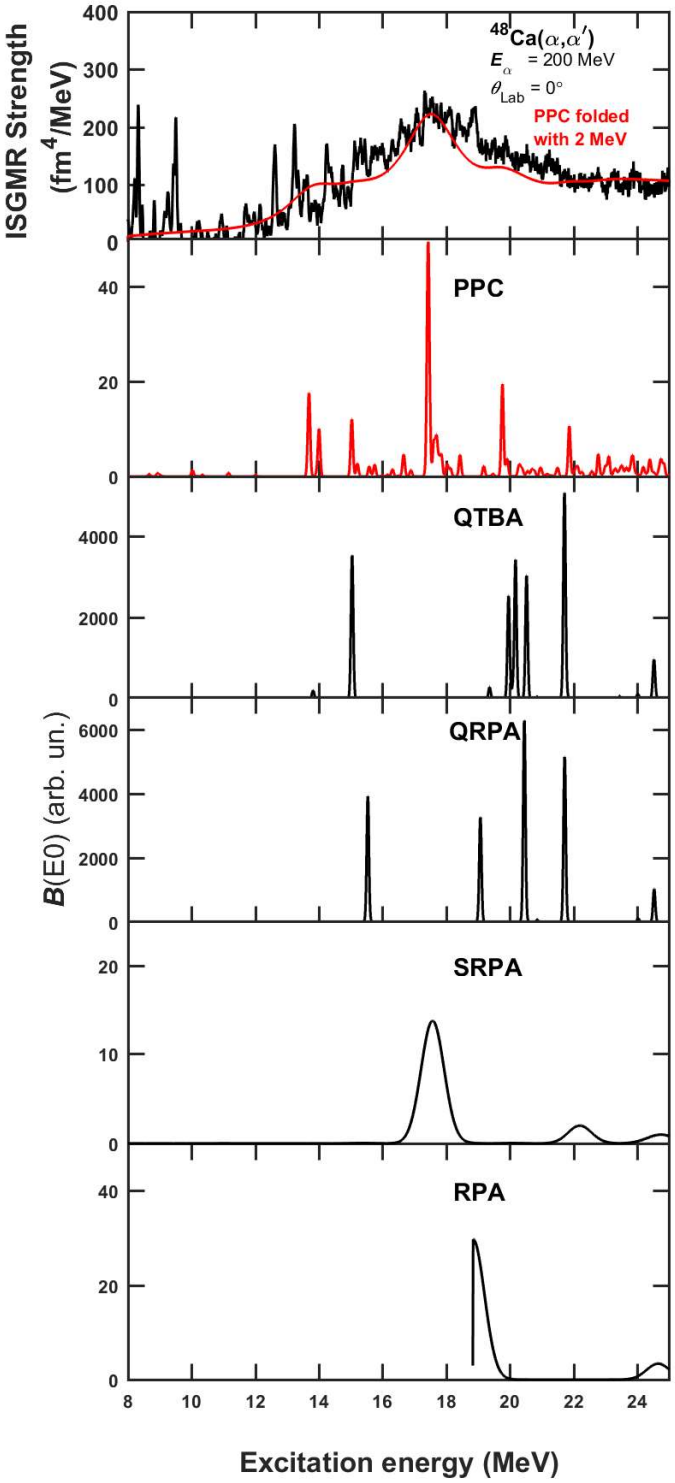


Figure 4.21: From top to bottom: ISGMR strength distribution for ^{48}Ca(α, α') overlaid with PPC result (in red) folded with 2 MeV; strength functions within the framework of PPC, QTBA, QRPA, SRPA and RPA.

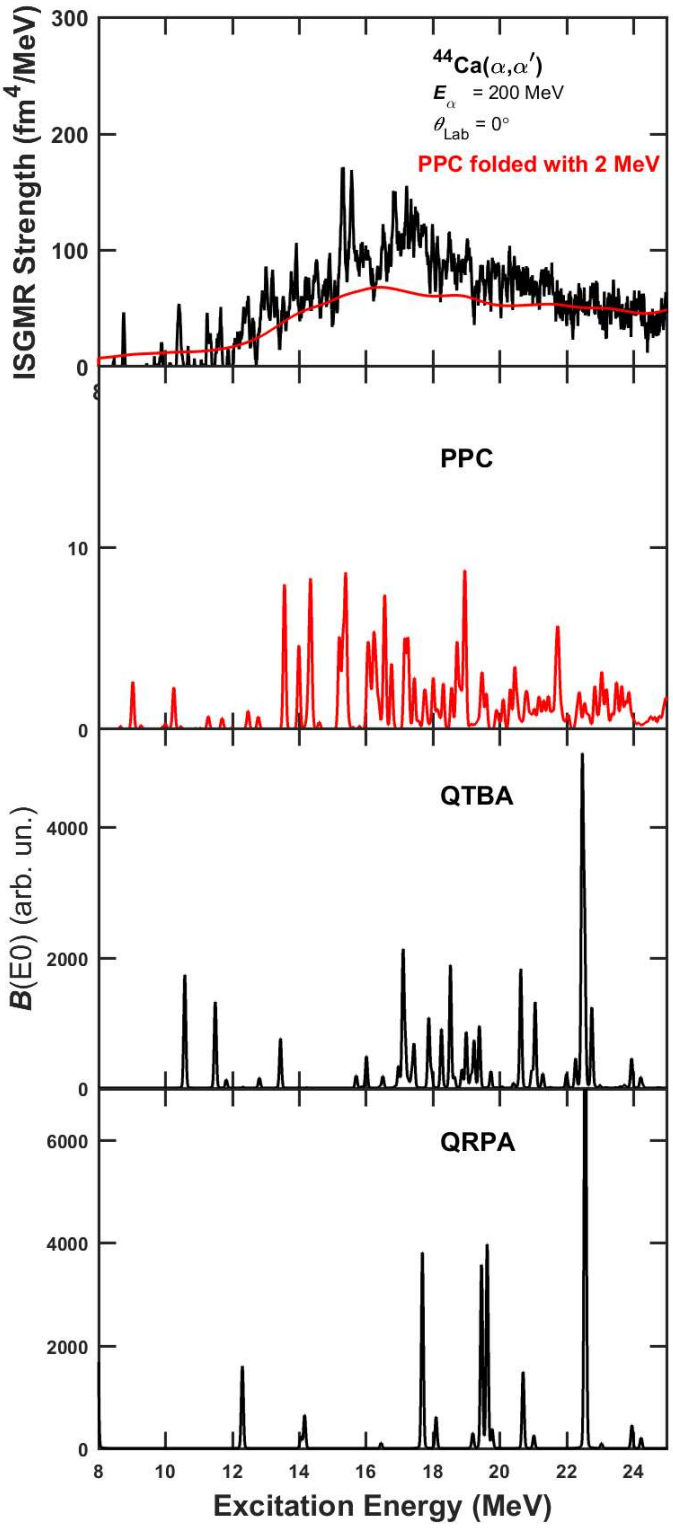


Figure 4.22: From top to bottom: ISGMR strength distribution for ^{44}Ca(α, α') overlaid with PPC result (in red) folded with 2 MeV; strength functions within the framework of PPC, QTBA and QRPA.

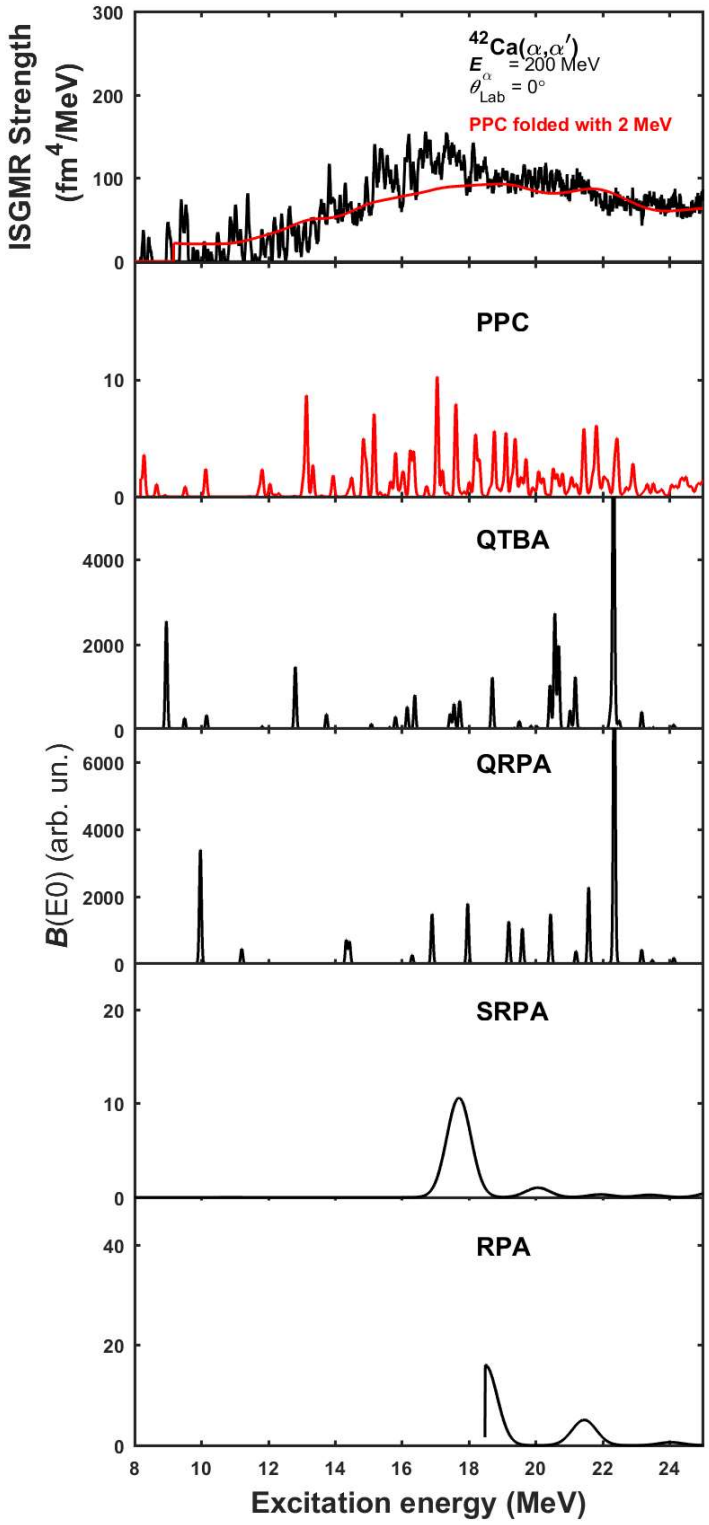


Figure 4.23: From top to bottom: ISGMR strength distribution for ^{42}Ca(α, α') overlaid with PPC result (in red) folded with 2 MeV; strength functions within the framework of PPC, QTBA, QRPA, SRPA and RPA.

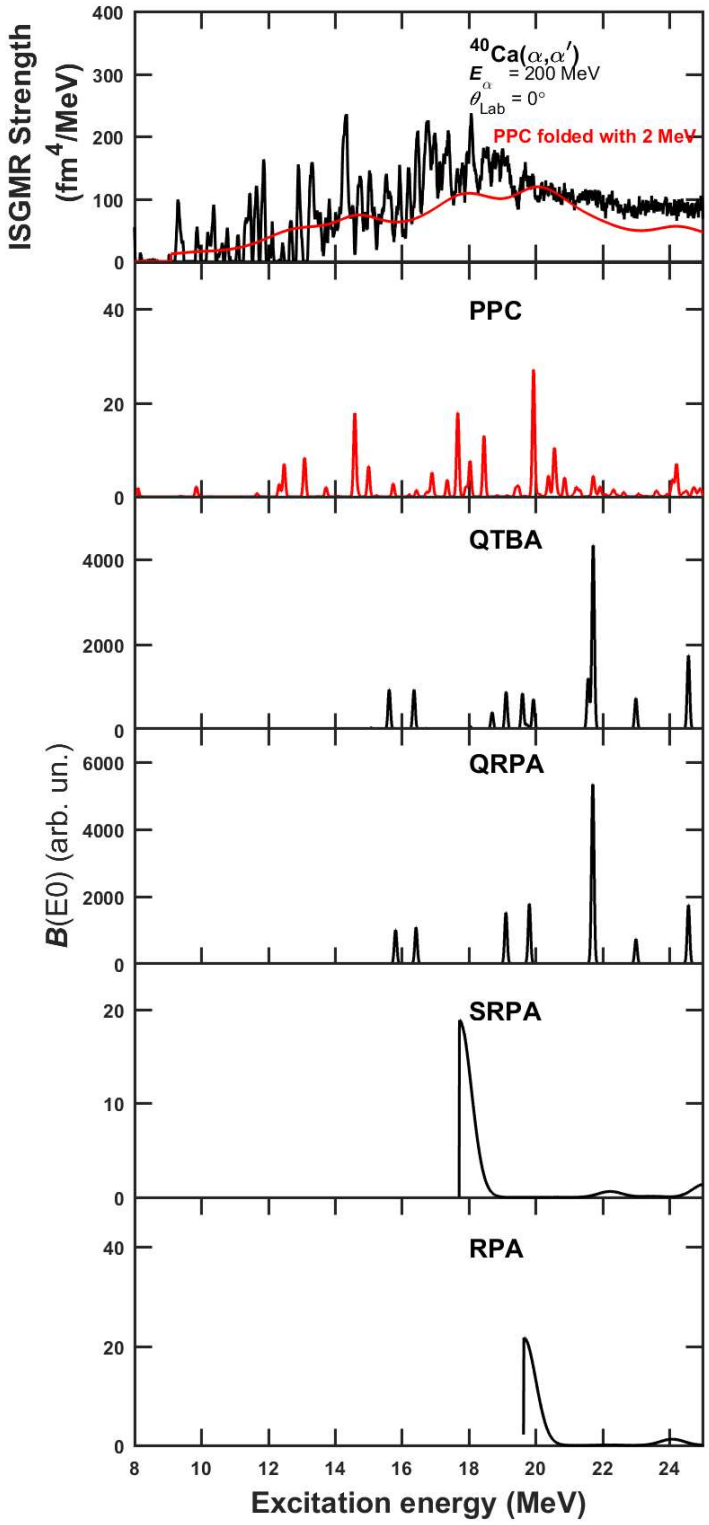


Figure 4.24: From top to bottom: ISGMR strength distribution for ^{40}Ca(α, α') overlaid with PPC result (in red) folded with 2 MeV; strength functions within the framework of PPC, QTBA, QRPA, SRPA and RPA.

4.4 Fine structure analysis of ^{40,42,44,48}Ca $E0$ strength

The extraction of characteristic energy scales from excitation-energy spectra using wavelet analysis allows comparisons to be made to the measured data and the various microscopic model predictions of the ISGMR. Ideally, a comparison should be made to the difference spectrum which represents the extracted $E0$ component using the DoS technique. Here, the effect on energy scales before and after subtraction of the 4° angle cut is first investigated in Section 4.4.1. Following which the results of the analysis and the extracted characteristics scales for ^{48}Ca, ^{44}Ca, ^{42}Ca and ^{40}Ca are presented and discussed in Section 4.4.2.

4.4.1 Effect of the DoS technique on the extraction of energy scales

The use of the DoS technique might have adverse effects on the wavelet analysis results either by inducing extra energy scales or completely suppressing some of them. This concern was investigated by comparing the wavelet power spectra of the equivalent zero-degrees spectra to those of the difference spectra. By way of example, results for ^{48}Ca are presented in Fig. 4.25. In this figure the $\theta_{\rm Lab} = 0°$ spectrum (Fig. 4.10 blue) and the DoS spectrum (Fig. 4.10 black) are shown in the first and third panels down on the right hand side column, respectively. Following the techniques outlined in Section 2.3, for each of the spectra the real part of the wavelet coefficients as a function of excitation energy, which is given by Eq. (2.44), was obtained from a Continuous Wavelet Transform (CWT) (see Section 2.3.1). The results are the two-dimensional plots shown in the second and fourth panels down on the right hand side of Fig. 4.25. The blue regions indicate negative values while the red indicate positive values. The blue and the black spectra on the left hand side of the Fig. 4.25 represent the projections of the corresponding wavelet coefficients on the scale axis (power spectrum) for the $\theta_{\rm Lab} = 0°$ and DoS spectra, respectively. Power spectra were determined by using the CWT coefficients in the excitation energy region of 12 - 24 MeV as indicated by the dashed black lines, and is consistent with the appearance of $E0$ strength for the various models shown in Figs. 4.21 to 4.24. As shown the left-hand-side lowest panel, overlapping

the power spectra show identical scales with some variation in the relative strength. This is an indication that the DoS technique has no adverse effect on the extracted wavelet energy scales. Similar results were obtained for ^{44}Ca, ^{42}Ca and ^{40}Ca and are shown in Figs. 4.26, 4.27 and 4.28, respectively.

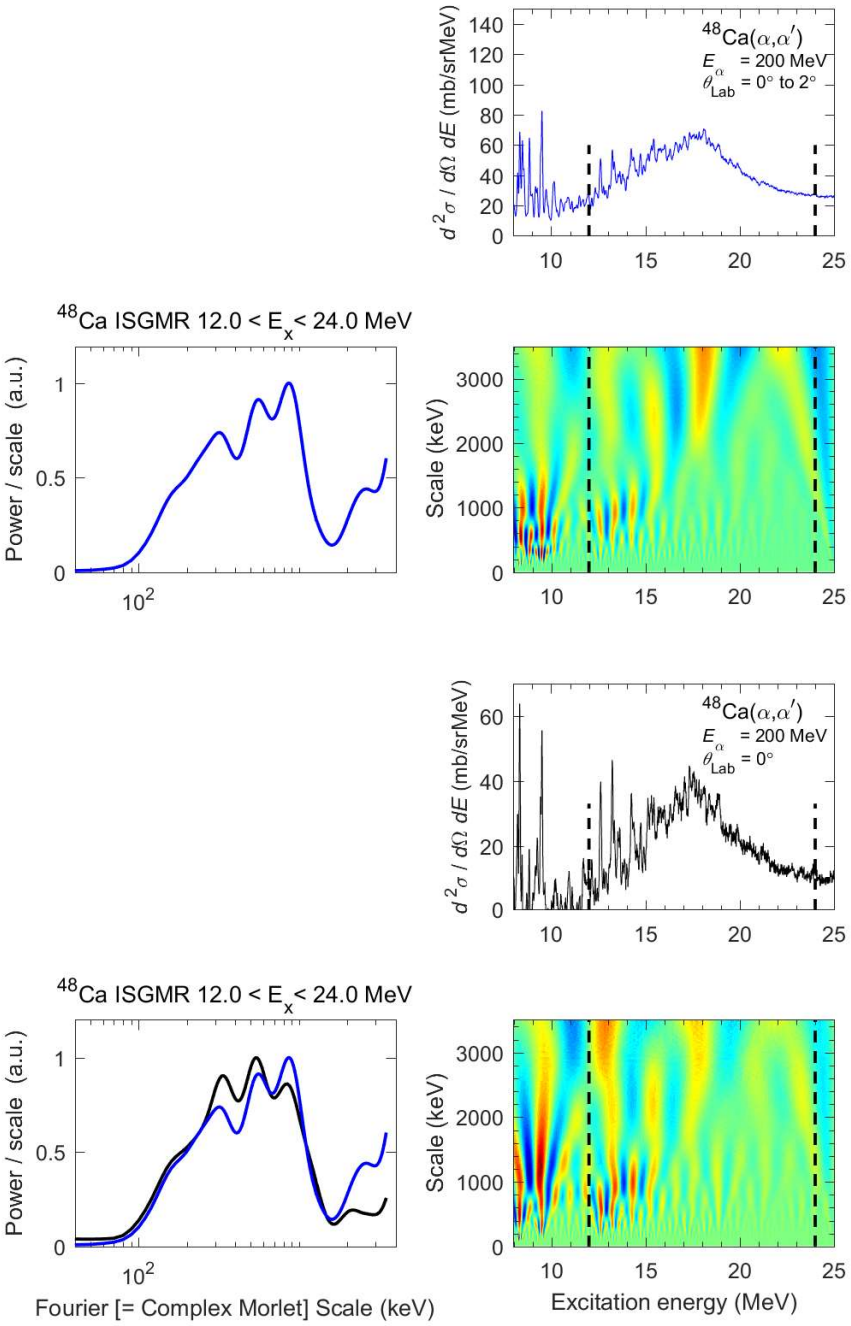


Figure 4.25: *Top Segment*: Experimental double-differential cross section for ^{48}Ca(α, α') at $\theta_{\rm Lab} = 0°$-2° (top right panel), wavelet coefficients from CWT (right panel on the second row down) and power spectrum (left panel on the second row down). *Bottom segment*: Difference spectrum for ^{48}Ca(α, α') (right panel on the third row down), wavelet coefficients from CWT (right panel on the lowest row) and corresponding power spectrum in black superimposed on power spectrum from $\theta_{\rm Lab} = 0°$ data (left panel on the lowest row).

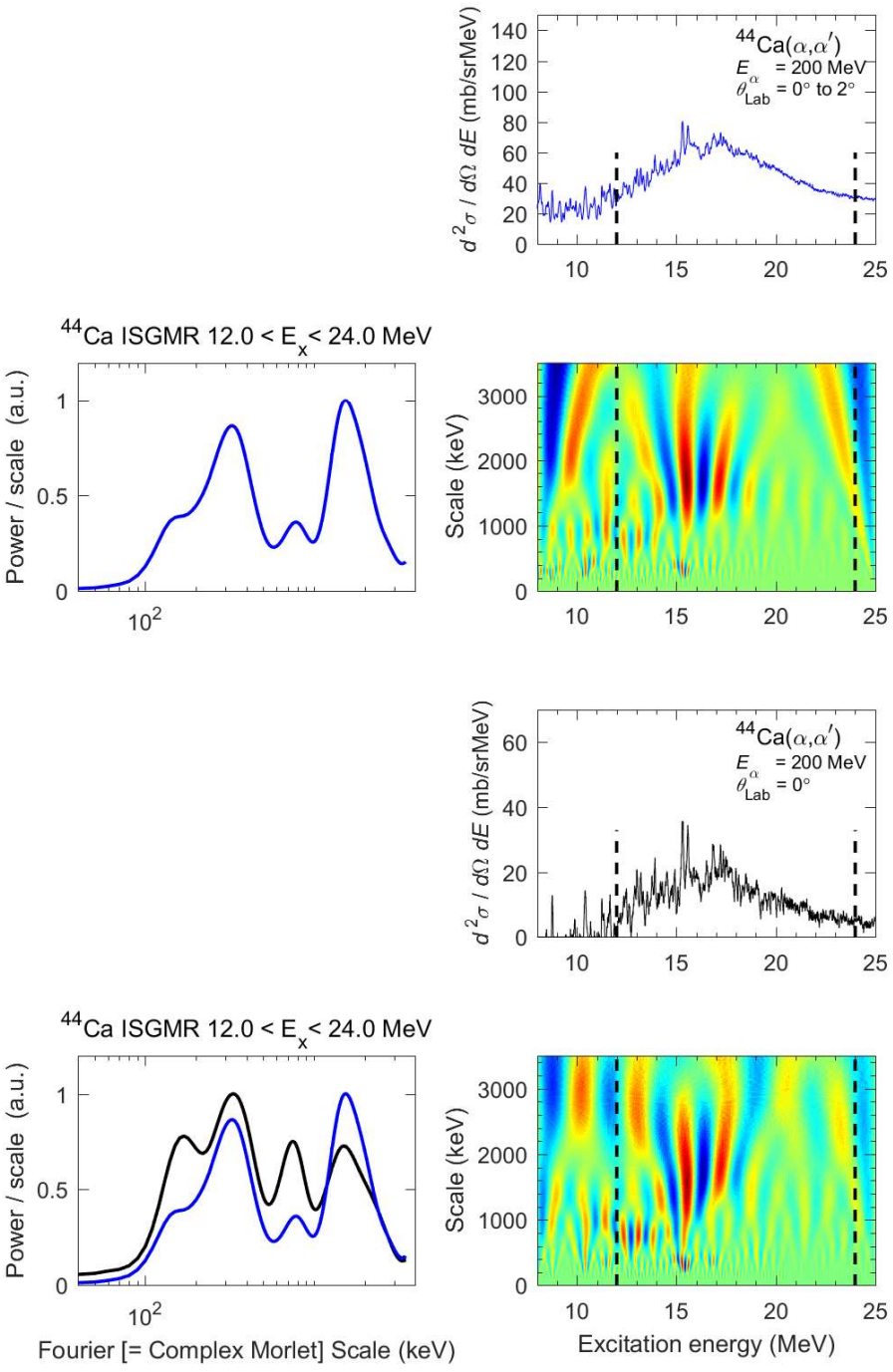


Figure 4.26: Same as Fig 4.25, but for ^{44}Ca.

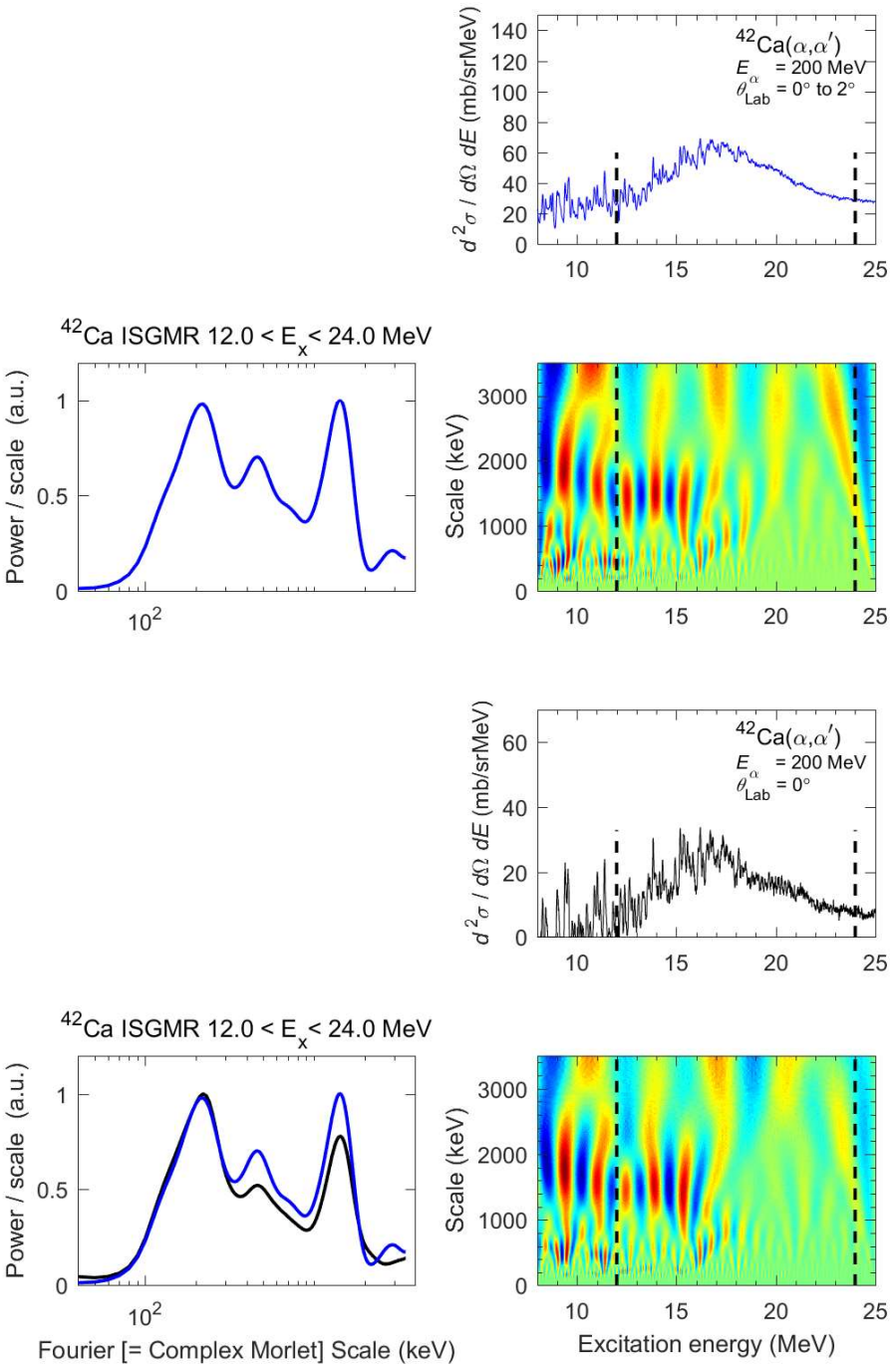


Figure 4.27: Same as Fig 4.25, but for ^{42}Ca.

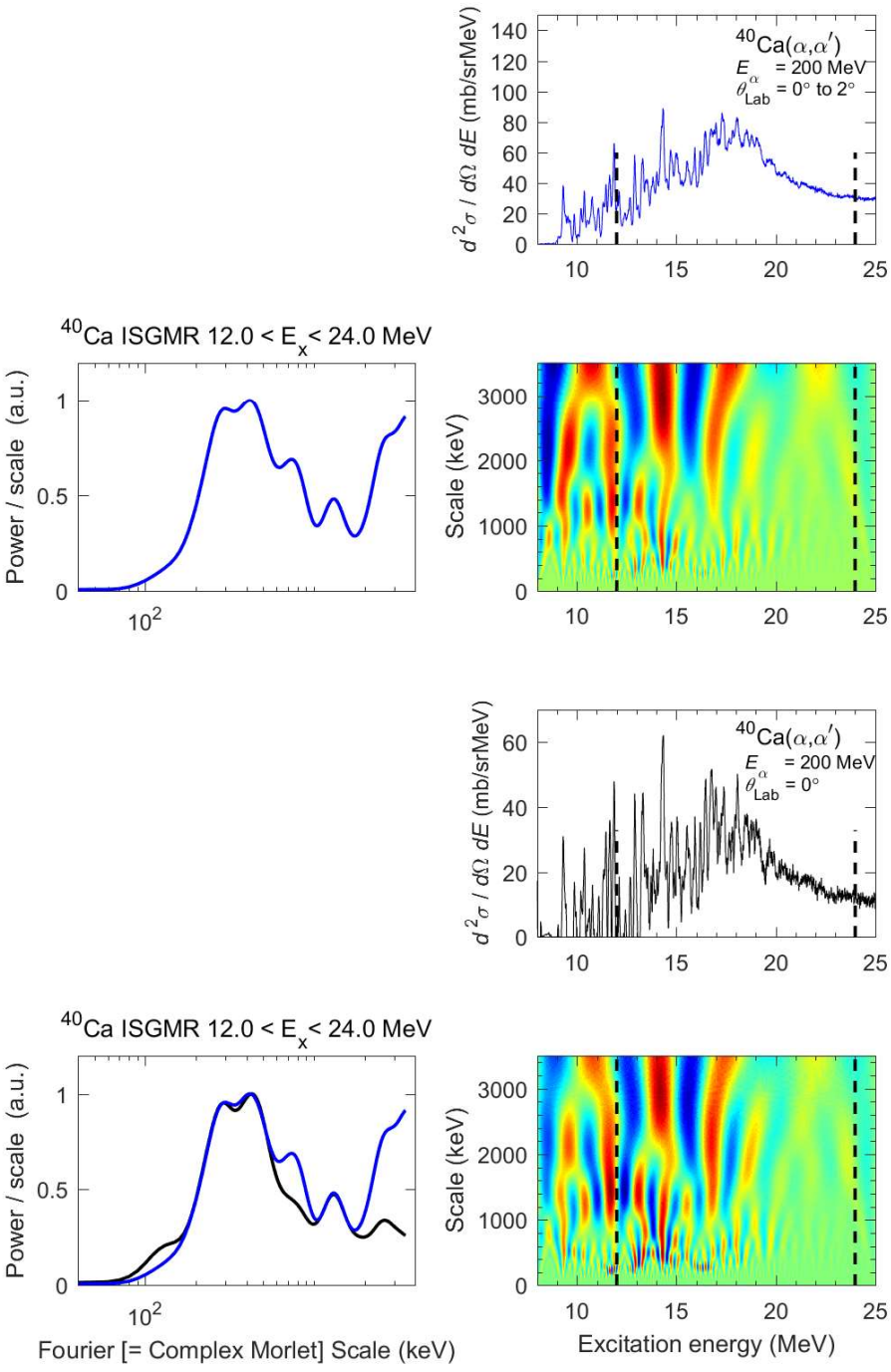


Figure 4.28: Same as Fig 4.25, but for ^{40}Ca.

4.4.2 Experimental and theoretical wavelet energy scales

The results of the wavelet analysis on the measured spectra for the doubly-magic ^{48,40}Ca and the singly magic ^{44,42}Ca are shown in Figs. 4.29 and 4.30, respectively. A comparison of the power spectra in Fig. 4.29 reveals similar scales for ^{48}Ca and ^{40}Ca. The singly magic nulcei ^{44}Ca and ^{42}Ca also show very similar scales but different from those of the doubly-magic nuclei, as shown in Fig. 4.30.

The experimental and theoretical electric monopole responses together with the corresponding power spectra for ^{48}Ca, ^{44}Ca, ^{42}Ca and ^{40}Ca are shown in Figs. 4.31, 4.32, 4.33 and 4.34, respectively. In each of these figures experimental spectra and the theoretical strength distributions are shown on the right column while the corresponding power spectra are shown on the left column. The black arrows point at the peaks of strength of the power spectrum. These peaks are associated with the characteristic scales in the region of the ISGMR. In order to make comparison between the different experimental results and with theoretical results, the scales are categorised into classes based on energy regions. Scales in the region 0 to 300 keV are in class I while those in the region 300 keV to 1000 keV are in Class II. Class III is for scales above 1000 keV. Scales above 3000 keV are trivial and represent the width of the resonance. The extracted characteristic energy scales for the doubly-magic ^{48,40}Ca and the singly magic ^{44,42}Ca are presented in Tables 4.6 and 4.7, respectively. Equivalent characteristic energy scale values are shown in red. Equivalent characteristic energy scale refers to scales present in both experimental data and any of the theoretical models.

Table 4.6: Characteristic energy scale values extracted from the experimental spectrum and theoretical calculations of the PPC, QTBA and QRPA for doubly-magic ^{48,40}Ca. Equivalent characteristic energy scale values are shown in red.

Nucleus		Class I $\Delta E \lesssim$300 keV	Class II 300$\leq \Delta E \leq$1000 keV	Class III $\Delta E \geq$1000 keV
^{48}Ca	Experiment	180 ——	340 540 840	—— 2100
	PPC	—— ——	300 —— 810	1100 2100
	QTBA	200 ——	300 560 ——	1500 ——
	QRPA	—— ——	320 640 ——	1300 ——
^{40}Ca	Experiment	130 290	430 780 ——	1300 2600
	PPC	220 ——	380 700 ——	—— 2400
	QTBA	200 ——	450 650 970	1400 2600
	QRPA	—— ——	330 620 970	1400 2600

Table 4.7: Characteristic energy scale values extracted from the experimental spectrum and theoretical calculations of the PPC, QTBA and QRPA for ^{44,42}Ca. Equivalent characteristic energy scale values are shown in red.

Nucleus		Class I $\Delta E \lesssim$300 keV	Class II 300$\leq \Delta E \leq$1000 keV	Class III $\Delta E \geq$1000 keV
^{44}Ca	Experiment	170 ——	330 —— 750	—— 2100
	PPC	—— 250	360 —— 910	—— 2400
	QTBA	—— 280	—— 680 ——	1600 ——
	QRPA	210 ——	—— —— 890	1600 ——
^{42}Ca	Experiment	220 ——	460 —— ——	1400 ——
	PPC	220 ——	310 560 ——	1000 ——
	QTBA	—— 290	430 560 880	1600 ——
	QRPA	—— 270	370 680 ——	—— ——

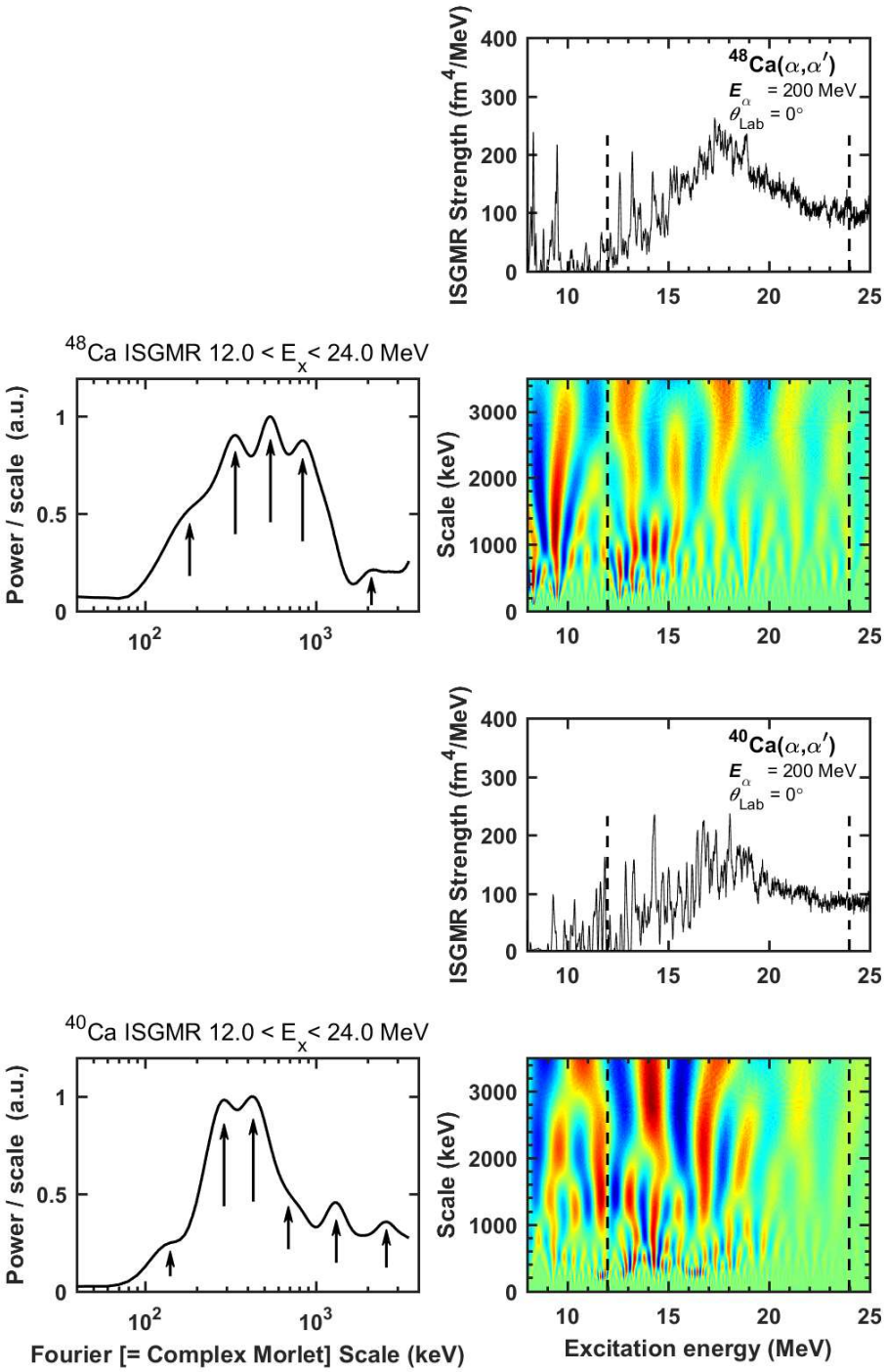


Figure 4.29: *Top Segment*: ISGMR strength distribution for ^{48}Ca(α, α') (top right panel), wavelet coefficients from CWT (right panel on the second row) and power spectrum (left panel on the second row). *Bottom Segment*: ISGMR strength distribution for ^{40}Ca(α, α') (right panel on the third row), wavelet coefficients from CWT (right panel on the last row) and power spectrum (left panel on the last row) with characteristic energy scales indicated by the black arrows. Excitation-energy region of 12 - 24 MeV was considered as indicated between the dashed black lines.

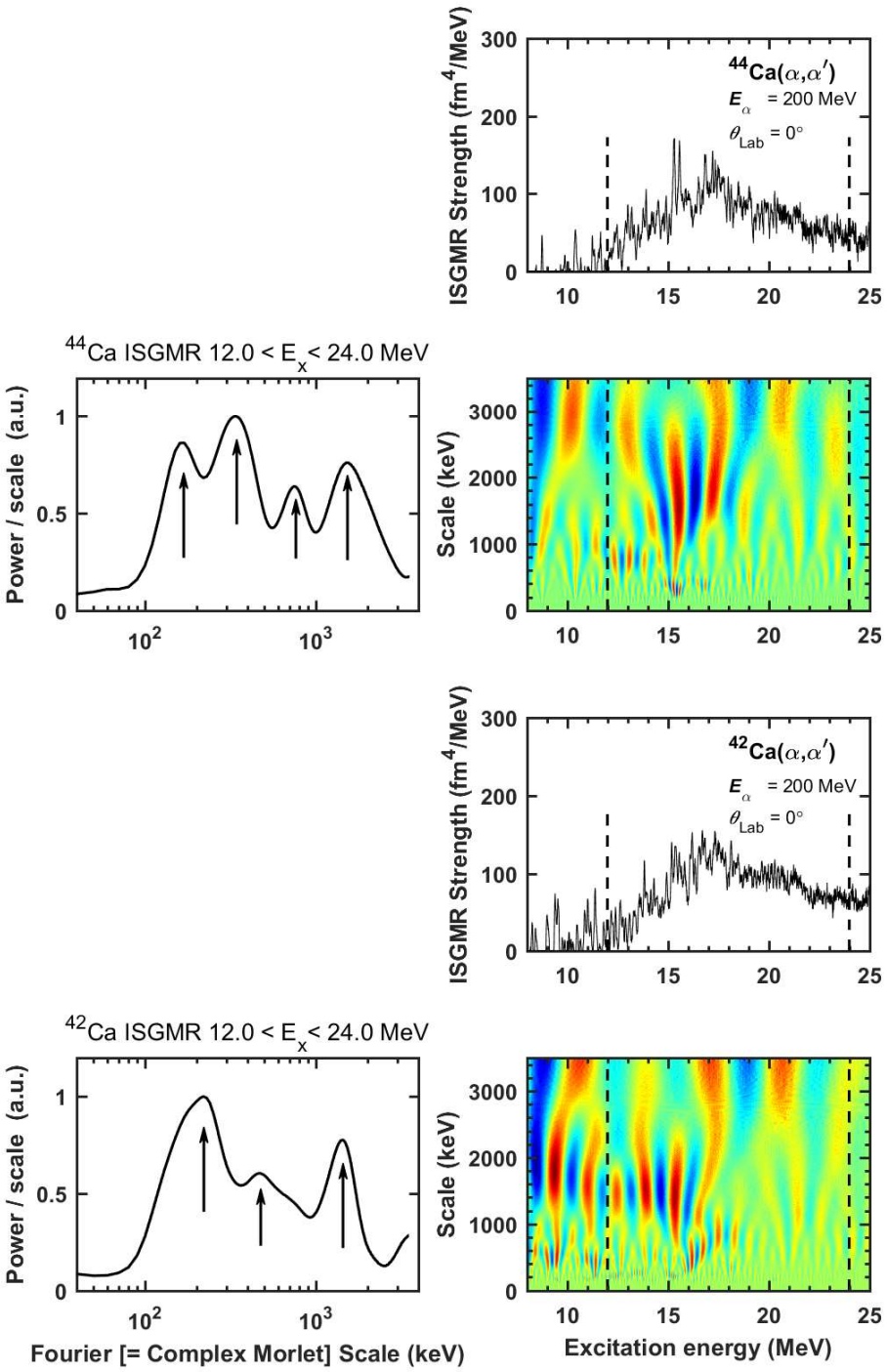


Figure 4.30: Same as Fig 4.29, but for ^{44}Ca and ^{42}Ca.

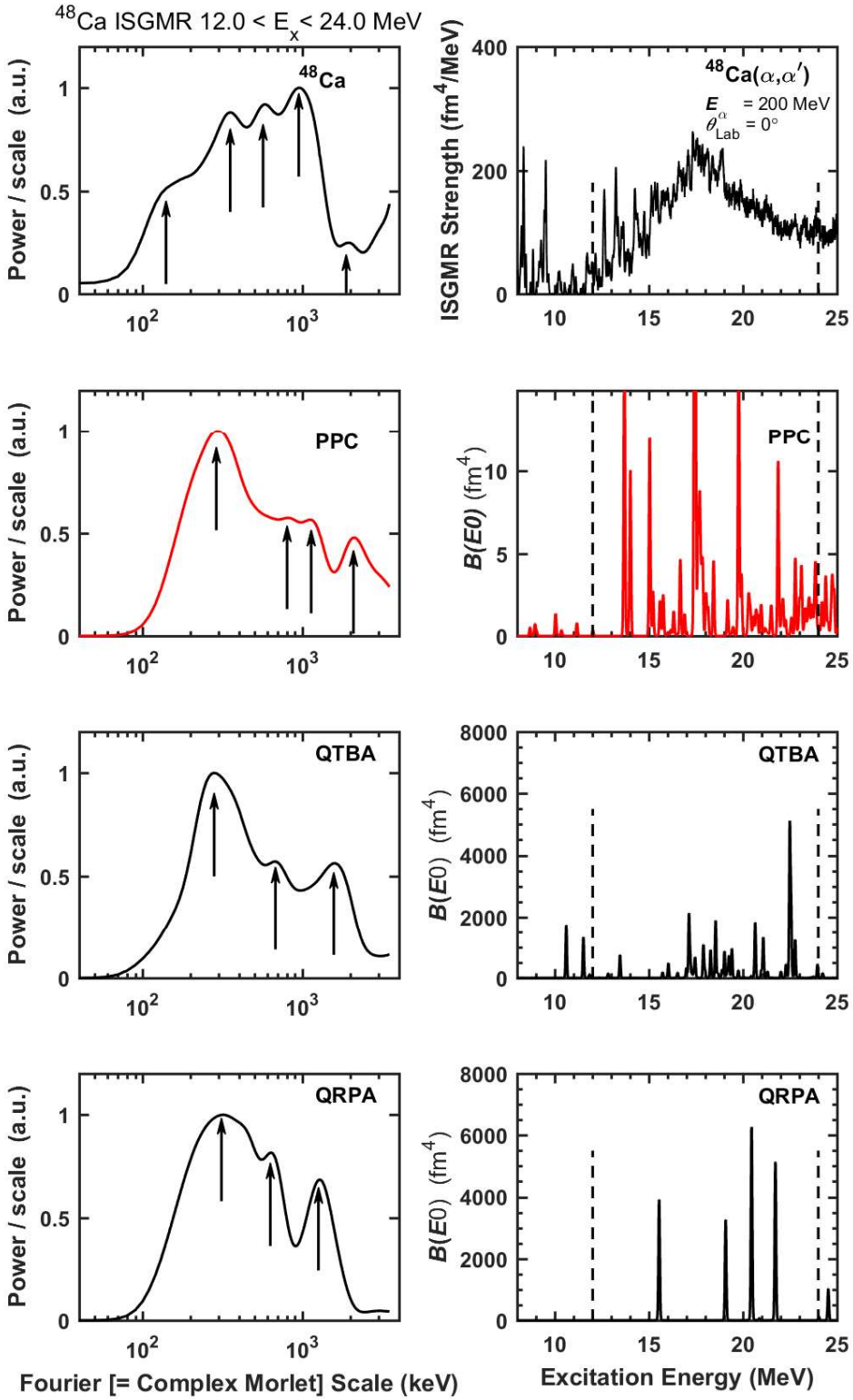


Figure 4.31: *From top to bottom*: On the right hand side is the ^{48}Ca(α, α') spectrum, the ^{48}Ca - PPC spectrum, the ^{48}Ca - QTBA spectrum and the ^{48}Ca - QRPA spectrum. On the left hand side are the corresponding power spectra with the characteristic scales pointed out with black arrows.

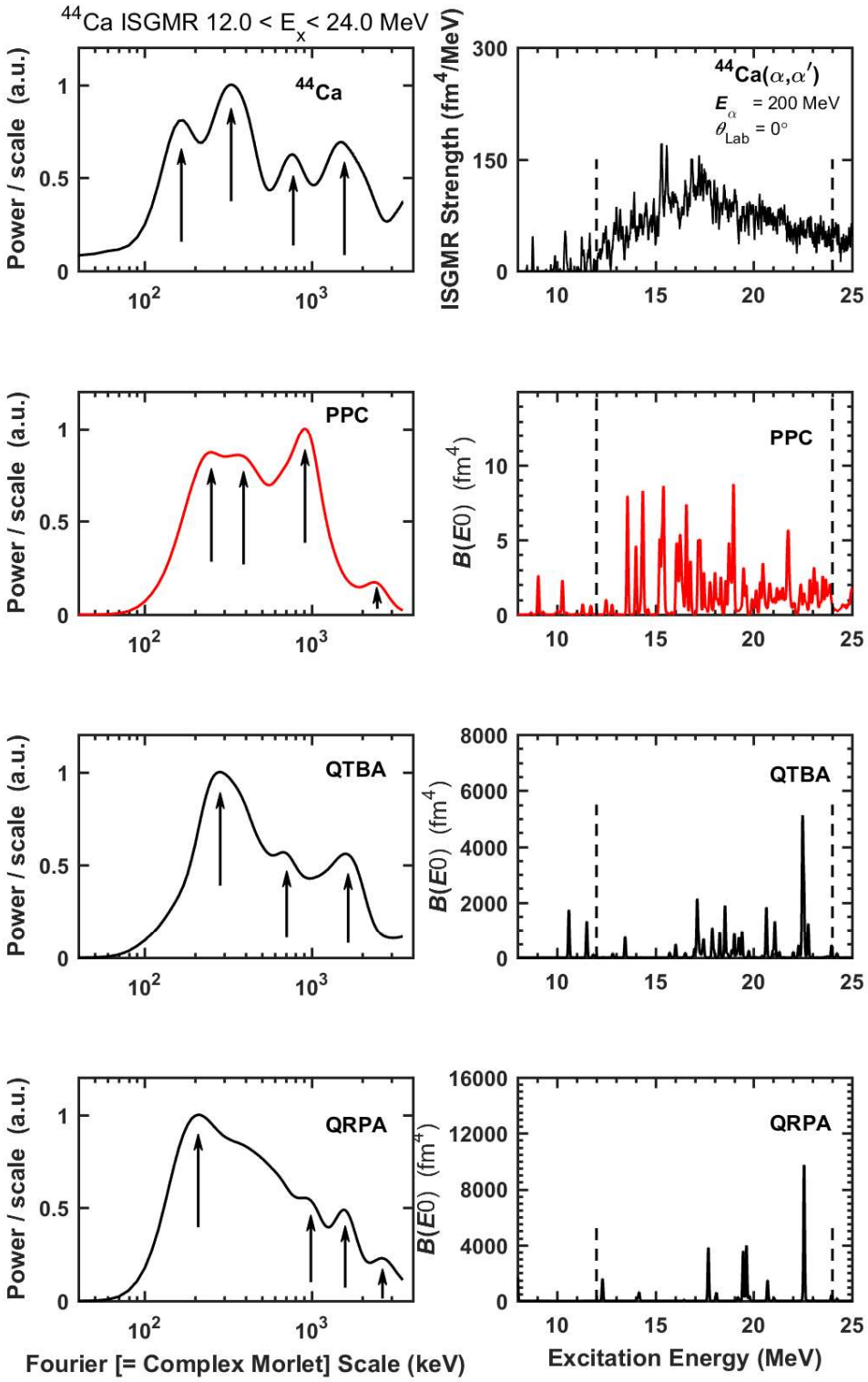


Figure 4.32: Same as Fig. 4.31 but for ^{44}Ca

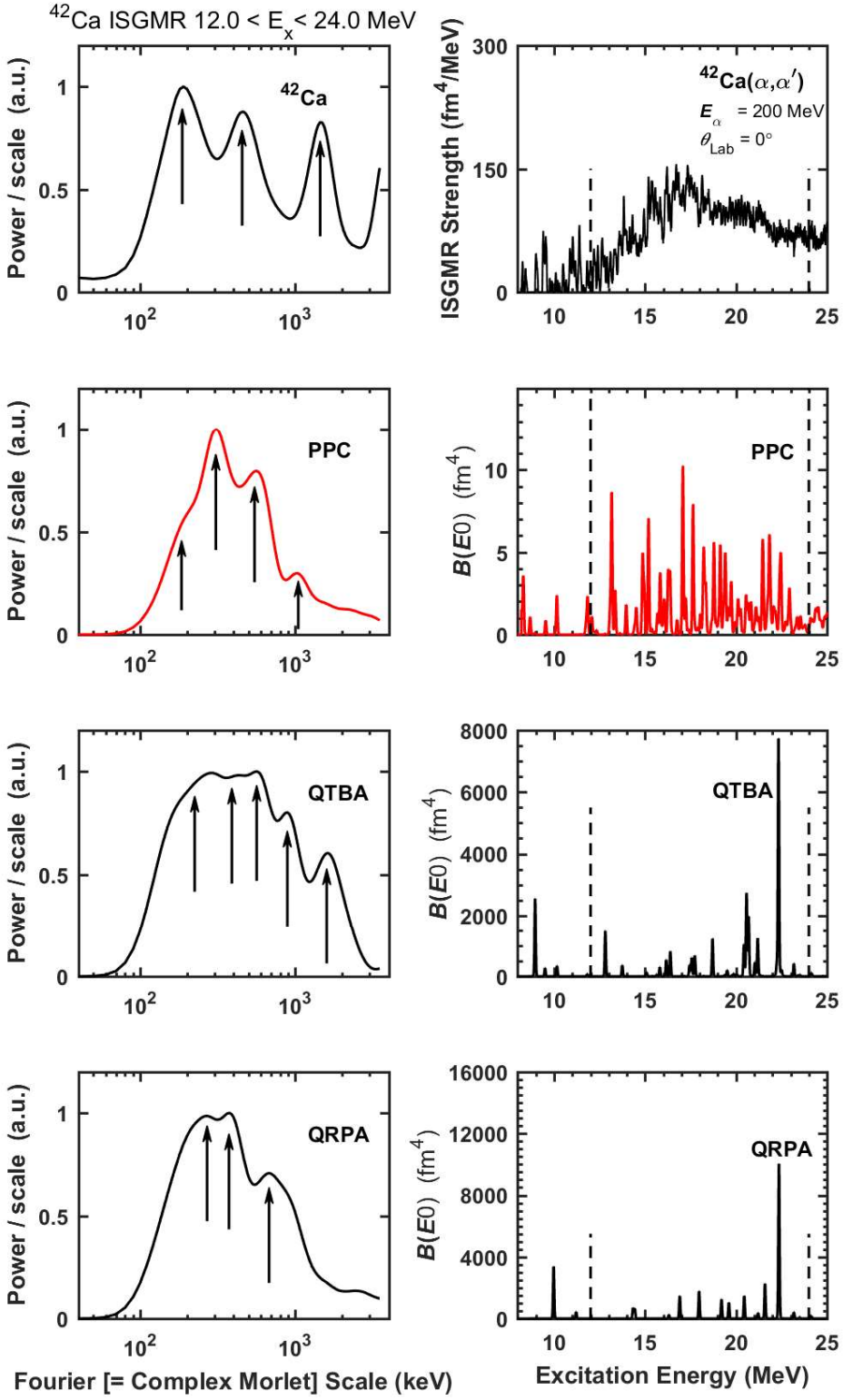


Figure 4.33: Same as Fig. 4.31 but for ^{42}Ca

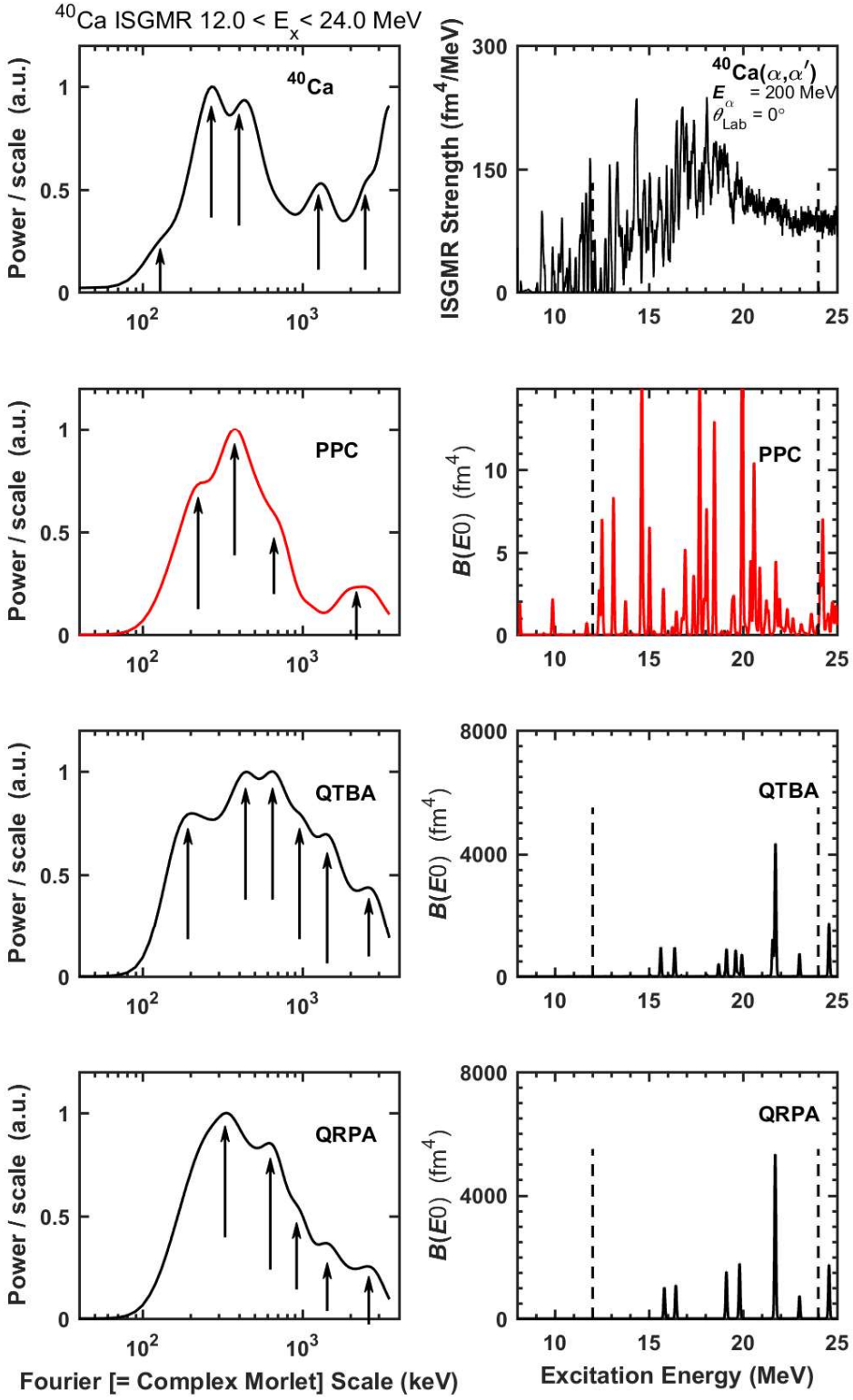


Figure 4.34: Same as Fig. 4.31 but for ^{40}Ca

4.4.2.1 Discussion

As seen in Table 4.6, for the case of ^{48}Ca, the three classes of scales are present in the experimental data as well as in PPC and QTBA calculations. In QRPA result Class I is missing but Class II and Class III are present. The PPC reproduce the experimental scales well except for the 340 keV and 540 keV. Also, the QTBA mimic the experimental scales with the exception of the 340 keV and 840 keV. A combination of the PPC and the QTBA gave a better representation of the experimental data for ^{48}Ca in terms of the number equivalent scales.

As seen in Table 4.6, for the case ^{40}Ca, the three classes of scales are present in the experimental data as well as in PPC and QTBA calculations. In QRPA results Class I is missing but Class II and Class III are present. In Class I all the theoretical results fail to give corresponding scale for the 130 keV scale in the experimental data. The two scales observed in experiment in class II are predicted by the PPC while only one of the scales was predicted by the QRPA. In Classes III all the theory agree reasonably well with the experiment except for PPC that fails to reproduce the 1300 keV scale. The experimental energy scales are jointly predicted by the PPC and QTBA.

Table 4.7 shows that, in the case of ^{44}Ca, the three classes of scales are present in the experimental data as well as in all the theoretical calculations. There is a good correspondence between the experimental data and PPC results in each of the classes. The QTBA and QRPA results also produce the scales in the measured data with the exception of the 330 keV scale. The PPC gave a better representation of the experimental data for ^{44}Ca.

For the case of ^{42}Ca table 4.7 shows that the three classes of scales are present in the experimental data. They are also present in the PPC and QTBA results. In the QRPA calculations Classes I and II are present but Class III is missing.

In summary, the characteristic energy scales extracted using the CWT technique are shown in Tables 4.6 and 4.7. Class III scales are most consistently reproduced by PPC. This suggests that non-harmonicity owing to interactions among phonons plays an important role. Class II scales are rather consistently reproduced by QTBA. This suggests that fragmentation of single-particle spectroscopic strength due to long-range correlations

(coupling to collective phonons) plays an important role. Class II scales are reproduced by QRPA too, but not as close to those extracted from experiment. The results suggest a certain complementarity of QRPA and QTBA. In Class I scales, there is some variance among models and isotopes. Generally, all models shown reproduce Class I scales, with the exception of QRPA in ^{48}Ca and ^{40}Ca, the two closed-shell nuclei and PPC in ^{48}Ca. It can be seen that no one microscopic model compared quantitatively well with the data. However, a combination of the PPC and the QTBA provides a quantitative description of the experimental data for the doubly-magic nuclei ^{48}Ca and ^{40}Ca. This suggests that the fine structure of ISGMR in the doubly-magic calcium isotopes originates from fragmentation of single-particle spectroscopic strength due to coupling to collective phonons and non-harmonicity owing to interactions among phonons. In the case of ^{44}Ca, the experimental scales are best reproduced by the PPC, suggesting coupling to collective phonon as the signatures for the scales. In the case of ^{42}Ca and ^{44}Ca, the lowest experimental scales in both nuclei seem to correspond to Landau damping, since comparable scales are found in the QRPA.

4.5 Level density of 0^+ states in the ISGMR region for ^{40,42,44,48}Ca

This section focuses on the extraction of level densities of $J^\pi = 0^+$ states in ^{48,44,42,40}Ca by means of the fluctuation analysis (discussed in Section 2.4.2) in the excitation-energy region, E_x = 12 MeV to 22 MeV. The extracted experimental level densities are compared with microscopic and phenomelogical models.

4.5.1 Fluctuation analysis

The theory of fluctuation analysis as it relates to level density extraction was discussed in Section 2.4.2. As presented in Eq. (2.60), the experimental autocorrelation function $C(\epsilon$=0)-1, known as the variance of the stationary spectrum, has a direct proportionality with the mean level spacing $\langle D \rangle$. It then means that the mean level spacing can be determined once the value of the variance is known. Before the level spacing can be extracted from the value of $C(\epsilon = 0)$-1, it is essential that the background be determined. In the alpha inelastic-scattering measurements presented here, three main sources of backgrounds can be identified: they are instrumental background, background from other multipoles excited and those from quasi-free scattering conditions. The instrumental background and those from quasi-free scattering reactions have been removed to a great extent during the data reduction as discussed in Section 3.5. Contributions from multipoles other than the isoscalar monopole as well as those from quasi-free scattering conditions have been largely removed by the DoS technique discussed in Section 4.2.2.

4.5.2 Extraction of level densities of 0^+ states in ^{40,42,44,48}Ca

Fluctuation analysis was performed on the background-free difference spectrum following the procedure detailed in Section 2.4.2.1. The background-free spectrum is smoothed and folded with a Gaussian of width

σ and another Gaussian of width $\sigma_>$ resulting in the spectra $g(E_x)$ and $g_>(E_x)$, respectively. For the present study, the widths of the Gaussian functions were chosen to be $\sigma = 0.4\Delta E$ and $\sigma_> = 3\sigma$, where ΔE is the experimental energy resolution (85 keV (FWHM)). As an illustration, the fluctuation analysis procedure is shown for ^{48}Ca where the spectra $g(E_x)$ and $g_>(E_x)$ are superimposed on each other in the second panel of Fig. 4.35. A dimensionless stationary spectrum, $d(E_x)$ of Eq. (2.57) distributed around the mean value of 1 is shown in the third panel down of Fig. 4.35 Typical autocorrelation functions for both theoretical and experimental data are shown superimposed on each other in the lower panel of Fig. 4.35.

Using Eq. (2.60), the level spacing can be obtained from the experimental autocorrelation function taking $\alpha = 2.273$, $\sigma = 40$ keV and $\sigma_> = 120$ keV.

A rearrangement of Eq. (2.60) gives,

$$\langle D \rangle = (C(\epsilon = 0)1) \times Constant. \tag{4.4}$$

The level density in each energy bin for a particular target nucleus is calculated by taking the reciprocal of the corresponding mean level spacing (see Eq. (2.64)).

The results of the extracted $J^\pi = 0^+$ level densities in ^{48}Ca and ^{40}Ca compared with various theoretical models are presented in Figs. 4.36 and 4.37, respectively, and discussed below. In these figures, the solid black symbol represent the experimental results. The green and the red lines represent the BSFG level density calculations using the parameterisations of Refs. [Egi05] and [Rau97], respectively (see Section 2.4.1.1). The blue and the cyan lines represents the results from HFB [Hil06] and HF-BCS [Dem01] models, respectively (see Section 2.4.1.2).

Taking the results for each calcium isotopes in turn:

^{48}Ca: Figure 4.36 shows the extracted measured level-density of 0^+ states in ^{48}Ca compared with the theoretical model predictions. It can be seen that the experimental data show an energy dependence similar to those of the parametrisations of the HF-BCS and both parametrisations of the BSFG. In terms of magnitude, however, in the excitation-energy region, $E_x = 12$ to 15

MeV BSFG of [Rau97], HFB and HF-BCS agree reasonably well with the experimental data. Between 17 and 21 MeV only BSFG of [Egi05] and HFB agree with the experiment. At large, the HFB best describes the experimental results.

^{40}Ca: In the excitation-energy region, E_{x} = 11 to 22 MeV, the measured level densities of $J^{\pi} = 0^{+}$ states in ^{40}Ca rose by more than one order of magnitude as shown in Fig. 4.37. All the models agree quite well with the experiment between 14 and 18 MeV excitation energy. However, below 14 MeV and above 18 MeV only the HFB (with substantial fluctuations) shows reasonable agreement with the experimental level density.

In general, the qualitative trend of the experimental level densities is best described by the HFB parametrisation. The experimental values are within the error limits in comparison with the theoretical model calculations. The uncertainties of the extracted experimental level densities were obtained by varying the: (i) smoothing parameters, a variation by 10% was used. (ii) range of the excitation-energy interval, the analysis was repeated for interval sizes between 0.5 and 2MeV. Moreso, level densities are used as one of the input parameters in astrophysical calculations especially in the region of unresolved states above the particle thresholds. The comparison with different theoretical models allows on the choice of calculations, based on either phenomenological (BSFG) or microscopic (HFB) cases for the nuclei under investigation.

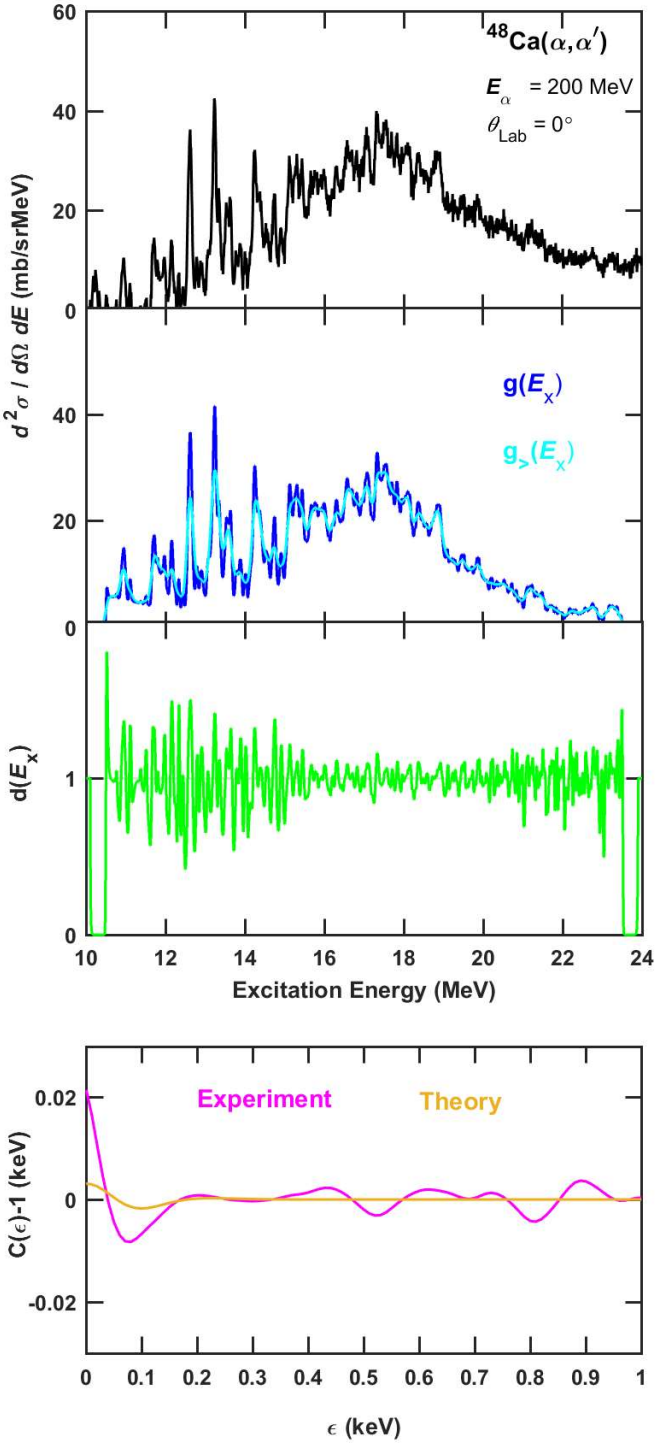


Figure 4.35: *Upper part top*: Spectrum of the ^{48}Ca(α, α') reaction at 0°. *Upper part middle*: Smoothed spectra $g(E\mathrm{x})$ and $g_>(E_\mathrm{x})$. *Upper part bottom*: Stationary spectrum $d(E_\mathrm{x})$. *Lower part*: Experimental (magenta line) and theoretical (dark yellow line) autocorrelation functions.

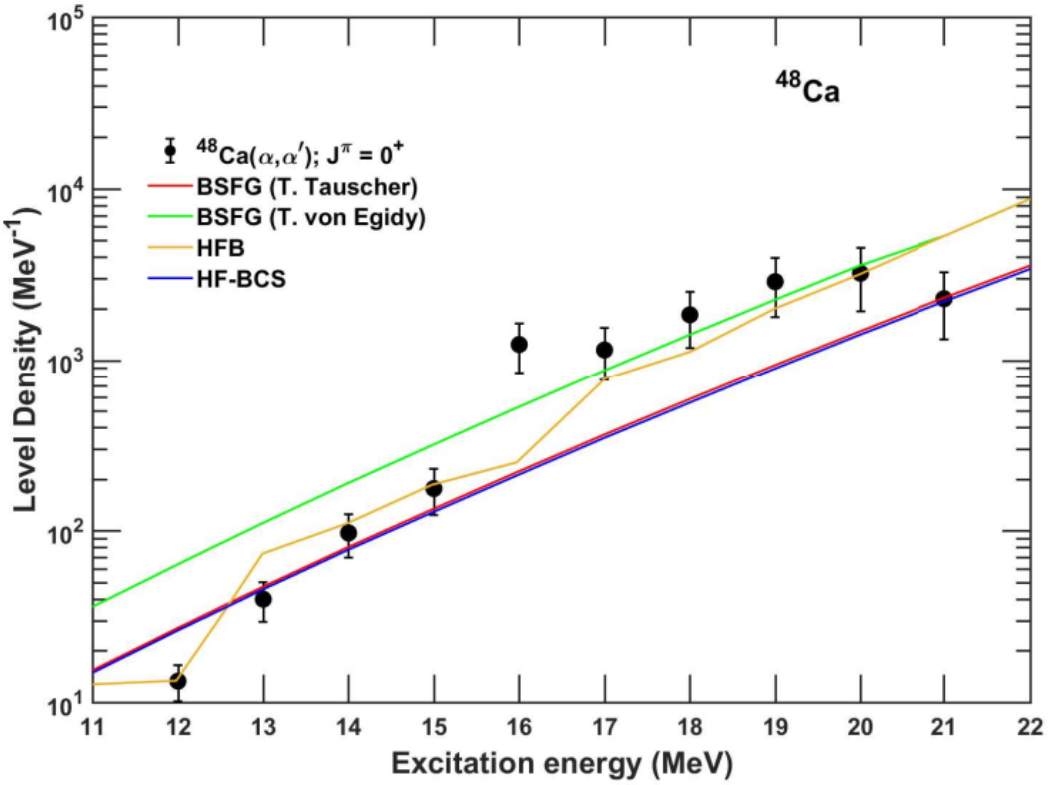


Figure 4.36: Level density of 0^+ states extracted from ^{48}Ca(α, α') and the theoretical models: BSFG of Ref. [Egi05] (green line), BSFG of Ref. [Rau97] (red line), HFB of Ref. [Hil06] (dark yellow line) and HF-BCS of Ref. [Dem01] (blue line).

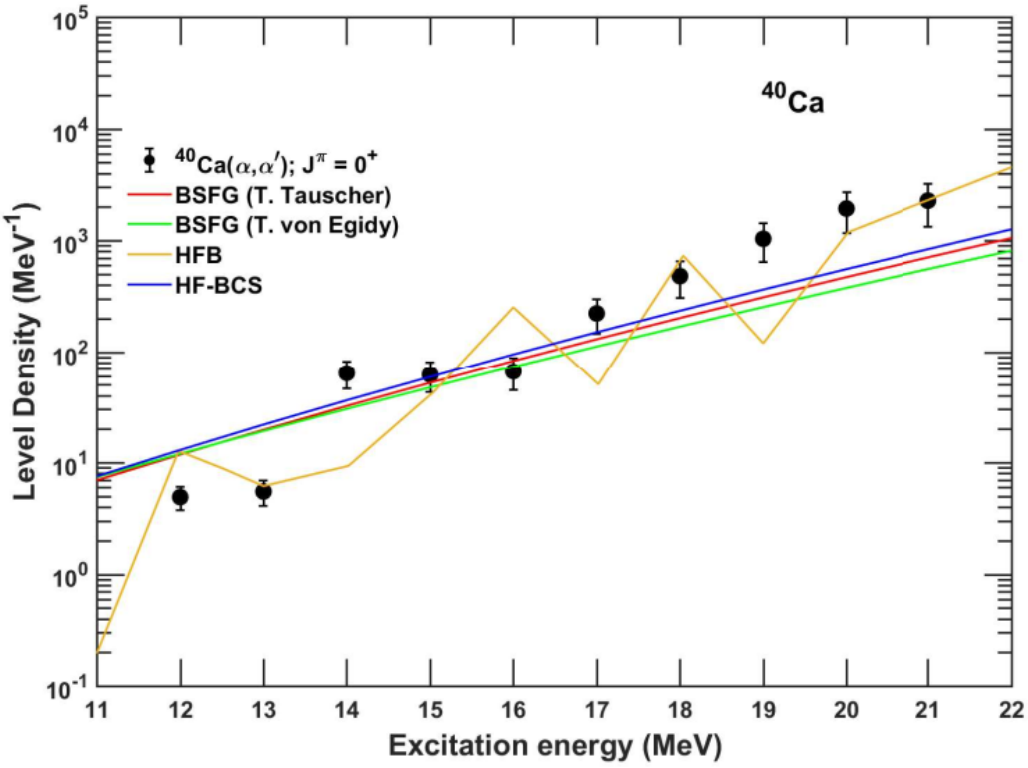


Figure 4.37: Level density of 0^+ states extracted from ^{40}Ca(α, α') and the theoretical models: BSFG of Ref. [Egi05] (green line), BSFG of Ref. [Rau97] (red line), HFB of Ref. [Hil06] (dark yellow line) and HF-BCS of Ref. [Dem01] (blue line).

Chapter 5

Conclusions

Inelastic α-particle scattering measurements, with $E_\alpha = 200$ MeV and $\theta_{\text{Lab}} = 0^\circ$ and 4°, were carried out on ^{40,42,44,48}Ca with the view of investigating fine structure in the Isoscalar Giant Monopole Resonance (ISGMR). The experiments were performed using the K600 magnetic spectrometer and the Separated Sector Cyclotron (SSC) facility at iThemba LABS, South Africa. For each of the four calcium targets, considerable fine structure was observed in the excitation energy region of the ISGMR. Contaminant oxygen peaks were identified in the ISGMR regions of the experimental excitation-energy spectra for all the calcium isotopes. Direct background-subtraction method was applied in order to remove the oxygen contaminants. Subsequently, the oxygen-subtracted data were converted to double-differential cross sections.

In order to apply the Difference of Spectra (DoS) technique for determination of $E0$ strength for ^{40,42,44,48}Ca(α,α') at E_α= 200 MeV, the angle cut for the measurement at $\theta_{\text{Lab}} = 4^\circ \pm 2^\circ$ is determined from DWBA calculations. Following which the DoS technique was applied to determine the Fraction $E0$ EWSR and the $E0$ strength in the region of the ISGMR for the various calcium isotopes. The fraction $E0$ EWSR and the $E0$ strengths obtained in the present work were compared with those from TAMU (for ^{48}Ca Ref. [Lui11]) and RCNP (for ^{48,44,42,40}Ca Ref. [How20]) within $10 \leq E_{\text{x}} \leq 25$ MeV region, and agreement was found among the three data sets. Also, centroids and widths were determined for the ISGMR from the corresponding strength functions for the various calcium isotopes using Lorentzian fitting procedure.

In addition, by applying the Continuous Wavelet Transform (CWT) technique the characteristic energy scales of the ISGMR of these isotopes were extracted from the oxygen-free difference spectra and compared to those of theoretical calculations within the framework of the Phonon Phonon Coupling (PPC) the Quasiparticle Time Blocking Approximation (QTBA) and the Quasi-particle Random Phase Approximation (QRPA). Of all these models, the PPC best described the experimental data for all the four isotopes of calcium in terms of reproducibility of the energy scales present in them as well as in terms of the amount of fine structure exhibited and the prediction of the centroid energies, compared to the other models. The comparison between theory and experimental seems to indicate that the origin of the fine structure is caused by different mechanisms in the doubly magic nuclei and the singly-magic nuclei. The situation is very similar to what is seen in the IVGDR and different from the ISGQR as discussed in [Neu19]. For ^{42,44}Ca the deviations are generally larger and no clear signature for scales beyond Landau damping is found.

The extraction of spin- and parity-dependent level densities of 0° states in ^{48}Ca and ^{40}Ca nuclei in the ISGMR region was achieved by means of the fluctuation analysis technique and comparisons between the experimentally obtained level densities with those from theoretical models were done. In general, there is an overall fair agreement between results from experiment and theory.

References

[Ada84] S. Adachi and Van R. Gial. In: *Phys. Lett. B* 149.447 (1984).

[Agv03] U. Agvaanluvsan, G. E. Mitchell, J. F. Shriner Jr., and M. Pato. In: *Phys. Rev. C* 67.064608 (2003).

[And13] M. Anders, S. Shlomo, Tapas Sil, D. H. Youngblood, Y.-W. Lui, and Krishichayan. In: *Phys. Rev. C* 87.024303 (2013).

[Ars17] N.N. Arsenyev. In: *Phys. Rev. C* 95.054312 (2017).

[Ars19] N. Arsenyev. Private Communication. 2019.

[Ber93] M. Berz, K. Joh, J. A. Nolen, B. M. Sherrill, and A. F. Zeller. In: *Physical Review* C 47 (1993), p. 537.

[Bet37] Bethe. In: *Rev. Mod. Phys.* 9 (1937), p. 69.

[Bla80] J.P. Blaizot. In: *Phys. Rep.* 64.171 (1980).

[Blo71] H. G. Blosser, G. M. Crawley, R. Deforest, E. Kashy, and B. H. Wildenthal. In: *Nucl. Instrum. Methods* 91 (1971), pp. 61–65.

[Boh51] D. Bohm and D. Pines. In: *Phys. Rev.* 82.625 (1951).

[Boh75] A. Bohr and B.M. Mottleson. *Nuclear Structure II.* Benjamin. New York, 1975.

[Bor81] K. van der Borg, M. N. Harakeh, and A. van der Woude. In: *Nuclear Physics* A 365 (1981), pp. 243–300.

[Bot37] W. Bothe and W. Z. Genther. In: *Phys.* 106 (1937), p. 236.

[Bra83] S. Brandenburg. In: *Phys. Lett. 130B* 9 (1983).

[But17] J. Button, Y.-W. Lui, D. H. Youngblood, X. Chen, and S. Bonasera G.and Shlomo. "Isoscalar E0, E1, and E2 strength in ^{44}Ca". In: *Phys. Rev. C* 96.054330 (2017).

[Cat05] W.N. Catford. "Catkin ver.2.02". In: *http://personal.ph.surrey.ac.uk/ phs1wc/kinematics/* (2005).

[Coh59] B. L. Cohen. In: *Rev. Sci. Instrum* 30 (1959), p. 415.

[Con09] D. Cong Cuong *et al.* In: *Nucl. Phys. A* (2009).

[Dem01] P. Demetriou and S. Goriely. In: *Nucl. Phys. A* 695 (2001), p. 95.

[Dil73] W. Dilg, W. Schantl, and H Vonach. In: *Nucl. Phys. A* 217 (1973), p. 269.

[Don16] L.M. Donaldson. "PhD Thesis". PhD thesis. University of the Witwatersrand, 2016.

[Don18] L.M Donaldson, C.A. Bertulani, J Carter, V.O. Nesterenko, P. von Neumann-Cosel, R. Neveling, V.U Ponomarev, P.G Reinhard, I.T Usman, P. Adsley, J.W Brummer, E.Z. Buthelezi, G.R.J Cooper, R.W. Fearick, S.V Fortsch, H. Fujita, Y. Fujita, M. Jingo, W. Kleinig, C.O. Kureba, J. Kvasil, M. Latif, K.C.W Li, J.P Mira, F Nemulodi, P. Papka, L Pellegri, N. Pietralla, A. Richter, E. Sideras-Haddad, F.D. Smit, G.F. Steyn, J.A Swartz, and A. Tamii. "Deformation dependence of the isovector giant dipole resonance: The neodymium isotopic chain revisited". In: *Phys. Lett. B* 776 (2018), pp. 133–138.

[Dro86] S. Drozdz, V. Klemt, J. Speth, and J. Wambach. In: *Nucl. Phys. A* 451.11 (1986).

[Egi05] T. von Egidy and D. Bucurescu. In: *Phys. Rev. C* 72.044311 (2005).

[Egi88] T. von Egidy, H. H. Schmidt, and A. N. Behkami. In: *Nucl. Phys. A* 481 (1988), p. 189.

[Ego16] Irina A. Egorova1 and Elena. Litvinova. "Electric dipole response of neutron-rich calcium isotopes in relativistic quasiparticle time blocking approximation". In: *Phys. Rev. C* 94.034322 (2016).

[Eri60] T. E. O. Ericson. In: *Adv. Phys.* 9 (1960), p. 425.

[Fir07] R. B. Firestone. In: *In:Nucl. Data Sheets* 58 (2007), pp. 2319–2392.

[Fri95] G. Fricke and C. Bernhardt. In: *Phys. Rev. C* 60.177 (1995).

[Fuj02] H. Fujita, Y. Fujita, G. P. A. Berg, A. D. Bacher, C. C. Foster, K. Hara, K. Hatanaka, T. Kawabata, T. Noro, H. Sakaguchi, Y. Shimbara, T. Shinada, E. J. Stephenson, H. Ueno, and M. Yosoi. In: *Nucl. Instrum. Meth. A* 484 (2002), pp. 17–26. ISSN: 01689002.

[Fuj97] Y. Fujita, K. Hatanaka, G. P. A. Berg, K. Hosono, N. Matsuoka, S. Morinobu, T. Noro, M. Sato, K. Tamura, and H. Ueno. In: *Nucl. Instrum. Meth. B* 126.96 (1997), pp. 274–278.

[Gad68] E. Gadioli and L. Zetta. In: *Phys. Rev.* 167 (1968), p. 1016.

[Gar18] U. Garg. In: *Prog. Part. Nucl. Phys.* 55.101 (2018).

[Gia98] Nguyen Van Giai, Ch. Stoyanov, and V.V Voronov. In: *Phys. Rev. C* 57.1204 (1998).

[Gup16] Y.K. Gupta *et al.* In: *Phys. Lett. B* 760 (2016), pp. 482–485.

[Haq82] R. U. Haq, A. Pandey, and O. Bohigas. In: *Phys. Rev. Lett.* 48 (1982), p. 1086.

[Har01] M. N. Harakeh and A. Van der Woude. *Giant resonances: Fundamental High-Frequency Modes of Nuclear Excitation*. Oxford Studies in Nuclear Physics. New York: Oxford University Press Inc., 2001.

[Har77] M. N. Harakeh, K. van der Borg, T. Ishimatsu, H. P. Morsch, A. van der Woude, and F. E. Bertrand. In: *Phys. Rev. Lett.* 36 (1977), p. 676.

[Hil01] S. Hilaire, J. P. Declaroche, and M. Girod. In: *Eur. Phys. J. A* 12 (2001), p. 169.

[Hil06] S. Hilaire and S. Goriely. In: *Nucl. Phys. A* 779.63 (2006).

[How19] K.B. Howard, U. Garg, Y.K Gupta, and M.N Harakeh. In: *Eur. Phys. J. A* 55.228 (2019).

[How20] K.B. Howard, U. Garg, M. Itoh, M. Akimune, S. Bagchi, T. Doi, Y. Fujikawa, M. Fujiwara, T. Furuno, M. N. Harakeh, Y. Hijikata, K Inaba, S. Ishida, N. Kalantar-Nayestanaki, T. Kawabata, S. Kawashima, K. Kitamura, N. Kobayashi, Y. Matsuda, A. Nakagawa, S. Nakamura, K. Nosaka, S. Okamoto, S. Ota, S. Weyhmiller, and Z. Yang. "Compression-mode resonances in the calcium isotopes and implications for the asymmetry term in nuclear incompressibility". In: *Phys. Lett. B* 801.135185 (2020).

[Hub18] N. J. Hubbard. "Studies of the nuclear structure of 12C and the astrophysical production of 23Na". PhD thesis. University of York, 2018.

[Hui69] J. R. Huizenga et al. In: *Phys. Rev.* 182 (1969), p. 1149.

[Ike80] H. Ikegami, S. Morinobu, I. Katayama, M. Fujiwara, and S. Yamabe. In: *Nuclear Instruments and Methods* 175 (1980), p. 335.

[Ito03] M. Itoh *et al.* In: *Phys. Rev. C.* 68.064602 (2003).

[Jin14] M. Jingo. "Fine structure of the Isovector Giant Dipole Resonance : A survey with the (p,p′) reaction at zero degrees". PhD. University of the Witwatersrand, 2014.

[Jin18] M. Jingo *et al.* In: *Eur. Phys. J. A* 54.234 (2018).

[Jon76] B. Jonson, E. Hagberg, P. G. Hansen, P. Hornshoj, and P. Tidemand-Petersson. In: *Proc. 3rd Int. Conf. on Nuclei far from Stability* Cargese, 1976.277 (1976),

[Kal06] Y. Kalmykov *et al.* In: *Phys. Rev. Lett.* 96.012502 (2006).

[Kaw10] T. Kawabata, T. Adachi, M. Fujiwara, K. Hatanaka, Y. Ishiguro, M. Itoh, Y. Maeda, H. Matsubara, H. Miyasako, Y. Nozawa, T. Saito, S. Sakaguchi, Y. Sasamoto, Y. Shimizu, T. Takahashi, A. Tamii, S. Terashima, H. Tokieda, N. Tomida, T. Uesaka, M. Uchida, Y. Yasuda, N. Yokota, H. P. Yoshida, and J. Zenihiro. "Alpha inelastic scattering and cluster structures in light nuclei". In: *AIP Conference Proceedings* 1235 (2010), p. 207.

[Kri15] Krishichayan, Y.-W. Lui, D. H. Youngblood, J. Button, G. Bonasera, and S. Shlomo. "Isoscalar giant resonances in 90,92,94Zr". In: *Phys. Rev. C* 92.044323 (2015).

[Kuh81] G. Kuhner *et al.* In: *Phys. Lett. B* 104.189 (1981).

[Kur18] C.O Kureba *et al.* In: *Phys. Lett. B* 779.269 (2018).

[Lat17] M. B. Latif. "Fine structure of the Isovector Giant Dipole Resonance in neutron-rich calcium isotopes using the (p,p')reaction at zero-degrees". PhD thesis. University of the Witwatersrand, 2017.

[Lat19] M. B. Latif et al. In: *Acta Physica Polonica B* 50.3 (2019).

[Lew72] M. B. Lewis and F. E. Bertrand. In: *Nucl. Phys. A* 196.337 (1972).

[Li10] T. Li, U. Garg, Y. Liu, R. Marks, B.K. Nayak, P.V. Madhusudhana Rao, M. Fujiwara, H. Hashimoto, K. Nakanishi, S. Okumura, M. Yosoi, M. Ichikawa, M. Itoh, R. Matsuo, T. Terazono, M. Uchida, Y. Iwao, T. Kawabata, T. Murakami, H. Sakaguchi, Z. Terashima, Y. Yasuda, J. Zenihiro, H. Akimune, K. Kawase, and M.N. Harakeh. "Isoscalar giant resonance in the Sn nuclei and implications for the

asymmetry term in the nuclear-matter incompressibility". In: *Phys. Rev. C* 81.034309 (2010).

[Lit08] Elena Litvinova, P. Ring, and V. Tselyaev. "Relativistic quasiparticle time blocking approximation: Dipole response of open-shell nuclei". In: *Phys. Rev. C* 78.014312 (2008).

[Lit19] E. Litvinova. Private Communication. 2019.

[Lui11] Y.-W. Lui, D. H. Youngblood, S. Shlomo, X. Chen, Y. Tokimoto, Krishichayan, M. Anders, and J. Button. In: *Phys. Rev. C* 83.044327 (2011).

[Mal98] S. Mallat. In: *(Academic Press, San Diego, 1998)* (1998).

[Mar83] S. A. Martin, A. Hardt, J. Meissburger, G. P. A. Berg, U. Hacker, W. Hürlimann, J. G. M. Römer, T. Sagefka, A. Retz, O. W. B. Schult, K. L. Brown, and K. Halbach. In: *Nucl. Instrum. Methods* 214 (1983), pp. 281–303.

[Men04] E. Menapace, C. Birattari, M. L. Bonardi, and F. Groppi. In: *Radiation Physics and Chemistry* 71 (2004), p. 943.

[Mig44] A. B. Migdal. In: *Acad. Sci. USSR* 8.331 (1944).

[Moo19] Chane Simone Moodley. "Fine structure of the Isoscalar Giant Monopole Resonance in 58Ni and 90Zr using alpha inelastic scattering at zero degrees". MA thesis. University of the Witwatersrand, 2019.

[Mul83] S. Muller. "PhD Dissertation D17". PhD thesis. TH Darmstadt, 1983.

[Neu19] Peter von Neumann-Cosel, Vladimir Yu. Ponomarev, Achim Richter, and Jochen Wambach. "Gross, intermediate and fine structure of nucleargiant resonances: Evidence for doorway states". In: *Eur. Phys. J. A* 55.224 (2019).

[Nev11] R. Neveling, H. Fujita, F. D. Smit, T. Adachi, G. P. A. Berg, E. Z. Buthelezi, J. Carter, J. L. Conradie, M. Couder, R. W. Fearick, S. V. Förtsch, D. Fourie, Y. Fujita, J. Görres, K. Hatanaka, A. M. Heilmann, J. P. Mira, S. H. T. Murray, P. Von Neumann-Cosel, S. O'Brien, P. Papka, I. Poltoratska, A. Richter, E. Sideras-Haddad, J. A. Swartz, A. Tamii, I. T. Usman, and J. J. Van Zyl. In: *J. Phys. Conference Series* 312 (2011), p. 052016.

[Nev17] R. Neveling, F. D. Smit, H. Fujita, P. Adsley, K. C. W. Li, J. W. Brummer, D. J. Marin–Lambarri, and R. T. Newman. "Guide to the K600 magnetic spectrometer". In: *Unpublished* (2017).

[Pap07] P. Papakonstantinou. In: *Europhysics Letters* 78.12001 (2007).

[Pap09] P. Papakonstantinou and R. Roth. In: *Phys. Lett. B* 671.356 (2009).

[Pap10] P. Papakonstantinou and R. Roth. In: *Phys. Rev. C* 81.024317 (2010).

[Pap19] P. Papakonstantinou. Private Communication. 2019.

[Pat14] D. Patel *et al.* In: *Phys. Lett. B* 735 (2014), pp. 378–390.

[Pat15] D.C. Patel. *A Study of the Isoscalar Giant Monopole Resonance: The Role of Symmetry Energy in Nuclear Incompressibility in the Open-ShellNuclei.* Springer Theses. 2015.

[Pit71] R. Pitthan and T. Walcher. In: *Phys. Lett. 36B* 563 (1971).

[Por56] C. E. Porter and R. G. Thomas. In: *Phys. Rev.* 104 (1956), p. 483.

[Rau97] T. Rauscher, F. Thielemann, and K. Kratz. In: *Phys. Rev. C* 56 (1997), p. 1613.

[Rho80] M. Rhoades-Brown. In: *Phys. Rev. C* 21.2417 (1980).

[Sat72] G.R. Satchler. "Particle". In: *Part. Nucl.* 5.105 (1972).

[Sat87] G. R. Satchler and Dao T. Khoa. In: *Nucl. Phys. A* 472.215 (1987).

[Sat97] G. R. Satchler and Dao T. Khoa. In: *Phys. Rev. C.* 55.1 (1997).

[Sev04] A. P. Severyukhin, V. V. Voronov, and Nguyen Van Giai. In: *Eur. Phys. J A* 22 (2004), pp. 397–403.

[Sev08] A.P. Severyukhin. In: *Phys. Rev. C* 77.024322 (2008).

[Sev12] A. P. Severyukhin, N. N. Arsenyev, and N Pietralla. In: *Phys. Rev. C* 86 (2012), p. 024311.

[She04] A. Shevchenko, J. Carter, R. W. Fearick, S. V. Förtsch, H. Fujita, Y. Fujita, Y. Kalmykov, D. Lacroix, J. J. Lawrie, P. von Neumann-Cosel, R. Neveling, V. Yu. Ponomarev, A. Richter, E. Sideras-Haddad, F. D. Smit, and J. Wambach. In: *Phys. Rev. Lett.* 93 (2004), p. 122501.

[She08] A. Shevchenko, G. R. J. Cooper, J. Carter, R. W. Fearick, S. V. Ffffdfffdortsch, Y. Kalmykov, P. von Neumann-Cosel, V. Yu. Ponomarev, A. Richter, I. Usman, and J. Wambach. In: *Phys. Rev. C* 77 (2008), p. 024302.

[She09] A. Shevchenko, O. Burda, J. Carter, G. Cooper, R. Fearick, S. Förtsch, H. Fujita, Y. Fujita, Y. Kalmykov, D. Lacroix, J. Lawrie, P. von Neumann-Cosel, R. Neveling, V. Ponomarev, A. Richter, E. Sideras-Haddad, F. Smit, and J. Wambach. In: *Phys. Rev. C* 79 (2009), p. 044305.

[Shl87] S. Shlomo, Y.-W. Lui, D. H. Youngblood, T. Udagawa, and T. Tamura. In: *Phys. Rev. C* 36 (1987), p. 1317.

[Sol92] V. G. Soloview. "Theory of Atomic Nuclei: Quasiparticles and Phonon". In: *(Institute of Physics, Bristol and Philadelphia, 1992)* (1992).

[Ter05] J. Terasaki, J. Engel, M. Bender, J. Dobaczewski, W. Nazarewicz, and M. Stoitsov. In: *Phys. Rev. C* 71.034310 (2005).

[Tho61] D.J. Thouless. In: *Nuclear Physics* 22.78 (1961).

[Uch04] M. Uchida *et al.* In: *Phys. Rev. C.* 69.051301 (2004).

[Usm11] I. Usman et al. In: *Phys. Lett. B* 698 (2011), pp. 191–195.

[Usm16] I. T. Usman. "Fine structure of the Isoscalar Giant Monopole Resonance in ^{42,44,48}Ca, using alpha inelasticscattering at zero degree." In: *PR260, Research Proposal to iThemba LABS* (2016).

[Vis03] Dale Visser. "JRelKin". Wright Nuclear Structure Laboratory, Yale University, 2003.

[Voi09] A. V. Voinov, B. M. Oginni, S. M. Grimes, C. R. Brune, Guttormsen M., A. V. Laesen, T. N. Massey, A. Schiller, and S. Siem. In: *Phys. Rev. C* 79.031301(R) (2009).

[Wak02] T. Wakasa, K. Hatanaka, Y. Fujita, G. P. A. Berg, H. Fujimura, H. Fujita, M. Itoh, J. Kamiya, T. Kawabata, K. Nagayama, T. Noro, H. Sakaguchi, Y. Shimbara, H. Takeda, K. Tamura, H. Ueno, M. Uchida, M. Uraki, and M. Yosoi. In: *Nuclear Instruments and Methods in Physics Research* A 482 (2002), p. 79.

[Whe14] C. Wheldon. "Derivations for two-body kinematics (both relativistic and non-relativistic)". In: (2014).

[Wig65] E. P. Wigner and C. E. Porter. “Statistical theories of spectra: fluctuations”. In: *(Academic Press, New York, 1965)* 200 (1965).

[Yan86] C. Yannouleas and S. Jang. In: *Nucl. Phys. A* 455.40 (1986).

[You01] D. H. Youngblood, Y.-W. Lui, and H. L. Clark. “Isoscalar E0, E1, and E2 strength in 40Ca”. In: *Phys. Rev. C* 63.067301 (2001).

[You13] D. H. Youngblood, Y.-W. Lui, Krishichayan, J. Button, M. R. Anders, M. L. Gorelik, M. H. Urin, and S. Shlomo. “Unexpected characteristics of the isoscalar monopole resonance in the A 90 region: Implications for nuclear incompressibility”. In: *Phys. Rev. C* 88.021301(R) (2013).

[You15] D. H. Youngblood, Y.-W. Lui, Krishichayan, J. Button, G. Bonasera, and S. Shlomo. “Isoscalar E0, E1, E2, and E3 strength in 92,96,98,100Mo”. In: *Phys. Rev. C* 92.014318 (2015).

[You77] D. H. Youngblood, C. M. Rozsa, J. M. Moss, D. R. Brown, and J. D. Bronse. In: *Phys. Rev. Lett.* 39 (1977), p. 1188.

[You91] D.H. Youngblood *et al.* In: *Phys. Rev. C.* 44.1878 (1991).

[You97] D. H. Youngblood, Y.-W. Lui, and H. L. Clark. In: *Phys. Rev. C* 55.2811 (1997).

[You99] D. H. Youngblood, H. L. Clark, and Y. -W. Lui. In: *Phys. Rev. Lett.* 82 (1999), p. 691.